Distribution System Modeling, Analysis and Design with High Penetration of Photovoltaic Generation

by

Yingying Tang

A Dissertation Presented in Partial Fulfillment
of the Requirements for the Degree
Doctor of Philosophy

Approved April 2016 by the
Graduate Supervisory Committee:

Raja Ayyanar, Chair
George Karady
Gerald Heydt
Vijay Vittal

ARIZONA STATE UNIVERSITY

May 2016

ABSTRACT

Present distribution infrastructure is designed mainly for uni-directional power flow with well-controlled generation. An increase in the inverter-interfaced photovoltaic (PV) systems requires a thorough re-examination of the design, operation, protection and control of distribution systems. In order to understand the impact of high penetration of PV generation, this work conducts an automated and detailed modeling of a power distribution system. The simulation results of the modeled distribution feeder have been verified with the field measurements.

Based on the feeder model, this work studies the impact of the PV systems on voltage profiles under various scenarios, including reallocation of the PV systems, reactive power support from the PV inverters, and settings of the load-tap changing transformers in coordination with the PV penetration. Design recommendations have been made based on the simulation results to improve the voltage profiles in the feeder studied.

To carry out dynamic studies related to high penetration of PV systems, this work proposes a differential algebraic equation (DAE) based dynamic modeling and analysis method. Different controllers including inverter current controllers, anti-islanding controllers and droop controllers, are designed and tested in large systems. The method extends the capability of the distribution system analysis tools, to help conduct dynamic analyses in large unbalanced distribution systems.

Another main contribution of this work is related to the investigation of the PV impacts on the feeder protection coordination. Various protection coordination types, including fuse-fuse, recloser-fuse, relay-fuse and relay-recloser have been studied. The analyses

provide a better understanding of the relay and recloser settings under different configurations of the PV interconnection transformers, PV penetration levels, and fault types.

A decision tree and fuzzy logic based fault location identification process has also been proposed in this work. The process is composed of the off-line training of the decision tree, and the on-line analysis of the fault events. Fault current contribution from the PV systems, as well as the variation of the fault resistance have been taken into consideration. Two actual fault cases with the event data recorded were used to examine the effectiveness of the fault identification process.

TABLE OF CONTENTS

Page

CHAPTER Page

LIST OF TABLES

Table Page

LIST OF FIGURES

Figure Page

Figure Page

Figure Page

Figure Page

Figure Page

LIST OF SYMBOLS

Abbreviations

AM	Ante meridiem
AMI	Advanced metering infrastructure
AMPL	A mathematical programming language
ANSI	American national standards institute
BPF	Band-pass filter
CAIDI	Customer average interruption duration index
CART	Classification and regression trees
COM	Component object module
CTAIDI	Customer total average interruption duration index
dc	Direct current
DAE	Differential algebraic equations
DAS	Data acquisition systems
DFT	Discrete Fourier transform
DG	Distributed generation
DLL	Dynamic linked library
DOE	Department of energy
DSF	Double synchronous frame
DT	Decision-tree
EMTP	Electromagnetic transient program
FFC	Fundamental fault current
GIS	Geographic information system
GMR	Geometric mean radius
HV	High voltage
ID	Identifier

IEEE	Institute of electrical and electronics engineers
IGBT	Insulated gate bipolar transistors
LTC	Load-tap changing
LV	Low voltage
ms	Millisecond
p.u.	per unit
PCC	Point of common coupling
PLL	Phase-locked loop
PM	Post meridian
PV	Photovoltaic
PWM	Pulse width modulation
RES	Renewable energy standards
RME	Renewable energy standards
RMS	Root mean square
SAIDI	System average interruption duration index
SEL	Schweitzer engineering laboratories
TCC	Time current curve
TD	Time dial

Mathematical symbols

ang_A	Represents the angle difference between the positive sequence and the negative sequence of phase A
ang_B	Represents the angle difference between the positive sequence and the negative sequence of phase B
ang_C	Represents the angle difference between the positive sequence and the negative sequence of phase C
A	Parameters of the state space functions in Chapter 3, constant of the TCC expressions for relay and recloser in Chapter 4

A_j	A function defined on $\overline{X}$ so that each X_i can be assigned to one of the target classes
B	Parameters of the state space functions in Chapter 3, constant of the TCC expressions for relay and recloser
C	Parameters of the state space functions, or represents the capacitance of the PV inverter filter in Chapter 3, a set of target classes containing class of 1, 2, ..., J in Chapter 5
C_{Load}	Capacitance of the impedance load
$d(X_i)$	The target class assigned to the predictor variable X_i
D	Parameters of the state space functions in Chapter 3
E	PV inverter controller output
E_α	E under the α frame
E_β	E under the β frame
E_d	E under the d frame
E_q	E under the q frame
$Error_{dis}$	Percentage error of the geometric distance to the substation
G_c	Function of the PV controller
h	Time step used in dynamic simulation in Chapter 3, index of harmonic in Chapter 5
i	Represents the ground fault case number under relay-lateral fuse coordination study
$i(t)$	Instantaneous current value in Chapter 3, a Gini index defined during growing of the decision-tree in Chapter 5
i_1	State variable representing the current flowing through the inductance L_1 in PV inverter model
$i_{1\alpha}$	i_1 under the α frame
$\dot{i}_{1\alpha}$	Time differential of $i_{1\alpha}$
$i_{1\beta}$	i_1 under the β frame
$\dot{i}_{1\beta}$	Time differential of $i_{1\beta}$

i_{1d}	i_1 under the d frame
$\dot{i}_{1d}$	Time differential of i_{1d}
i_{1q}	i_1 under the q frame
$\dot{i}_{1q}$	Time differential of i_{1q}
i_2	State variable representing the current flowing through the inductance L_2 in PV inverter model
$i_{2\alpha}$	i_2 under the α frame
$\dot{i}_{2\alpha}$	Time differential of $i_{2\alpha}$
$i_{2\beta}$	i_2 under the β frame
$\dot{i}_{2\beta}$	Time differential of $i_{2\beta}$
i_{2d}	i_2 under the d frame
$\dot{i}_{2d}$	Time differential of i_{2d}
i_{2q}	i_2 under the q frame
$\dot{i}_{2q}$	Time differential of i_{2q}
i_a, i_b, i_c	Current outputs from the PV inverters in OpenDSS circuit in the initialization step
i_{an}, i_{bn}, i_{cn}	Current outputs from the PV inverters in OpenDSS circuit in step n
$i_f(t)$	Expression of the fault current
i_{ref}	Current reference for the PV inverter current controller
$\|I\|$	The magnitude of the PV inverter output current
$\vec{I}$	Represents the current phasors
I_0	Current in the power flow simulation before the dynamic simulations in Chapter 3, magnitude of the decaying dc offset in Chapter 5
I_{0maxL}	Maximum unbalanced current in the feeder
I_{0maxL_BRE}	Maximum unbalanced current seen by relay
I_{0maxL_REC}	Maximum unbalanced current seen by recloser
I_{fault}	Fault current seen by relay or recloser

I_h	Magnitude of the hth harmonic component
I_{jfault_BRE}	Fault current seen by relay in the fault case j applied
I_{jfault_REC}	Fault current seen by recloser in the fault case j applied
I_{maxL}	Maximum load current in the feeder
I_{maxL_BRE}	Maximum phase current seen by the relay
I_{maxL_REC}	Maximum phase current seen by the recloser
$I_{measured}$	Measured current at the substation (or the most upstream available DAS)
I_{min_phase}	Minimum phase fault current in the feeder
I_n	Currents in the power flow simulation in step n
I_{pickup}	Pickup current of relay or recloser
I_{pickup_ground}	Pickup current for ground relay or ground recloser
I_{pickup_phase}	Pickup current for phase relay or phase recloser
$I_{simulated}$	Simulated current at the substation (or the most upstream available DAS)
I_A	Recorded fault current at phase A by DAS. Used specifically as axis labels in the figures
I_B	Recorded fault current at phase B by DAS. Used specifically as axis labels in the figures
I_{BRE_pickup}	Pickup current for relay
I_C	Recorded fault current at phase C by DAS. Used specifically as axis labels in the figures
I_{REC_pickup}	Pickup current for recloser
j	Represents the ground fault case number under recloser-lateral fuse coordination study in Chapter 3, and represents the target class in Chapter 4
k	Tree index number
K	Value of R_{0f} under phase faults
K_1	Value of R_{2f} under phase faults
K_R	Parameter in the current controller of the PV inverter
K_P	Parameter in the current controller of the PV inverter

L	Inductance of the line, used specifically as illustration in the figure
L_1	Inductance of the PV inverter filter, used specifically as illustration in the figure
L_2	Inductance of the PV inverter filter, used specifically as illustration in the figure
L_{est}	Distance of the estimated fault location and the true fault location to the substation
L_{Load}	Inductance of the impedance load
L_{true}	Distance of the true fault location and the true fault location to the substation
m	One of the possible classes a given node belonging to
m_p	Active power droop coefficient
$min(I_{fault\_BRE})$	Minimum ground fault current seen by the relay in all the fault cases
$min(I_{fault\_REC})$	Minimum ground fault current seen by the recloser in all the fault cases
M	Bus inside the PV filter
n	One of the possible classes a given node belonging to
n_{DAS}	Total feeder DAS number
n_p	Reactive power droop coefficient
p	Represents the constant of the TCC expressions for relay and recloser in Chapter 3, and represents the maximum harmonic order in Chapter 4
$p(m\|t)$	Probability of a given sample at node t belonging to the class m
$p(n\|t)$	Probability of a given sample at node t belonging to the class n
$p(t)$	Probability that any case falls into node t
P	Average value of the output real power
$\tilde{P}$	Real power calculated inside the power controller
P_r	Rated real power
$P_{reference}$	Real power reference of the anti-islanding scheme
P_{output}	Real power output of the PV inverter
P_A	Used specifically as axis labels in the figures. Real power for phase A

P_{Load}	Real power consumed by the load
q	Quality factor
$\tilde{Q}$	Reactive power calculated inside the power controller
Q	Average value of the output reactive power
Q_r	Rated reactive power
Q_A	Used specifically as axis labels in the figures. Reactive power for phase A
$r(t)$	Resubstituition estimate of the misclassification error of a case in node t
R	Resistance of the line, used specifically as illustration in the figure
$R(T)$	Misclassification cost
$R(T_k)$	Misclassification error for the tree T_k
$R(T_{ko})$	Misclassification error for the optimal tree T_{ko}
R_{0f}	Represent the ratios of $\|I_{a0f}\|$ to $\|I_{a1f}\|$
R_1	Resistance of the PV inverter filter, used specifically as illustration in the figure
R_2	Resistance of the PV inverter filter, used specifically as illustration in the figure
R_{2f}	Represent the ratios of $\|I_{a2f}\|$ to $\|I_{a1f}\|$
R_3	Resistance of the PV inverter filter, used specifically as illustration in the figure
R_f	Fault resistance
R_{f1}	Fault resistance value, used specifically as illustration in the figure
R_{f2}	Fault resistance value, used specifically as illustration in the figure
R_{f3}	Fault resistance value, used specifically as illustration in the figure
R_{f4}	Fault resistance value, used specifically as illustration in the figure
R_{Load}	Resistance of the impedance load
$t(I_{fault})$	Operation time of the relay or recloser under fault current I_{fault}
$\vec{t}_{ifuse}$	Vector containing the open time of the fuses in the protection zone of the relay upstream of the recloser

$\vec{t}_{iBRE}$	Vector containing the operation time of the relay in the protection zone of the relay upstream of the recloser
$\vec{t}_{jfuse}$	Vector containing the open time of the fuses in the protection zone of the recloser
$\vec{t}_{jBRE}$	Vector containing the operation time of the relay in the protection zone of the recloser
$\vec{t}_{iREC}$	Vector containing the operation time of the recloser in the protection zone of the recloser
t_{ifuse}	Open time of the fuses under fault case *i*
t_{iBRE}	Operation time of the relay under fault case *i*
t_{jfuse}	Open time of the fuses under fault case *j*
t_{jBRE}	Operation time of the relay under fault case *j*
t_{jREC}	Operation time of the recloser under fault case *j*
T	Binary trees
T_c	Represents on cycle of the time, equaling to 0.0167 s
T_k	The *k*th binary tree
T_{ko}	Optimal decision-tree model
TD_{BRE}	Time dial value of the relay
TD_{REC}	Time dial value of the recloser
u	Input of the state space functions
u_0	Input of the state space functions in the initialization step
u_{PLL}	Input of the PLL
u_{n-1}	Input of the state space functions in the step (*n*-1)
u_n	Input of the state space functions in the step n
$v(t)$	Instantaneous voltage value
$\|V\|$	The percentage voltage at the PV terminal during faults in Chapter 5, the magnitude of the calculated voltage phasor in OpenDSS in Chapter 3

$\vec{V}$	Represents the voltage phasors
V_0	Voltages in the power flow simulation before the dynamic simulations
V_α	PV terminal voltage V_T on the α axis
V_β	PV terminal voltage V_T on the β axis
V_{a0}, V_{b0}, V_{c0}	PV terminal voltage V_T on the *abc* axis at the initialization step
V_{an}, V_{bn}, V_{cn}	PV terminal voltage V_T on the *abc* axis at step *n*
V_{ang_base}	Base voltage angle of 180° used as the weights for calculation of $\varepsilon_{FeederDAS}$
$V_{ang\_mea\_DAS\_ph}$	Measured voltage sag angel of the phase *ph* at the corresponding DAS
$V_{ang\_sim\_DAS\_ph}$	Simulated voltage sag angel of the phase *ph* at the corresponding DAS
V_{base}	Base voltage of 7200 V used as the weights for calculation of $\varepsilon_{FeederDAS}$
$V_{c\alpha}$	V_c under the α frame
$\dot{V}_{c\alpha}$	Time differential of $V_{c\alpha}$
$V_{c\beta}$	V_c under the β frame
$\dot{V}_{c\beta}$	Time differential of $V_{c\beta}$
V_c	Recorded fault voltage at phase C by DAS in Chapter 2, used specifically as axis labels in the figures. State variable representing the voltage across the capacitor in the PV inverter model in Chapter 3, used specifically as illustration in the figure.
V_{cd}	V_c under the *d* frame
$\dot{V}_{cd}$	Time differential of V_{cd}
V_{cq}	V_c under the *q* frame
$\dot{V}_{cq}$	Time differential of V_{cq}
V_d	PV terminal voltage V_T on the *d* axis
V_q	PV terminal voltage V_T on the *q* axis
V_m	Voltage at node *M* inside the PV filter
$V_{mea\_DAS\_ph}$	Measured voltage sag magnitude of the phase *ph* at the corresponding DAS

V_{md}	V_m on the d axis
V_{mq}	V_m on the q axis
V_n	Voltages in the power flow simulation at step n, or rated voltage
V_{sense}	Voltage sensed by the anti-islanding controller
$V_{sim\_DAS\_ph}$	Simulated voltage sag magnitude of the phase ph at the corresponding DAS
V_A	Recorded fault voltage at phase A by DAS. Used specifically as axis labels in the figures
V_{AN}	Used specifically as axis labels in the figures. Phase-neutral voltages for phase A
V_B	Recorded fault voltage at phase B by DAS. Used specifically as axis labels in the figures
V_{Load}	Voltage across the load
V_T	PV inerter terminal voltage at the point of common coupling
x	State variable
$\dot{x}$	Time differential of the state variable x
x_0	State variable in the initialization step
x_1	State variable of the current controller in PV inverters
$x_{1\alpha}$	x_1 under the α frame
$\dot{x}_{1\alpha}$	Time differential of $x_{1\alpha}$
$x_{1\beta}$	x_1 under the β frame
$\dot{x}_{1\beta}$	Time differential of $x_{1\beta}$
x_{1d}	x_1 under the d frame
$\dot{x}_{1d}$	Time differential of x_{1d}
x_{1q}	x_1 under the q frame
$\dot{x}_{1q}$	Time differential of x_{1q}
x_2	State variable of the current controller in PV inverters
$x_{2\alpha}$	x_2 under the α frame

$\dot{x}_{2\alpha}$	Time differential of $x_{2\alpha}$
$x_{2\beta}$	x_2 under the β frame
$\dot{x}_{2\beta}$	Time differential of $x_{2\beta}$
x_{2d}	x_2 under the d frame
$\dot{x}_{2d}$	Time differential of x_{2d}
x_{2q}	x_2 under the q frame
$\dot{x}_{2q}$	Time differential of x_{2q}
x_3	State variable of the PLL in PV inverters
$\dot{x}_3$	Time differential of x_3
x_4	State variable of the PLL in PV inverters
$\dot{x}_4$	Time differential of x_4
x_{n-1}	State variable in the step n-1
$\dot{x}_{n-1}$	Time differential of x_{n-1}
x_n	State variable in the nth step
$\dot{x}_n$	Time differential of x_n
x_{di}, x_{qi}	State variables under the dq frame of the PV inverter model
x_{dj}, x_{qj}	State variables under the dq frame of the OpenDSS circuit
$\overline{X}$	A m-dimensional vector of the predictor variables X_1, X_2, ... X_m
X/R	Reactance versus resistance ratio
X_α, X_β	Electrical quantities on the $\alpha\beta$ axis respectively
X_a, X_b, X_c	Electrical quantities on the abc axis respectively
X_d, X_q	Electrical quantities on the dq axis respectively
X_m	Peak value of the electrical quantity
X_i	Predictor variables in decision tree problems
y	Output of the state space functions

y_{PLL}	Output of the PLL
$Z(t)$	Integral of the fault current in one cycle
Z_0	Zero sequence impedance of the line
Z_2	Negative sequence impedance of the line
Z_f	Fault impedance
Δi	Output of the anti-islanding controller
Δv	Output of the BPF inside the anti-islanding controller
τ	Time constant of the decaying dc offset
θ	Rotating angle of the reference frame
$\dot{\theta}$	Frequency inside the PV inverter model
θ_i	Rotating angle of the reference frame inside the PV inverter model
θ_j	Rotating angle of the reference frame inside the OpenDSS circuit
θ_k	Phase angle of the hth harmonic component
θ_{sys}	Phase angle of the calculated voltage phasor in OpenDSS
θ_{PV}	Rotating angle of the reference frame in PV inverter model
θ_{PV1}, θ_{PV2}, θ_{PVn}	Rotating angle of the reference frame in PV inverter model 1 to n
Δt	A small time step
ε_{curr}	Current magnitude mismatch between the simulated and the measured values
ε_{curr1}	Current magnitude mismatch between the simulated and the measured values with fault resistance value of R_{f1}, used for illustration in the figure
ε_{curr2}	Current magnitude mismatch between the simulated and the measured values with fault resistance value of R_{f2}, used for illustration in the figure
ε_{curr3}	Current magnitude mismatch between the simulated and the measured values with fault resistance value of R_{f3}, used for illustration in the figure
ε_{curr4}	Current magnitude mismatch between the simulated and the measured values with fault resistance value of R_{f4}, used for illustration in the figure
$\varepsilon_{FeederDAS}$	Voltage sag error between the simulated case results and the measurements at feeder DAS

ε_{PVDAS}	Voltage sag error between the simulated case results and the measurements at PV DAS
ε_{total}	Total voltage sag error between the simulated case results and the measurements at feeder DAS and PV DAS
ω	Frequency of the system
ω_0	Reference frequency of the system
ω_c	Cut off frequency of the filter inside the power controller
ω_n	Rated frequency of the system

CHAPTER 1: INTRODUCTION

Technology advances, environmental concerns and ambitious renewable energy standards (RES) have led to an increasing interest in distributed energy resources. Distributed generation (DG) is of limited size (10MW or less) [1], and can be interconnected at different levels (substation, distribution feeder, or customer) in the electric power systems. DG technologies can run on fossil fuel, waste heat, and renewable energy resources such as PV and wind turbines. Among them, as an inexhaustible and clean energy source, solar energy has attracted much interest, and the PV markets are booming in the United States due to large demands and investments.

The positive impacts of high penetration of DG on distribution systems have been reported in the literature [1] [2] [3]. The main advantages of high penetration of DG in distribution systems are as follows:

- Emergency backup during outage
- Energy savings during peak electricity demand
- Reduced voltage sag and improved power quality
- Reduction of power loss
- Increased transmission and distribution system capacity
- Increased system reliability.

For a distribution system to benefit from DG, the DG is required to coordinate well properly with the existing distribution system elements. Several issues may arise when DG of different types and technologies are connected to the distribution systems.

1.1 Impacts of DG on distribution systems

Integrating DG in distribution systems influences both the power quality and the existing protection systems [1] [4-5]. From a power quality viewpoint, inclusion of DG can affect voltage regulation, losses, voltage flicker, voltage dips, harmonics and voltage unbalance in a distribution system. From a system protection viewpoint, adding DG can affect the existing overcurrent protection, coordination of protective devices and islanding. Details of the potential impacts of DG on distribution system are as follows.

Voltage regulation

Radial distribution systems have several regulation methods to control steady-state voltages, including substation transformers with load-tap-changing (LTC), substation feeder regulators, line regulators, and switched capacitors [6-7]. The voltage regulators are controlled to compensate for downstream voltage drops due to the line impedance. During heavy load conditions, the regulators increase the controlled voltage to alleviate low voltage problems in the feeder. During light load conditions, the voltage regulators reduce the controlled voltage to prevent overvoltages.

The introduction of DG affects the voltage profile along a feeder, by changing the direction and magnitude of power flows. The impact of DG on voltage regulation can be positive or negative, depending on the distribution system, DG characteristics, and DG locations [8-9].

If a DG is located downstream of a regulator with line-drop compensation, the DG may cause low voltages in the feeder. Under heavy load conditions, the DG reduces the load observed by the regulator, which makes the regulator set a lower voltage at the feeder.

The feeder voltage becomes lower with the DG than without the DG installed. Two possible methods can be adopted to solve this problem [1]. The first method is to move the DG upstream of the regulator, and the second method is to add regulator controls to compensate for the DG output.

DG can also cause unacceptably high voltages at the customer premises. In accordance with ANSI standards [60], during normal conditions, utilities in the United States are required to maintain customer voltages between 114 and 126 V (± 5%) based on a 120 V secondary voltage base. The DG located on the secondary side of the transformers can cause reverse power flow, which counteracts the normal voltage drop in the distribution transformers. The reverse power flow may cause the service voltage on the secondary side to be higher than that on the primary side of the distribution transformer. During light load conditions, if the primary side voltage is near or above the upper limit of 126 V, the installation of DG can cause the service voltage to exceed the ANSI upper limit.

Losses

One of the major impacts of DG is on the distribution system losses [1, 10-11]. Energy losses have been one of the metrics to assess the performance of the distribution systems. Substantial reduction in feeder losses can be achieved with the optimal placement of DG. Locating DG to minimize losses is similar to locating capacitor banks to reduce losses. The main difference between the two is that the DG may provide both active power and reactive power, while the capacitor banks only contribute reactive power. Since most DGs are owned by the customers, the DG locations cannot be determined by the utilities. Normally, losses are assumed to decrease when DG is placed near the loads. However, if

large-scale DGs are installed, the increased reverse power flow may exceed the thermal limit of overhead lines and cables.

Voltage flicker

Voltage flicker is caused by the fluctuation of energy resulting from intermittent generation or load, such as starting of an induction machine, or step changes in the DG output [12]. Slower power changes usually do not cause flicker problems. For example, the photovoltaic power output varies significantly with cloud movement, and voltage flicker problems may occur. In contrast, the change in sunlight intensity is so slow that severe voltage flicker problems are unlikely to occur. Identifying and solving the flicker problems need good models of the distribution system as well as the DG. Software analyses of the dynamic behavior of the systems are quite useful for this type of the study [13-15].

Harmonics

High penetration levels of DG may introduce significant harmonics in the distribution systems. Harmonics produced can be from the generation unit itself (synchronous generator) [16], or from the power electronics equipment such as inverters [17-19]. The IEEE 519-1992 standard [20] provides the acceptable levels of harmonics that may be injected into the system. PV systems are connected to the distribution systems through power electronic inverters. The inverters using insulated gate bipolar transistors (IGBT) employ pulse width modulation (PWM) techniques at relatively high switching frequencies (several kHz). The current injected by the inverters into the grid has low harmonic content at low frequencies. The harmonics at the switching frequency can be attenuated to acceptable levels by the use of the relatively small filters. In general, DG interfaced to the grid through a power

electronic converter produces lower harmonic distortion than other types of DG such as rotating generators. However, the impact of DG needs to be analyzed when a very large number of such inverter interfaced generation are installed in close proximity.

Increased level of fault current

Fault current level increases with the installation of DGs in the distribution systems [21-22]. The increase in fault current level is mainly due to the short circuit current contribution from a large number of inverters. However, the probability of the fault current level exceeding the interrupting current ratings of the protection devices due to installation of DG is low.

Impact on protection coordination

Installing DGs in the distribution systems can decrease the fault current flowing from the substation through the relay, thereby de-sensitizing the relay [23-24]. The protection coordination may be lost due to the increased fault current seen by the fuses and the reduced fault current seen by the relay. The effect of DG on protection system coordination depends on the amount of DG in the system, and the connections of the interconnection transformers. Detailed studies are needed to assess the impact of DG on protection device coordination in distribution systems.

The work presented in this report analyzes the impact of high penetration of PV based DG on the distribution system feeder voltages and protection coordination. The study has been performed on a realistic distribution feeder with high PV penetration and the results of the study are presented here.

1.2 Analysis of distribution feeders with high penetration of PV systems

A detailed model development and analysis of the distribution feeders with high penetration of the distributed PV resources is necessary for system design, improvement and future planning. Figure 1.1 shows several types of system analyses, including snapshot simulation, time-series simulation, dynamic simulation and fault simulation that were performed in this thesis.

The modeling and analyses performed in this work are based on a test bed distribution feeder. The complete geographic information system (GIS) database is available for the major feeder equipment and the conductor segments. In addition, the load and the PV data at a fine resolution can be obtained through the extensive advanced metering infrastructure (AMI) and other data acquisition systems (DAS).

The test bed feeder has been modeled in CYMDIST (CYME Distribution System Analysis Tool) [34] and OpenDSS (Open Distribution System Simulator) [35]. CYMDIST is a commercially available distribution system analysis tool, and OpenDSS is an open source tool. Both tools are capable of supporting the snapshot and quasi-static analysis, as well as the fault simulations. In addition, with the proposed dynamic modeling and interface method in this work, the dynamic analysis can also be executed in OpenDSS.

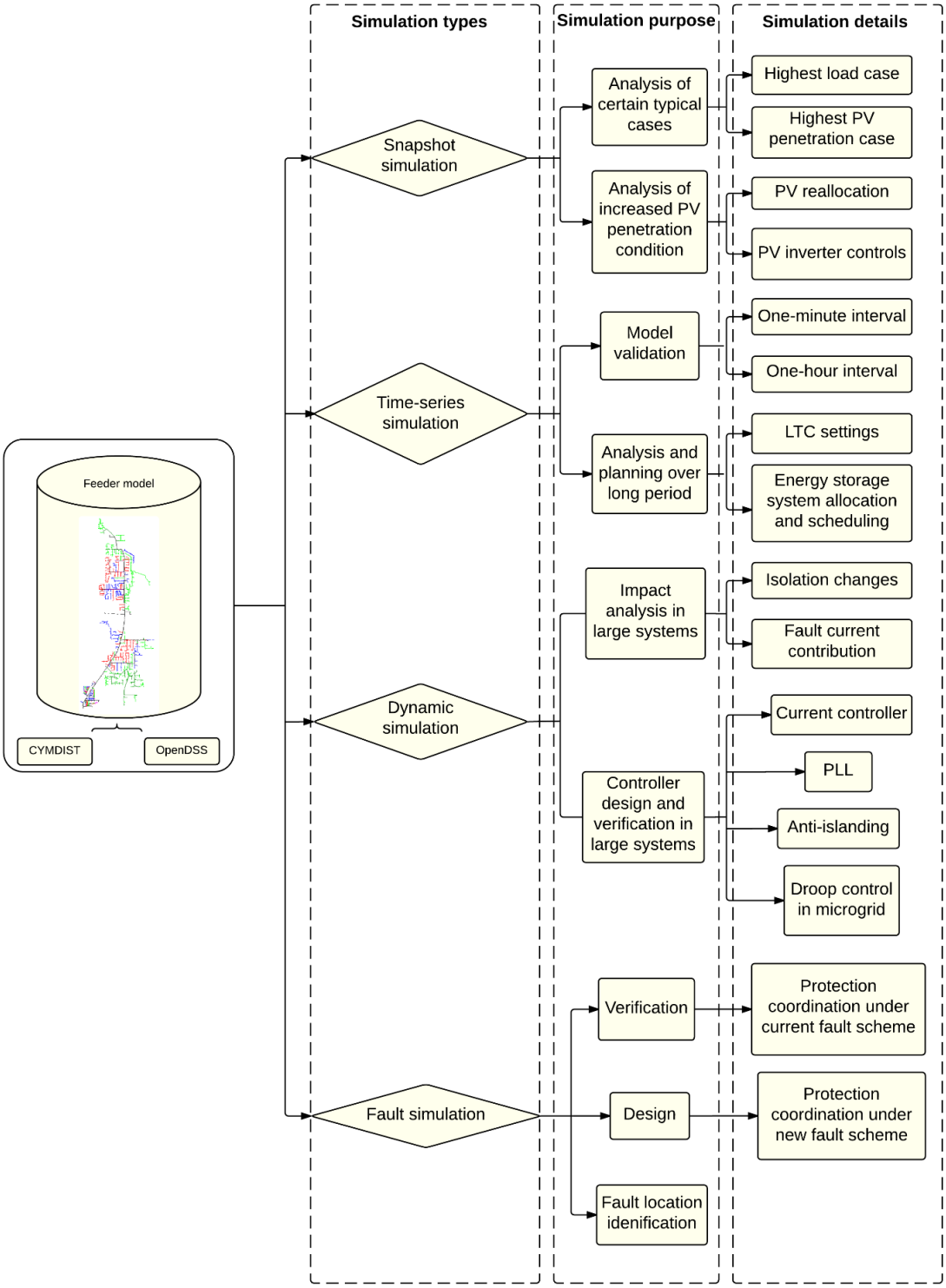

Figure 1.1 Simulations and analyses proposed in this work for the impact study of high penetration of PV systems

The snapshot analysis can be used for solving the power flow for the distribution systems in certain typical cases, such as the highest load case and the highest PV penetration case. The voltage profiles along the feeder can be obtained to study the voltage violations under current and expected penetration levels of PV generation. In addition, the snapshot simulation can help investigate the impact of PV on the feeder voltages under different feeder scenarios, such as reallocation of the PV systems and PV inverter reactive power support with variable power factors.

The time-series simulation, which involves a series of steady-state solutions, is an analysis of the distribution system over a day, month or year. On the basis of the snapshot analysis, the time-series analysis further includes the variation of the loads, PV generation and substation voltages over time. The study can be done with a time resolution of one-minute or one-hour interval depending on the data available and the study objectives. The time-series analysis helps verify the feeder model by comparing the simulation results to the field measurements, in terms of the feeder voltage profiles, active power flow and reactive power flow. Furthermore, using time-series analysis, the most suitable settings of the load tap changers in the transformers can be obtained, which help in system planning. The time-series analysis can also assist in the allocation and scheduling of energy storage based on the load and PV conditions in different seasons.

The existing distribution system analysis tools primarily conduct steady state and snapshot studies by solving network algebraic equations for different operating scenarios. Such steady state analyses typically require shorter simulation time. However, dynamic simulations are an integral part of distribution system analysis, and such studies are needed

to design, verify and improve the control of the inverter-interfaced DGs. Therefore, efficient techniques to perform dynamic analyses are needed to extend the capabilities of the distribution system analysis tools.

Electromagnetic transient programs (EMTP) [96-97] and positive sequence electromechanical transient programs (PSLF [119], PSSE [120], PowerWorld [121]) use differential or differential algebraic equations to conduct dynamic analyses in the time domain. EMTPs are typically used for detailed analysis of smaller portions of transmission or distribution system. EMTPs are useful because such tools can be used to develop detailed three-phase models of equipment to study systems, which may have unbalanced voltages and currents. Positive sequence electromechanical transient programs are primarily used to study the dynamic performance of the transmission systems, which are assumed to be balanced. Simulation of the large distribution networks using EMTP-type programs is computationally burdensome due to the large number of network elements (lines, transformers, shunt devices, generators and loads) that need to be modeled. The positive sequence electromechanical transient programs are not adequate here because of the inherent current and voltage unbalances that exist in the distribution systems.

In this work, a DAE based dynamic modeling and analysis of the PV inverters in large unbalanced distribution systems is proposed. A single-phase *dq* frame based method is proposed to build the inverter analytical model under unbalanced conditions. The dynamics of the PV inverter models are analyzed by solving differential equations written in dynamic link libraries (DLLs). The circuits built in OpenDSS are analyzed using algebraic equations. DLL is interfaced with OpenDSS circuits by importing and exporting electrical quantities in each dynamic step. The DAE based method takes much shorter computation

time as compared to the traditional EMTP solvers. Thus, this approach can be used to conduct dynamic analyses in large unbalanced systems.

In the study related to faults, the analysis is performed in the dynamic mode, and all generators in the system are converted to their corresponding Norton's equivalents. After a conventional power flow solution, a fault object, which is a multi-phase resistor branch with two terminals, is applied to the faulted phases. The solution then proceeds under the dynamic mode. Since the PV penetration may affect the protection coordination between fuses, reclosers and relays, a thorough analysis of the system protection coordination based on fault simulations is required. Distribution systems are primarily protected by fuses, and use either a fuse-clearing or a fuse-saving scheme. A detailed protection coordination analysis helps identify whether the existing protection schemes are sufficient under DG integration or a different scheme needs to be adopted.

An additional topic, which derives from the fault analysis of the distribution system, is the fault location identification. There are two aspects of the fault location in distribution systems: the first is to identify and isolate the faulted sections by protective devices, and the second is to locate the fault accurately. The two aspects are affected by the high penetration of PV systems. Under the detailed protection coordination analysis considering PV impacts, the protective devices can be re-designed to accomplish the first aspect. The second aspect also needs to be re-evaluated in the presence of the PV systems. An accurate and efficient fault location identification methodology is highly desirable in distribution systems. If the fault locations can be pinpointed quickly and accurately by utilities, the isolation of the faults can be done efficiently. In this way, the duration of the fault inter-

ruptions is reduced and the system reliability is improved. This thesis has proposed a complete approach including both fault type identification and fault location identification with PV systems in the distribution feeders. In order to eliminate the impacts of the fault current contribution of the PV systems on the identification process, methods based on fuzzy logic and decision-tree are adopted. The fault identification process is implemented using OpenDSS, MATLAB, Fuzzy Logic Toolbox in the MATLAB environment and CART (Classification and Regression Trees) [36]. The proposed identification method was verified using actual fault data, which were obtained from the measurements made by the utility.

1.3 Literature review

The work proposed in this thesis comprises of five major parts:

1. Distribution system modeling and verification in CYMDIST and OpenDSS
2. Steady-state analysis of the impacts of PV on the feeder voltages
3. DAE based dynamic modeling and analysis of the PV inverters
4. Protection coordination analysis of distribution systems with distributed PV generation
5. Fault location identification in the distribution systems with distributed PV generation.

The following sub-sections present a detailed review of the relevant work that has been done on these topics and published in various literatures. The thesis further proposes the improvements that can be made to the existing work.

1.3.1 Distribution system modeling and verification

In previous analyses of the distribution systems [31-33], relatively small feeders were built in distribution system analysis tools due to the lack of the GIS data for large feeders. In addition, loads were usually defined as constant power loads, constant current loads and constant impedance loads. The assumptions made on the load models causes significant discrepancies in the analyses results.

With the complete GIS database and the fine resolution measurements from AMI and DAS available, an automated modeling process for the distribution feeder starting from the GIS database, equipment standard, and device settings to the final detailed feeder model is proposed here. This work has utilized a zone-division methodology, which divides the feeder into several segments based on the locations of DAS. By using the zone-division method, the load and PV outputs are modeled in a finer resolution. The simulated voltages and powers were verified by comparing these quantities to that obtained from different measurements. Based on the comparison results the feeder models were found to be accurate. Chapter 2 describes the modeling and verification procedure of the actual distribution feeder used in this study in details.

1.3.2 Steady-state analysis of the PV impacts

The previous work has investigated the potential voltage violations caused by the distributed resources in the electrical distribution systems [37-39]. In order to alleviate the overvoltage problems, [40-41] proposed the method of the power curtailment of reactive power by using energy storage systems. [42] proposed and verified the advantages of the coordinated control of the distributed energy storage system with tap-changing transform-

ers. [43] demonstrated the benefits of leveraging the reactive power capabilities of the inverters in improving the voltage profiles. [44-46] have evaluated the impacts of various PV penetration levels at several locations in different feeders. Furthermore, the maximum PV penetration levels were obtained for each feeder under study.

Based on the verified feeder model, this thesis examines the impacts of different levels of PV penetration on the feeder voltages in relation to:

1. Reallocation of PV systems
2. Reactive power support from the PV inverters
3. Settings of the LTC transformers in coordination with the PV penetration and load variation.

Design recommendations are proposed based on the simulation results to improve the feeder voltage profiles in the real feeder studied.

1.3.3 DAE based dynamic modeling and analysis of the PV impacts

EMTP programs (PLECS [96], PSCAD [97], MATLAB/Simulink [122]) are capable of modeling and analyzing the dynamics of converter interfaced generation (CIG) using small time-steps in unbalanced conditions. However, analyzing the operations of CIG in large distribution systems using such programs is computationally burdensome. A typical distribution system contains hundreds or thousands of laterals and sub-laterals. A detailed time-domain analysis using differential equations of such extended system requires substantial computation time. On the other hand, existing distribution system analysis tools (OpenDSS [98], CYMDIST [34], GridLab-D [99]) can only be used to perform steady-state and quasi-static analysis on large unbalanced distribution systems.

Several articles have addressed the dynamic modeling of CIGs in transmission level [100-102], and validation in smaller systems. The positive sequence converter models developed for CIG are suitable for the transmission level analysis, due to the balanced nature of the transmission systems. However, the unbalanced nature of the distribution systems, which include transposed lines, single-phase laterals and unbalanced loads, present challenges in the development of CIG models. [103] proposed a method using MATLAB via the OpenDSS COM interface for implementation of DER volt-watt controls in distribution systems. The method did not implement the dynamic model of CIGs, and the need of multiple iterations for one actual time-step takes extra computation time. [104] implemented a three-phase unbalanced dynamic model of synchronous machine in GridLAB-D. The dynamic models were successfully validated and studied in microgrids. However, the focus of this work on the CIG modeling, which includes modeling of filters, controls, and phasor locked loop (PLL) is different from the synchronous machine modeling proposed in [104]. [105] introduced the modeling of induction machines and three-phase PV unit in DLLs. [104] also presents a method to interface the PV generator model with OpenDSS for unbalanced dynamic analysis in distribution systems. This method offers a way to perform dynamic studies for large distribution systems based on DAEs. Additionally, the use of DLLs helps protect the proprietary information for inverter vendors. However, details of the modeling and testing in large systems are not presented in [105].

Based on [105-107], this thesis proposes the modeling of PV inverters for unbalanced dynamic studies in large distribution systems. The key contributions of this thesis compared to the previous work are as follows:

1. A single-phase *dq* frame design is proposed to help the unbalance modeling of the PV inverters
2. A complete modeling of the basic components of the PV inverters, including filters, current control loop and PLLs, is implemented and validated
3. Thorough dynamic analyses of the PV inverters in large unbalanced distribution systems, including the grid-connected mode of operation, islanding detection, and droop controls in microgrids are conducted.

The focus of this thesis is to develop unbalanced dynamic model of the PV inverters that can be interfaced to the distribution system analysis tool OpenDSS. Simple, generic controls are used in the modeling process, to illustrate the capability of the proposed method to effectively perform large distribution system dynamic analyses. This thesis lays a foundation for the verification of future advanced control designs in large systems, and breaks the previous limitations of verification in small systems only by EMTPs.

1.3.4 Protection analysis under PV impacts

The analysis of the impact of PV on protection systems can be sub-divided under three primary topics:

- Impact of interconnection transformer configurations
- Impact of PV on protection coordination
- Solutions to the protection coordination problems.

Impact of interconnection transformer connections

The selection of the interconnection transformer configuration affects how PV interacts with the distribution systems. [47] has investigated thoroughly the problems and advantages of different connections of the interconnection transformers. Connecting the high

voltage (HV) side as delta or ungrounded wye has an advantage of restricting the zero sequence current to avoid affecting the utility ground relay coordination. However, overvoltage issues may occur during a ground fault on the utility side due to the undergrounded connection. Connecting the HV side as wye and the low voltage (LV) side as delta establishes a zero sequence current source during ground faults. This affects the coordination between protective devices, although no overvoltage problems are associated with this type of connection.

With different interconnection transformer connections, PV systems will have different impacts on the ground faults and phase faults. The study provides a complete mathematical evaluation of how the settings of the protective devices should be changed to avert problems arising from different transformer connections.

Impact of PV on protection coordination

Topics on the potential loss of the protection coordination due to PV impacts have been frequently visited in literature [26, 28-30, 47, 50].

For the existing coordinated fuses, fault contributions from upstream PV systems could increase the minimum and maximum fault currents seen by the fuses. When fault current contribution is large enough, the increased fault current could exceed the ratings of the fuses, and the fuse coordination may be lost. When the PV system is located downstream of a fuse, the fuse may be unnecessarily opened during upstream faults due to the PV fault current contribution.

The recloser-fuse coordination is also affected under the fuse-saving scheme. The installation of the PV systems will decrease the sensitivity of the recloser, and may result in slower operation of the recloser compared to the existing coordinated fuses.

This thesis thoroughly discussed the impact of PV on fuse-fuse coordination, recloser-fuse coordination, relay-fuse coordination and relay-recloser coordination under both fuse-clearing and fuse-saving schemes. Recommendations based on the study are also presented here.

Solutions to the protection coordination problems

Several techniques have been introduced in the literature as possible solutions to the coordination problems caused by distributed generation.

[51] has recommended the use of microprocessor-based devices with predefined curves instead of the relay and reclosers in the distribution systems. A different solution was proposed in [52] by using remotely communicated and controlled breakers. In [52], the distribution system is divided into several zones by the breakers, and the fault zone is isolated by tripping the corresponding breakers through a remote control. Both solutions require high initial equipment costs for replacement and thus may be impractical.

[53] investigated the threshold capacity value of the distributed generation, beyond which recloser-fuse coordination is lost. This solution puts a limit on the penetration levels of the distribution system. In a similar way, [54] proposed a classification technique to find the suitable settings for recloser and distributed generation. This approach is based mainly on two steps, the first step is to search for the best locations of the distributed generation, and the second step is to change the recloser settings. However, the IEEE 37-node test feeder selected for the study is relatively small for adequately representing a practical distribution system. In addition, the settings for the recloser and fuses are derived from equations rather than the device manufactures, which may significantly affect the findings of the study.

To alleviate the discrepancies, this thesis proposes an automated methodology to find the suitable settings of the reclosers and relays in the large feeder, under different PV penetration levels. Thousands of coordinated cases are considered and the settings are found by solving the formulated nonlinear optimization problems.

1.3.5 Fault location identification in the distribution systems

The fault location identification approaches can be classified into five subcategories as follows:

1. Superimposed components method [55-56]. In this method, the superimposed values of voltage and current at any assumed fault point are determined from the differences between the total fault and prefault steady-state voltage and current signals. The assumed fault point is varied systematically until the superimposed current in healthy lines is found to be a near zero value. This method does not yield unique results for the fault location
2. Intelligent system method. [57-59] have proposed a method based on intelligent systems such as neural networks, fuzzy logics and decision-trees. This method requires a large number of training data, and the re-training process is needed whenever the power system structure is changed
3. Impedance based method. [60-67] have utilized the impedance-based method for fault location identification. In this method, the total reactance between the substation and the fault location is defined as the ratio of the selected voltage to the selected current, based on different fault types and faulted phases. In [63], a real-world fault location system is described based on the proposed method. [64-67] have investigated the various aspects of the impedance-based method, including heterogeneity

of the distribution system lines, load current impacts, and lack of substation voltage measurements. Due to the reliance of this method solely on measured voltage and current signals at the substation, multiple estimations of the fault location are obtained

4. Traveling wave methods. The methods based on traveling waves generated by the fault have been suggested in [68-70]. The high frequency sampling requirement in this method increases the implementation costs. This method is more applicable to transmission systems where lines are longer and better monitoring devices are equipped
5. Voltage sag based methods. Based on the gathered data from meters installed along the distribution feeders, the voltage-sag based method is proposed in [23, 71-74]. The distinctive feature of the voltage sag based fault location is the capability of differentiating faults on different laterals with the same accumulated impedance seen from the substation. In [71], the fault is applied at each feeder node, and the simulated voltages at the meters are recorded and compared to the measured values. The node with the minimum values of the voltage match at all meters is selected as the faulted node. [72] has improved the previous method by narrowing down the potential faulted area using the decision-tree method. In [72-73], fault resistance values are estimated by comparing the simulated substation fault current to the measured ones with varying fault resistance values.

With the fault event data available from several DAS installed in the studied feeder, the voltage sag based method is utilized in this thesis. Based on the method proposed in [71], this work further improves the accuracy of the fault location identification combining

the use of fuzzy-logic and decision-tree. [59, 71-72] verified their proposed methods from simulation results, while this thesis uses the event data from the real fault cases.

The fault current contribution from PV systems is also taken into consideration in this thesis. Some literature has discussed the algorithm of the fault location identification in the presence of DGs. [74] has developed a superposition-based approach to locate the faults, while the method proposed cannot locate the fault exactly on the faulted section. [75] proposed a fault location identification method by using synchronized voltage and current measurements at the interconnection of DG, and the fault location can be pin-pointed accurately. However, the during-fault measurements of the voltage and current are not always available, if the fault occurs far away from DG and the meter at DG is not triggered during the fault.

In this work, PVs are modeled as current injection sources during the faults, and the fault currents contributed are calculated based on the during-fault voltages at the PV terminals. Based the validated feeder model, simulations are run with PV fault contribution included, and the fault locations are identified by the voltage-sag based method proposed.

1.4 Thesis organization

This thesis conducts the steady-state analysis, quasi-static analysis, dynamic analysis and protection coordination analysis for distribution feeders with high penetration of PV generation. In Chapter 1, the potential impacts of DG on the distribution systems have been discussed, and the various simulation types to study the impact of PV have been introduced. A thorough review of the published relevant literature is also presented in this chapter.

Chapter 2 describes the detailed steps of the distribution feeder modeling. The zone division method has been used for load and PV output allocation, as well as the verification of the feeder model. In addition, the various aspects of the PV impacts on the voltage profiles are studied in this chapter. Recommendations are proposed based on the simulation results to improve the feeder voltage profiles in the studied feeder.

Chapter 3 proposes the modeling and interface of PV inverter for unbalanced dynamic analysis. The analytical models of the PV inverters including filters, controllers, and PLL are constructed based on the single-phase *dq* frame. The model is written into DLL and interfaced with OpenDSS circuits. Dynamic analyses including faults, reference changes, anti-islanding controls and droop control in microgrid are conducted.

In Chapter 4, a novel methodology is proposed to define the settings of the recloser and relay based on different connections of the PV interconnection transformers, PV penetration levels, and fault types.

Chapter 5 demonstrated a novel fault location identification method, which is expected to greatly improve the reliability of the system. The event data obtained from the real fault cases are used for the verification of the method proposed.

Chapter 6 concludes the contributions from each type of the simulation conducted in this work. In addition, future work is proposed to further study the dynamic behavior of the PV inverters in large distribution systems with improved controls.

Appendix A lists the number of buses violating the ANSI limit in each hour of the day with the selected LTC tap settings, for the test feeder studied in this work.

CHAPTER 2: MODELING AND VERIFICATION OF THE DISTRIBUTION FEEDER WITH HIGH PHOTOVOLTAIC SYSTEM

2.1 Introduction

The penetration levels of the distributed renewable resources, especially solar photovoltaics, in power distribution systems are increasing at a rapid rate. However, distribution systems were traditionally not designed to accommodate such generation resources. The rapid increase in penetration levels of such sources has raised concerns over the potential voltage violations, loss of protection coordination and reduction of the system reliability on the distribution feeders.

In order to understand the impact of high penetration of the inverter-interfaced PV, this work has conducted an extensive study on the subject of modeling and analysis of the distribution systems, based on a test bed distribution feeder located in Flagstaff, Arizona. This work is part of the five-year project sponsored by Department of Energy (DOE) [95], and some of the publications are listed in APPENDIX B. The test feeder was chosen from over 20 feeders, since the feeder meets the following criteria [95]:

- PV penetration level is above 15% of the feeder peak load
- Sufficiently available land area for 500 kW PV arrays
- Sufficient area in substation for future energy storage systems
- Sufficient mix of commercial to residential customers
- Sufficient residential rooftops with south-facing exposure.

The details of the test feeder are listed in Table 2.1. The test feeder has been modeled in CYMDIST and OpenDSS. Several other tools including MATLAB, Excel and

ArcCatalog were used to process data, develop component models and control the power flow engine. In addition, a thorough verification of the feeder modeled has been conducted by comparing the simulated results to the field measurements at different DAS locations. Based on the verified feeder model, the snapshot and time-series simulations have been conducted to study the PV impacts on the system voltages and the protection coordination.

Table 2.1 Details of the test bed distribution feeder

Feeder length	10 miles
Peak load	7 MW
Feeder capacity	13 MW
Number of customers	Residential: 3000
	Commercial: 300
Number of primary segments	1810
Number of secondary segments	2738
Number of transformers	929
Number of fuses	182
Number of capacitor banks	3
Utility scale PV system 1 rating	400 kW
Utility scale PV system 2 rating	500 kW
Number of residential PV systems	107
Residential PV generation	300 kW

2.2 Modeling procedure of the test feeder

Figure 2.1 illustrates the overall, automated modeling process, starting from the required data to the generation of the complete feeder model in both CYMDIST and OpenDSS. The developed model is suitable for the power flow and other analyses under different load and PV conditions.

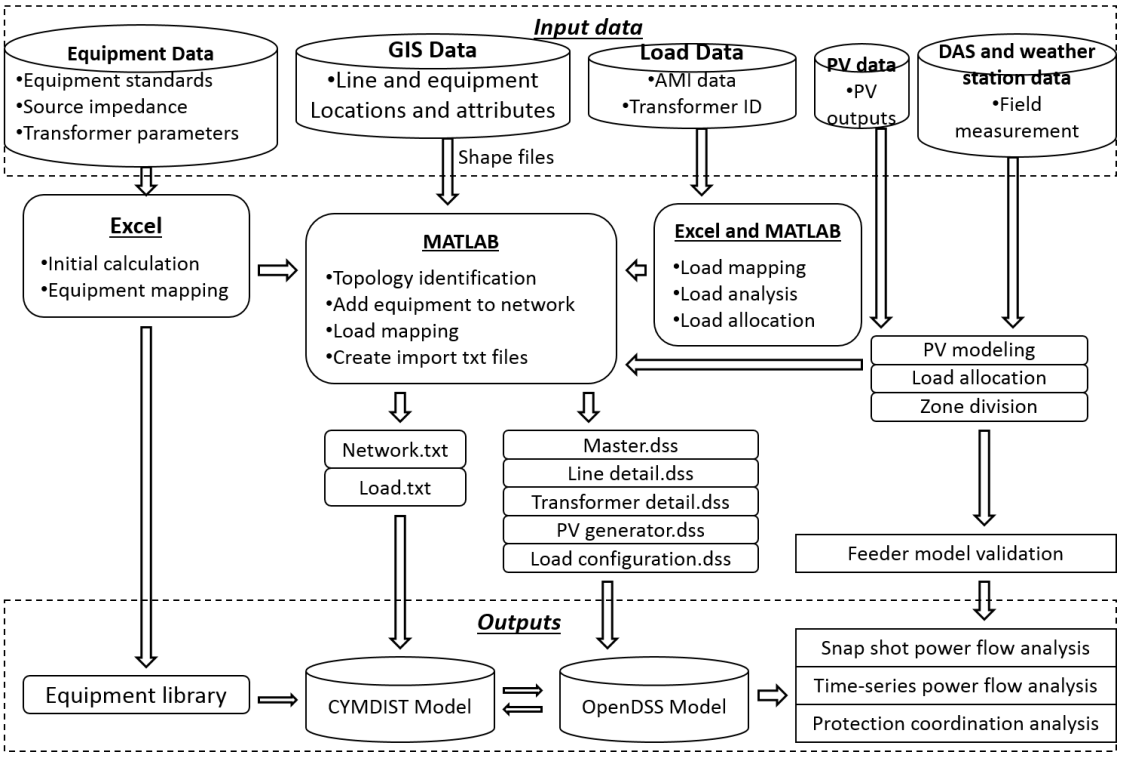

Figure 2.1 Overview of the modeling process proposed in this work to study high penetration PV in distribution feeders

To generate the complete system model, three distinct parts that can be generated and integrated independently are required. The three distinct parts are as follows:

- Equipment model. The equipment library contains the definitions of all the equipment that are used in the circuit model

- Network model. The network model is the physical model of the system, and it contains detailed information about what equipment is present in the system and how each device is connected
- Load and PV models. The load and PV models include the locations and the data to be used for the power flow study.

The input data obtained from the utility are processed by several tools and programs. The data are then imported into CYMDIST and OpenDSS to generate the three models. The details of the various stages in the modeling process are presented in the following sub-sections.

2.2.1 Distribution system input data

As indicated from Figure 2.1, GIS data are required for the detailed modeling of the feeder. The GIS data provide the locations and information such as equipment type and rating for all the line segments and equipment on the feeder. In addition, construction standards of the electric utility for line conductors including standards on spacing, transformer impedance data, protection devices and their settings are used. Finally, the load data (real power and measured or estimated power factor) at the required resolution and the PV system outputs are needed for the accurate distribution system analysis.

2.2.2 Building the equipment model

The first step in the equipment modeling involves identifying all the different types and subtypes of various devices used in the distribution system. Then the various devices are modeled, and the models are added to the equipment library with unique equipment ID. For example, the feeder modeled has 1810 primary feeder segments. These segments fall under 39 line types, namely 25 overhead line cables and 14 underground cables. These 39

line types in turn make use of different phases, neutral conductors and spacing models created in the equipment library.

The original input data are processed to obtain the parameters and are converted to the format required by CYMDIST or OpenDSS. The data are then used to construct the equipment library. For the feeder modeled in this work, there are equipment libraries for lines, transformers, capacitor banks and feeder equivalent sources at the substation. Details of all the equipment libraries are as follows:

- Equipment library of the feeder lines. Feeder lines are composed of overhead lines and underground cables. With the line types given from the utility GIS data, and sizes, stranding, GMR, diameters, resistance and spacing values of line conductor components found in the utility standards and handbooks [75], the line geometry is defined and line impedance is calculated in CYMDIST/OpenDSS
- Equipment library of the transformers. The impedance values, *X/R* ratios, and turns-ratios of transformers (single phase and three phase) are found from relevant standards based on their kVA ratings. These values are then recorded in the library
- Equipment library of the capacitor banks. The values of the rated power and rated voltage are recorded in the library
- Equipment library of the feeder equivalent source. The feeder generation, transmission system and the substation transformer that serve the feeder are represented by a Thevenin equivalent source. The impedance of the source is defined by looking from the low voltage side of the substation transformer into the system.

2.2.3 Building the network model

The network model is constructed with a set of MATLAB programs, as illustrated in Figure 2.2. The main procedure for the network modeling is as follows:

- Reading shape files. In the GIS data, each equipment (i.e. transformers, fuses, switches, reclosers) is a point type feature, meaning that they have the geometry of a point when shown on the GIS map. The distribution lines are line type features. The GIS data given in personal geodatabase (.mdb) format are converted to shape file (.shp) using ArcCatalog, and are read into MATLAB
- Topology identification. The topology identification process is needed to find the electrical connections of the line segments and the equipment devices. By starting from one random line end, a tree structure is expanded and created. The tree structure contains a set of nodes (buses), a set of sections (branches), and the indices of the *from node* and *to node* of each section
- Associating conductors with sections. The sections representing lines known from the GIS data are linked to the corresponding line/cable types defined in the equipment libraries
- Adding equipment. Each transformer in GIS data is represented by one point, but usually implemented as a two-terminal element in OpenDSS. Hence, a new node for each transformer is created. Since the transformer primary nodes are treated as the points provided in GIS data, the secondary line sections are changed to connect with the new created nodes representing the transformer secondary points.

2.2.4 Building the load and PV models

The load and PV models are created as the last step of the feeder modeling procedure. To obtain a finer resolution for the load kW and kVAr values and the PV outputs, a zone division method is used in this work. The zone division method also helps to construct a system that closely matches the real system conditions. The zone division is based on the feeder DAS locations. The proposed method makes use of the high-resolution feeder DAS data and the low-resolution AMI data for the allocation of the loads and PVs. The zone division method is implemented in MATLAB, and the resulting load and PV output data are written into OpenDSS to run the time-series simulations.

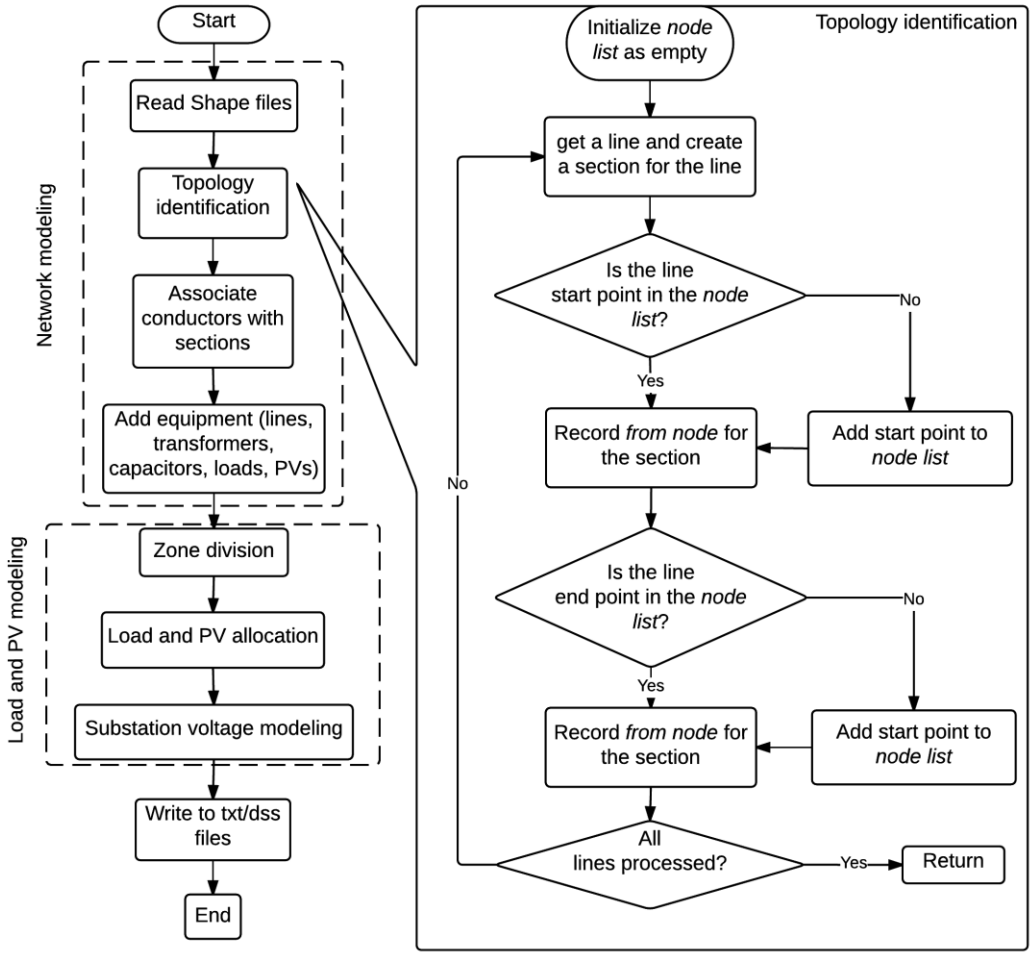

Figure 2.2 Network modeling, load and PV modeling process in MATLAB

In the modeled system, there are 6 feeder DAS systems along the feeder. These DAS systems use the Schweitzer Engineering Laboratories' (SEL) SEL-735 power quality meter to collect the parameters. Additionally, there are 17 residential DAS systems at residential PV installations using the SEL-734 power quality meter to collect the data. The DAS system measurements are of one-minute-interval and one-second-interval. AMI meters are installed for all the customer loads and PV systems, and the AMI meter measurements are of one-hour-interval or 15-minute-interval for a small number of customers [77-78]. Figure 2.3 shows the feeder diagram with the locations of the feeder DAS 1 to 5 and the substation

DAS marked clearly. Based on the feeder DAS locations, starting from the substation at the bottom of the feeder diagram downstream to the feeder end, the feeder has been divided into five zones.

The load kW values at 1-minute-interval resolution are obtained from the zone division using mainly the 1-minute-interval data from the feeder DAS measurements. The 15-minute-interval or 60-minute-interval data from the load and PV AMI are also used for scaling. In each zone, the total DAS kW measurements of each phase are scaled by the proportion of each load to the total load of the AMI data of the same phase in that zone.

Similarly, for power factor allocation, the total kVAr and kW values for each phase are obtained in each zone. The capacitor bank operation is judged from the DAS kVAr values in time sequence. The influence of the capacitor bank operation is then deducted from the kVAr values of each phase. The averaged line capacitance values, obtained from prior model simulations, are also deducted from the kVAr values of each phase. The power factor values for each phase in each zone then can be calculated from the deducted kVAr values and the total kW values.

With the available DAS data, the substation voltages in simulations are adjusted to match the measured substation voltages from the substation DAS. Since distribution system analysis tools such as OpenDSS do not directly allow dynamically variable circuit source voltages, another voltage source with time-series values corresponding to field measurements is added to the feeder head.

Completion of all the above modeling processing steps results in the equipment model, network model and PV and load models being fully defined in MATLAB. The model data are written in CYMDIST and OpenDSS formats. The written data are imported

into the respective tools to create the complete feeder model. The described procedure for developing the feeder model in both CYMDIST and OpenDSS is entirely automated. Figure 2.3 to Figure 2.5 show the one-line diagram of the resulting CYMDIST and OpenDSS model, together with the original GIS figure for a comparison.

2.3 Verification of the feeder model

For the verification purpose, one-minute interval time-series simulations for one-month periods have been run for the distribution system model in OpenDSS. Figure 2.6 to Figure 2.9 shows the comparison between the simulated results and the measured DAS data for the model validation for a one-day period. The active power, reactive power and voltages have been compared. The comparisons of the quantities in the figures are only displayed for a single phase. All other phases have similar results and hence omitted for the sake of brevity.

Figure 2.6 shows the comparison between the measured and simulated one-minute-interval kW plot of phase A at the substation DAS for a single day. As seen in Figure 2.6, the modeled kW values are following the DAS kW measurements closely, with the zone division method adopted. This is true for the other DAS systems as well.

To illustrate the output kW from the PV systems in the feeder, the simulated kW values at DAS 4 with PV systems and without PV systems are plotted together in Figure 2.7. As seen in Figure 2.7, with the installations of PV systems, the total supplied kW at the DAS 4 decreases between 7 AM and 5 PM.

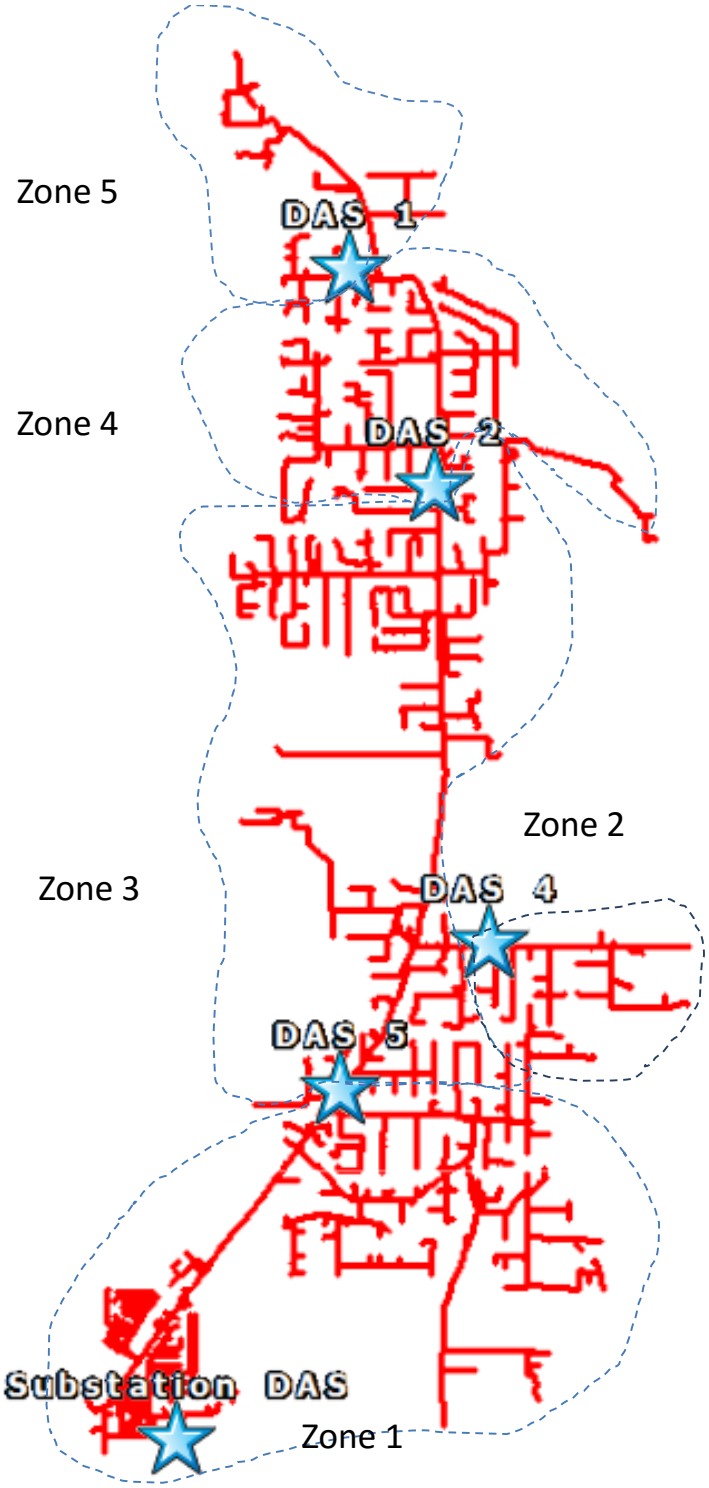

Figure 2.3 The GIS view of the feeder

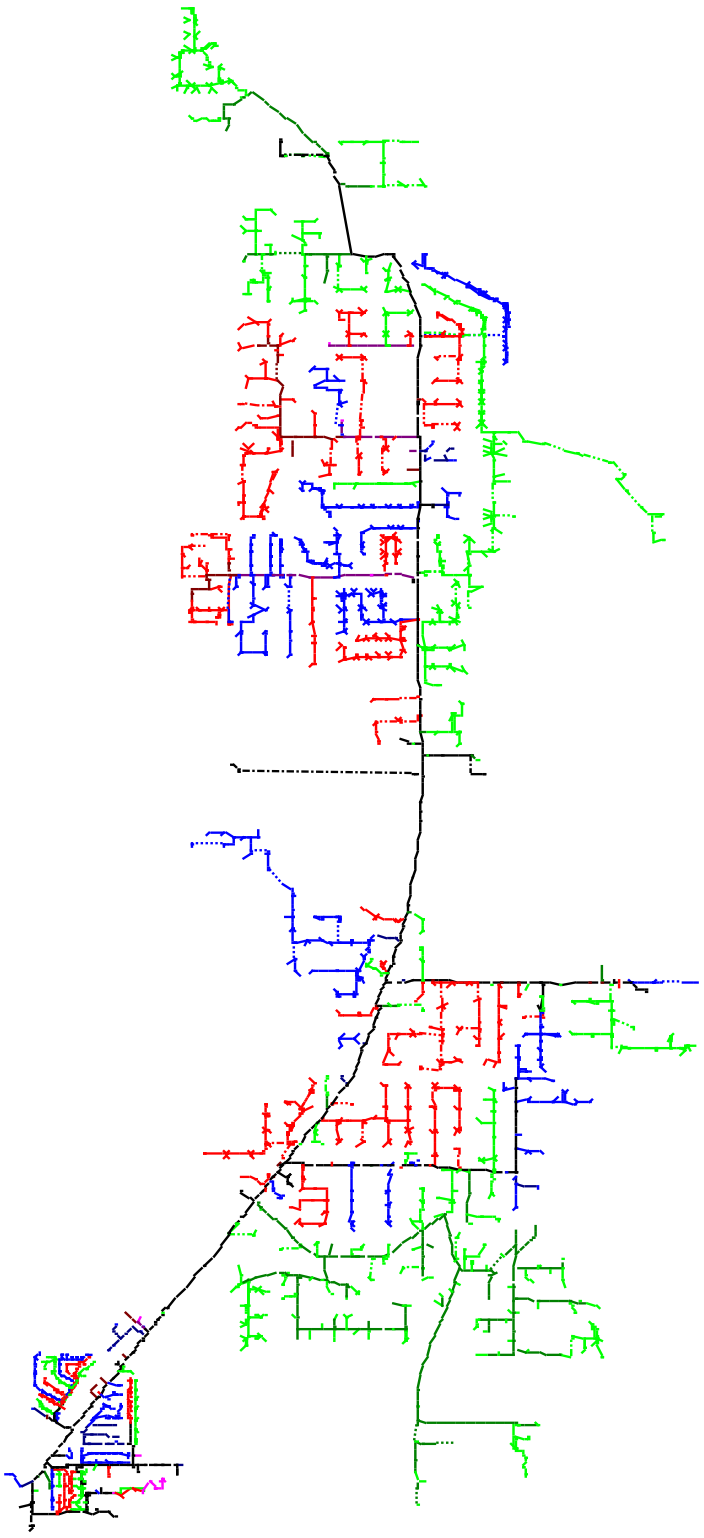

Figure 2.4 The one-line diagram of the feeder in CYMDIST

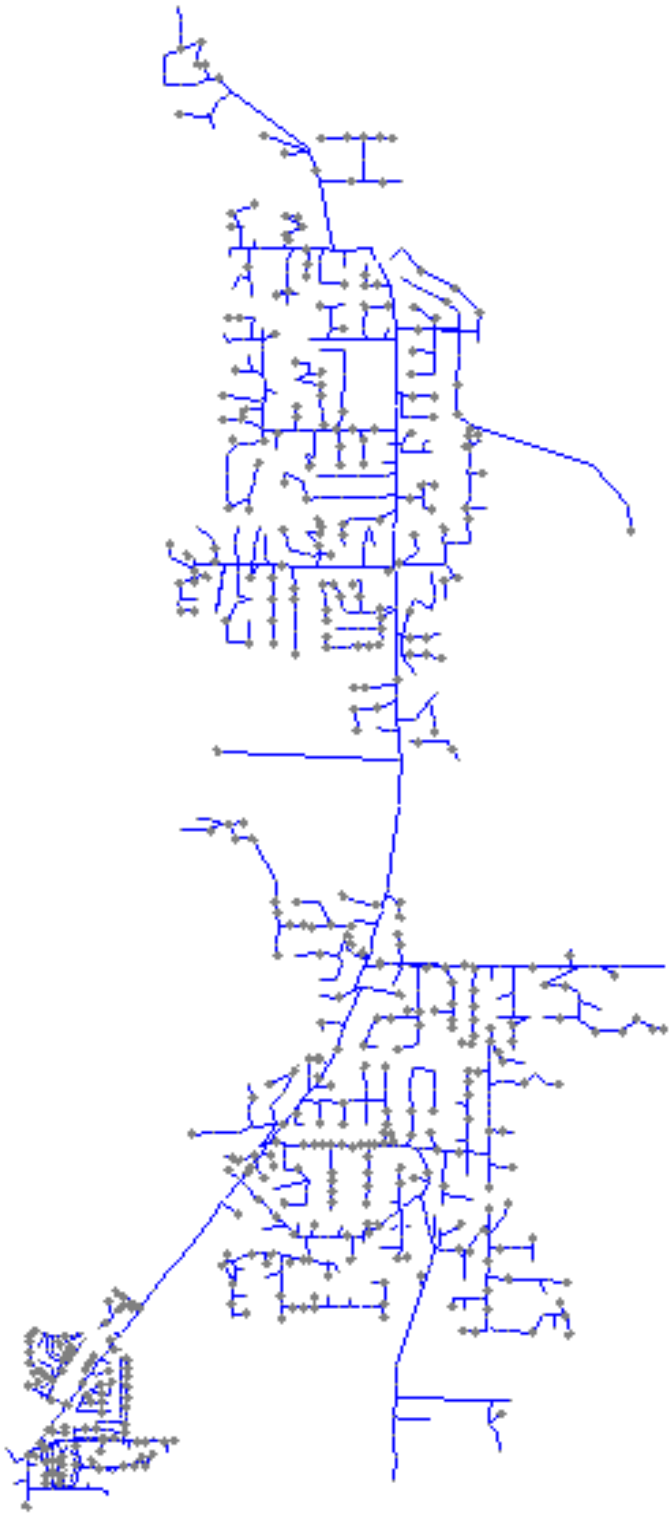

Figure 2.5 The one-line diagram of the feeder in OpenDSS

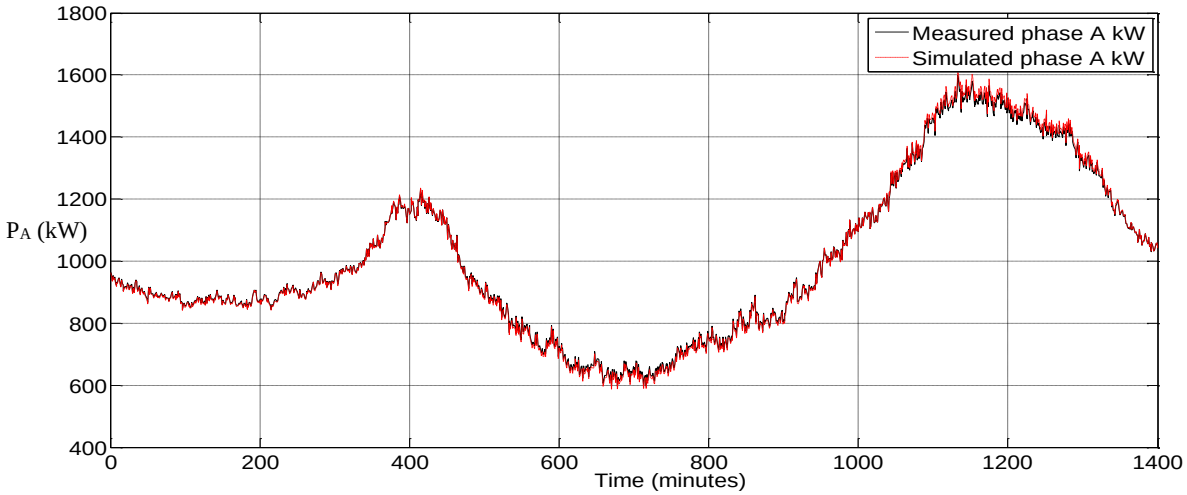

Figure 2.6 Measured and simulated substation one-minute-interval kW plot of phase A over a day – October 2, 2012

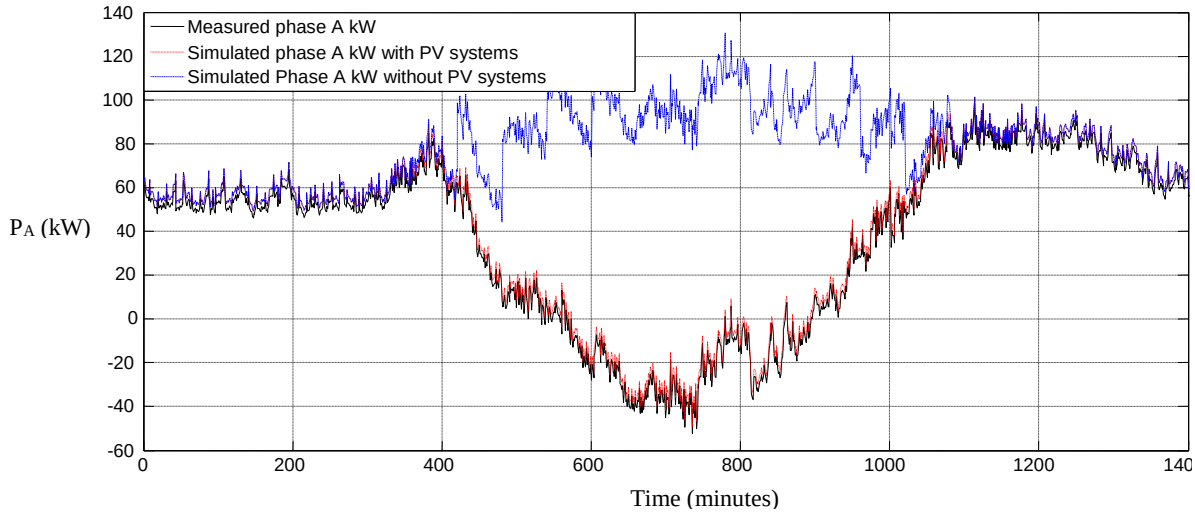

Figure 2.7 Measured and simulated DAS04 one-minute-interval kW plot of phase A over a day – October 2, 2012

Figure 2.8 shows that the simulated kVAr values with capacitor bank operations matches the real measurements at DAS 5 closely, based upon the DAS kVAr allocation procedure. In general, small changes in the voltage profiles make the timing of the actual and the simulated capacitor bank operations quite different, and hence lead to mismatching errors in the kVAr plot. Figure 2.8 shows the comparison of kVAr for day when the differences between the kVAr profiles are small.

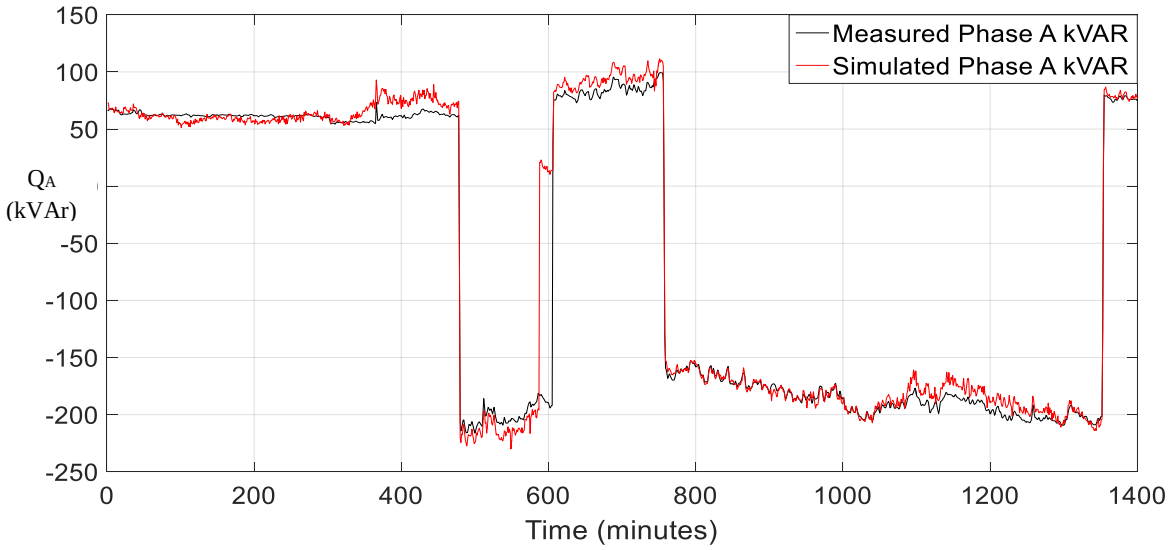

Figure 2.8 Measured and simulated substation one-minute-interval kVAr plot of each phase over a day – October 2, 2012

When the substation voltage is modeled to follow the measured DAS voltage, the modeled feeder voltage values are closer to the real conditions. Figure 2.9 shows the comparison between the measured and simulated voltage plots of phase A at DAS 5, which is at the middle of the feeder, and at DAS 1, which is located near the end of the feeder. As seen from Figure 2.9, the simulated voltage values match the measured data closely throughout the feeder. To better illustrate the difference between the measured and simulated voltage profiles, Table 2.2 lists the RMS percent error between simulated and measured voltage magnitudes for each phase at various DAS locations in the same day. As seen from Table 2.2, the RMS percent error in the voltage magnitudes is less than 1.5%. This indicates that the developed model closely represents the actual system with minimal error.

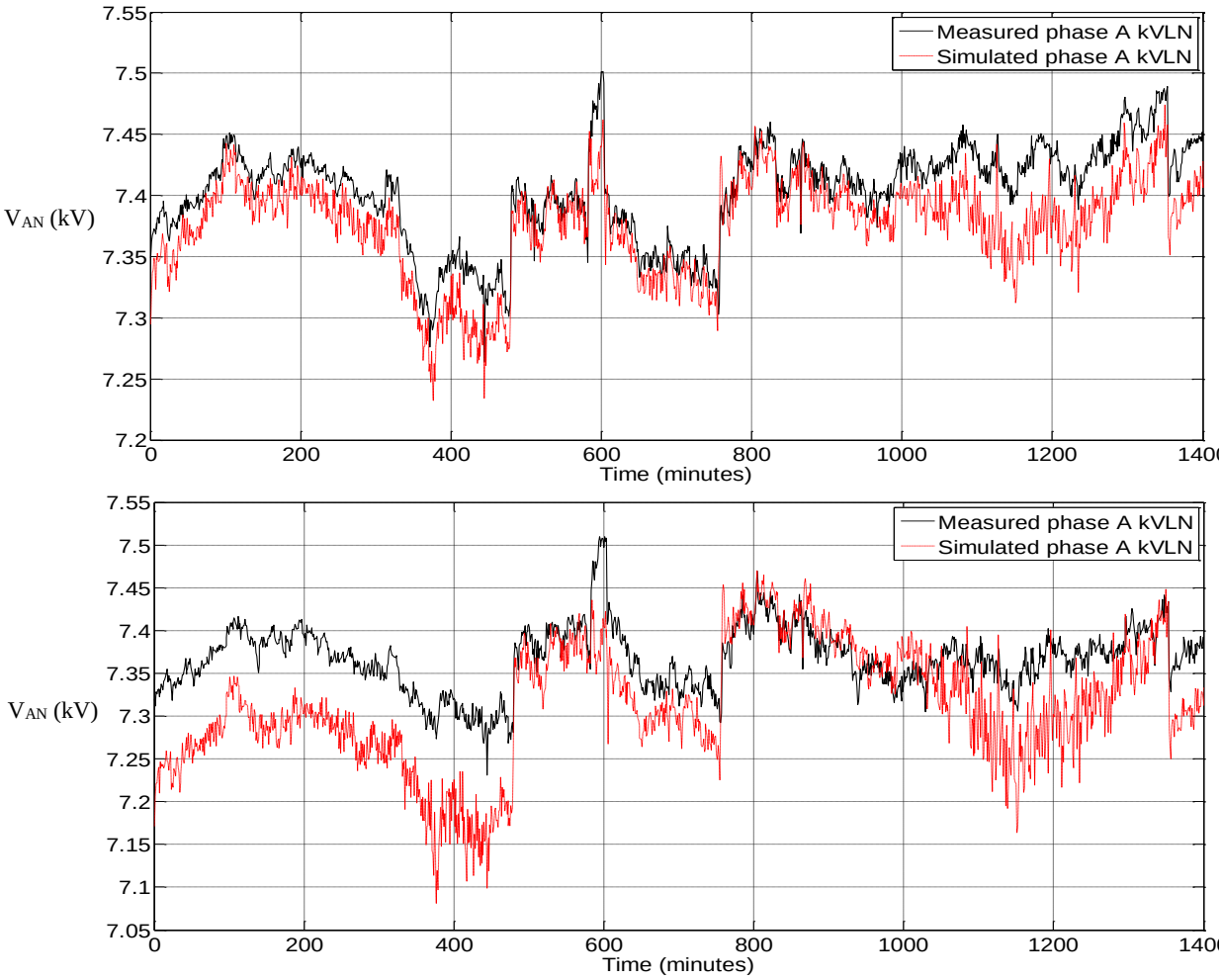

Figure 2.9 Measured and simulated DAS 5 and DAS 1 one-minute-interval voltage plot of phase A over a day – October 2, 2012

Table 2.2 RMS percent error between simulated and measured voltage magnitudes for each phase at various DAS locations over a day – October 2, 2012

	Substation (%)	DAS05 (%)	DAS04 (%)	DAS02 (%)	DAS01 (%)
Phase A	0.00	0.38	0.45	0.60	0.85
Phase B	0.15	0.37	0.40	0.64	0.85
Phase C	0.28	0.63	0.56	1.16	1.34

2.4 Steady state analysis of the feeder model

To study the impact of PV on the test feeder, the verified feeder model for the year 2014 has been chosen. The load and PV data for this particular year were provided by the utility. Simulations were performed for two operating conditions. The two operating conditions represent the highest load case and the highest PV penetration case in the year 2014.

By summing up the load data at each hour in the year 2014, the highest load case was found to occur at 8 PM on Jan 5, 2014. The substation voltage was measured as 1.028 p.u. for this case. The operating parameters for the highest load case simulated in CYMDIST are given in Table 2.3. As seen in Table 2.3, the generation from PV is negligible due to the low insolation at the late evening hour in the winter.

Table 2.3 Operating parameters in the highest load case

Parameters	Real power (kW)	Reactive power (kVAr)
Total load	5484.24	2707.20
Total PV generation	0	0
Total losses	176.76	359.78

The highest penetration case in the year 2014 was found at 12 PM on March 24, 2014. The substation voltage was measured as 1.028 p.u. for this scenario. The PV penetration level used in this study is defined in (2.1). Based on (2.1) the PV penetration level in the highest penetration case is 41.97%. The operating parameters in the highest penetration case are given in Table 2.4.

$$\text{PV penetration} = \frac{\text{PV power generation}}{\text{Feeder head power} + \text{PV power generation}} \times 100\% \qquad (2.1)$$

Table 2.4 Operating parameters in the highest penetration case

Parameters	Real power (kW)	Reactive power (kVAr)
Total load	2977.81	1508.89
Total PV generation	1249.81	0
Total losses	32.56	49.31

2.5 Analysis of the impact of PV and recommendations

The main purpose of the feeder modeling is to perform an in-depth analysis of the impact of PV on the distribution system operation. In this section, the developed model is simulated under different operating scenarios to find the maximum allowable penetration levels of PV, such that the feeder voltages are maintained within ANSI Range A voltage limits [79]. The studies have been divided in two categories:

1. To study the effect of placement of PV at different locations in the feeder
2. To study the effect of allowing PVs to perform reactive power control.

In addition, the use of LTC has been studied with the historical load and PV data to alleviate the feeder voltage violation problems. The details of the studies are presented in the following sub-sections.

2.5.1 Impacts on voltage profile under varying levels of PV penetration

To analyze the impacts of the PVs at various locations, 7 different scenarios are studied. Four scenarios of the small residential PVs and three scenarios of the large-scale PVs have been developed. Before generating these scenarios, the electrical distances from each transformer load to the substation were calculated and sorted. The accumulated electrical distance can be calculated and sorted for every feeder node based on the feeder topology and the parameters of all the line sections. The details of each scenario are listed as follows.

Small residential PVs

- PV scenario 1: Small-scale PV clustered near substation source
- PV scenario 2: Small-scale PV clustered near midpoint of the feeder
- PV scenario 3: Small-scale PV clustered near the end of the feeder
- PV scenario 4: Small-scale PV on all load points.

To produce the scenarios 1-3, residential PV systems are successively added to the transformers that are ranked according to the location requirement of the scenarios. This is continued until the desired PV penetration level is reached. The PV systems are sized as 20% of the corresponding transformer rating. For example, to create scenario 3, a residential PV system is added to the transformer, which is farthest from the substation. Then another PV is added to the transformer second-farthest from the substation. The process is continued until the desired PV penetration level is reached. To produce the scenario 4, residential PV systems are added to all the transformers, and are sized equally with the total PV outputs reaching the desired PV penetration levels.

Scenarios 1-4 are run with the loads under the highest PV penetration case, and the PV penetration levels are progressively increased from 10% to 100% of the total feeder loads. Under each penetration level for each scenario, the maximum feeder voltages are found and listed in Table 2.5. As seen in Table 2.5, the PV penetration levels can be increased to 100% in scenario 1, 40% in scenario 2, 10% in scenario 3, 90% in scenario 4, without violating the maximum voltage limit (1.05 p.u.).

Large-scale PVs

- PV scenario 5: One large-scale PV located close to the feeder head, with another large-scale PV located at original location

- PV scenario 6: One large-scale PV located near the feeder midpoint, with another large-scale PV located at original location
- PV scenario 7: One large-scale PV located at the end of the feeder, with another large-scale PV located at original location.

The loads corresponding to the highest penetration case are used to study the PV impacts under the three large-scale PV scenarios. Table 2.6 shows the maximum primary voltage simulated under different scenarios and PV penetration levels. As seen in Table 2.6, the PV penetration levels can be increased to 100% in scenario 5, 80% in 6, and 40% in scenario 7, without violating the maximum voltage limit (1.05 p.u.).

As indicated from Table 2.5 and Table 2.6, the maximum achievable PV penetration generally decreases while the average distance from the PV systems to the feeder head increases.

Table 2.5 Maximum feeder voltage (p.u.) under different scenarios and penetration levels of the small residential PVs

PV scenarios / PV penetration levels	1	2	3	4
10%	1.0279	1.0289	1.0458	1.0278
20%	1.0285	1.0328	1.0534	1.0279
30%	1.0292	1.0394	1.0527	1.0280
40%	1.0298	1.0456	1.0566	1.0307
50%	1.0306	1.0507	1.0515	1.0343
60%	1.0302	1.0552	1.0551	1.0378
70%	1.0319	1.0586	1.0592	1.0413
80%	1.0319	1.0622	1.0596	1.0447
90%	1.0377	1.0637	1.0598	1.0481
100%	1.0431	1.0610	1.0519	1.0514

Table 2.6 Maximum feeder voltage (p.u.) under different scenarios and penetration levels of the large-scale PVs

PV scenarios / PV penetration levels	5	6	7
10%	1.0288	1.0295	1.0315
20%	1.0298	1.0310	1.0377
30%	1.0310	1.0327	1.0438
40%	1.0330	1.0352	1.0497
50%	1.0359	1.0386	1.0555
60%	1.0387	1.0418	1.0612
70%	1.0414	1.0450	1.0668
80%	1.0441	1.0481	1.0722
90%	1.0467	1.0511	1.0776
100%	1.0493	1.0541	1.0828

2.5.2 Impacts on voltage profile with reactive power support

The large-scale inverters can be designed to regulate their terminal voltage (or the voltage at a remote bus) by closed-loop control. The relevant settings and parameters can be changed remotely by the utility operator. These inverters have advanced features including volt/VAr control, volt/watt control, frequency based curtailment, full range of power factor control (0 to 1 leading and lagging) and sufficient margin for reactive power even while injecting rated active power.

The residential-scale string inverters currently operate only at unity power factor. Depending on the topology used, many of the string inverters are also capable of providing on-demand reactive power support and variable power factor operation. Based on the emerging products from inverter manufacturers, in the near future, the string inverters are expected to be capable of autonomously injecting reactive power and/or operate at fixed power factor mode.

Having a large reserve capacity to inject reactive power at the rated kW generation is not cost effective. Therefore, the design of the string inverters may restrict a wide range

of power factor. Emerging products from inverter manufacturers are expected to support up to 0.9 lagging and leading power factor. In this section, extensive analyses are carried out to determine the effectiveness of the VAr control features in both the residential and the commercial grade inverters to mitigate the voltage issues arising from high penetration of PV in the distribution system.

In the highest PV penetration case, the maximum feeder voltage is found under 1.05 p.u., which is within the prescribed ANSI voltage limit. Therefore, a base hosting capacity case with a PV penetration level of 59.64% is defined, where the maximum feeder voltage is exactly 1.05 p.u.. To demonstrate the improvements in the PV hosting capacity by allowing reactive power support from both large-scale and residential-scale PVs with different power factors, the PV penetration level at the base hosting capacity are increased by 15%, 25% and 50% and the voltage profiles are studied. Table 2.7 shows the maximum voltage at any bus (including the feeder secondary sides) on the feeder under the considered high PV penetration scenarios.

Table 2.7 Maximum voltage (p.u.) at different PV penetration levels

Power factor lagging	PV at base hosting capacity	PV at 15% above base hosting capacity	PV at 25% above base hosting capacity	PV at 50% above base hosting capacity
0.99	1.0454	1.0467	1.0476	1.0526
0.98	1.0433	1.0444	1.0451	1.0472
0.95	1.0393	1.0396	1.0399	1.0406
0.9	1.0381	1.0381	1.0381	1.0381

As seen from Table 2.7, reactive power is absorbed by each of the inverters at a power factor of 0.9. The reactive power support from the inverters allows the PV penetration to be increased by an additional 50% above the base hosting capacity without violating the ANSI voltage limits.

Based on the results from Table 2.7, the residential inverters (typically in the 2 kW to 8 kW range) are recommended to have a kVA rating of at least 1.11 times the maximum kW rating of the corresponding PV arrays. This corresponds to a reactive power capacity of 48.4% of the rated active power, when the inverters are injecting the rated active power.

The inverters should also have the capability to adjust the PV operating power factor from unity to 0.9 lagging and leading. The control settings for the reactive power injection will be fixed at the time of installation, and the inverters then operate autonomously based on the settings and local measurements such as terminal voltage and frequency. The settings will be determined based on the distribution system characteristics such as the stiffness ratio, *X/R* ratio, specific location along the feeder, and proximity to voltage control devices and larger PV plants. The settings can also be changed as new devices, new PV systems and loads are added.

2.5.3 Reduction of the voltage violation by changing LTC settings

As indicated from Table 2.7, the reactive power support from the PV inverters results in significant improvement of the voltage profiles at high level of PV penetration. A substantial increase in PV hosting capacity can be also obtained without needing reactive power support from PV inverters. This can be achieved by appropriate tap selections of LTCs, based on the variation of loads and irradiance. With the measurements of the loads

and PV output data available for the year 2014, the one-hour-interval time-series simulation is applied for the whole year. In this way, the proper settings of LTC can be obtained with the least number of buses violating the ANSI limits in that year. In addition, considering the possibility of increase in the PV penetration, the time-series simulation can be also re-applied with increased PV penetration levels. This analysis assists in the future planning of the distribution system operation.

In this section, to analyze the effect of proper LTC tap selection at the substation, 8 LTC tap settings ranging from 0.98 p.u. to 1.05 p.u. in 0.01 p.u. steps are considered. The one-hour-interval time-series simulation is run for a whole day (the day with the highest PV penetration case is used) with the 8 tap settings respectively. Analyses have been conducted under different high penetration scenarios.

- *The base hosting capacity case*

For each time step in the chosen day (the day with the highest PV penetration), all PV generations are scaled up by the same factor to reach a maximum penetration level of 59.64% (penetration level of the base hosting capacity case). The one-hour-interval time-series simulation is applied with the scaled up PV generation. Table A.1 and Table A.2 in appendix A lists respectively the number of buses where the voltage values were beyond the upper limit and below the lower limit respectively, for each hour of the day and with the selected tap settings.

For a tap setting of 1.0 p.u., which represents the original case without LTC at the substation, 744 buses violate the ANSI limit in the whole day. If none of the LTC taps are changed, the LTC tap setting of 0.99 p.u. is the most suitable one with total 144 buses violating the ANSI limit in the whole day. If the LTC taps are allowed to change in the day,

the LTC tap settings in the corresponding hour listed in Table 2.8 lead to a reduced total number of 95 buses violating the ANSI limit in the whole day.

Table 2.8 LTC tap settings proposed in the base hosting capacity case

Hours of the day	LTC tap settings
Hour 1 to hour 7	Tap of 0.99 p.u.
Hour 8 to hour 23	Tap of 1.01 p.u.
Hour 23 to hour 24	Tap of 0.99 p.u.

- *15% and 50% scaled up of the base hosting capacity case*

To study this case, the PV generation is scaled up by a factor of 1.15 and 1.50 of the base hosting capacity case respectively. A time-series analysis is applied, and the number of buses where the voltage values are beyond the ANSI prescribed limit in each hour with the different tap settings are recorded.

In the case of 15% increase in PV penetration from the base hosting capacity, 743 buses were found to violate the ANSI limit in the whole day without LTC. The total number of buses where voltage violations occur can be reduced to 94 by adopting the LTC settings listed in Table 2.8.

In the case of 50% increase in PV penetration from the base hosting capacity, 745 buses were found to violate the ANSI limit in the whole day without LTC. The total number of buses where voltage violations occur can be reduced to 91 by adopting the LTC settings listed in Table 2.8.

From the results presented in this section, it can be concluded that the requirement of reactive power support from a smart inverter can be significantly reduced with the proper use of LTC.

CHAPTER 3: DYNAMIC MODELING AND ANALYSIS OF UNBALANCED DISTRIBUTION FEEDER WITH PHOTOVOLTAIC SYSTEMS

3.1 Introduction

Distribution system analysis tools are capable of performing steady-state and quasi-static analysis on large unbalanced distribution systems. The impacts of PV systems on the feeder, which include voltage changes, LTC transformer operations and capacitor switching operations, can be analyzed in one-minute or one-hour interval simulations. These simulations are done by solving the network algebraic equations with updated load and generation data for each minute or each hour. However, dynamic simulations involving the solution of differential equations cannot be performed using most of the commercial distribution system analysis tools.

Capturing the dynamic performance of the PV inverters is necessary, especially in large distribution systems. The distribution system analysis tools usually assume that the controller transients of PV inverters have settled down and the system has reached a steady state. However, an improper design of the controller can cause instability and some of the distribution system and PV transient changes may be faster in comparison to the relevant control bandwidth of inverters. The assumptions usually made in the existing distribution system analysis tools have largely ignored these issues. The EMTP-type solvers are capable of analyzing the dynamic behavior of the inverters for small systems. However, these tools are not practical for dynamic studies in large distribution systems. Additionally, the positive sequence electromechanical transient simulators are not adequate for distribution system studies as distribution systems have inherent voltage and current unbalances.

This work proposes an approach to model the PV inverter for unbalanced dynamic analysis. The PV models are stored in DLLs, which are interfaced with the OpenDSS network model. A method to interface the DLLs containing the dynamic model of the PV inverters to OpenDSS is also discusses here. At each time-step of the dynamic simulation, the time-domain current outputs from the inverter model are calculated based on differential equations. OpenDSS treats the inverters as Norton equivalents, and calculates the electrical phasors based on algebraic equations. The DAE based method shortens the computation time required for performing dynamic simulation with the inverter models in large distribution systems.

This chapter illustrates single-phase *dq* frame based implementation of the PV inverter, the creation of the inverter analytical model, and validation and analysis of the inverter through dynamic simulations.

3.2 Design of three-phase unbalanced PV inverter

The generic average model of the PV inverter including the PV filter, the current controller and the PLL is shown in Figure 3.1.

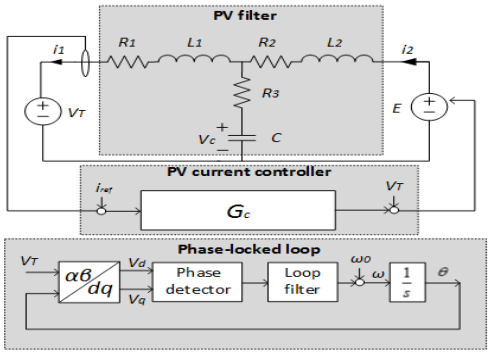

Figure 3.1 Average model of the PV inverter

In Figure 3.1, R_1, L_1, R_2, L_2, R_3 and C are the components of the PV filter. V_T is the PV inverter terminal voltage at the point of common coupling (PCC), and E is the controller output. i_1, i_2 and V_c are the state variables representing the current flowing through the inductor L_1 (also the current output of the PV inverter), the current flowing through the inductor L_2, and the voltage across the capacitor C respectively. i_{ref} is the current reference for the PV current controller.

Embarcadero Delphi [108] is used to develop the DLL containing the PV inverter model shown in in Figure 3.1. Figure 3.2 (a) shows the interaction between the DLL and network model in OpenDSS. Simulations in OpenDSS are based on the phasor values of the electrical quantities, while the outputs from the DLLs are instantaneous values. As shown in Figure 3.2 (a), during the dynamic simulation, at each time step, OpenDSS calculates the bus voltages based on the known output of the current sources, by solving the network algebraic equations. The calculated voltage phasors in the form $|V| \angle \theta sys$ are read by the PV inverter model in the DLL. Based on the differential equations, the values of the PV inverter output current *i(t)* is calculated and is exported to the network model built in OpenDSS. Since *i(t)* is the instantaneous current, the peak current value as well as the current phasor angle cannot be computed until one cycle of the instantaneous current values are gathered and calculated.

The synchronous reference frame (*dq* frame) is used to solve the discrepancy between the phasor values obtained from OpenDSS and instantaneous values from the PV inverter model. The transformation from the *abc* frame to the *dq* frame is given by [123] as

$$\begin{bmatrix} X_d \\ X_q \end{bmatrix} = \frac{2}{3}\begin{bmatrix} \cos(\omega t) & \cos(\omega t - \frac{2\pi}{3}) & \cos(\omega t - \frac{4\pi}{3}) \\ -\sin(\omega t) & -\sin(\omega t - \frac{2\pi}{3}) & -\sin(\omega t - \frac{4\pi}{3}) \end{bmatrix}\begin{bmatrix} X_a \\ X_b \\ X_c \end{bmatrix} \quad (3.1)$$

$$\begin{bmatrix} X_a \\ X_b \\ X_c \end{bmatrix} = \begin{bmatrix} \cos(\omega t) & -\sin(\omega t) \\ \cos(\omega t - \frac{2\pi}{3}) & -\sin(\omega t - \frac{2\pi}{3}) \\ \cos(\omega t - \frac{4\pi}{3}) & -\sin(\omega t - \frac{4\pi}{3}) \end{bmatrix}\begin{bmatrix} X_d \\ X_q \end{bmatrix} \quad (3.2)$$

where, X_a, X_b and X_c are the electrical quantities under the *abc* frame, and X_d and X_q are the transformed electrical quantities in the *dq* frame. The balanced electrical quantities X_a, X_b and X_c are instantaneous values, calculated as $X_m cos(\omega t)$, $X_m cos(\omega t - \frac{2\pi}{3})$ and $X_m cos(\omega t + \frac{2\pi}{3})$, where X_m is the peak value of the sinusoidal waveform.

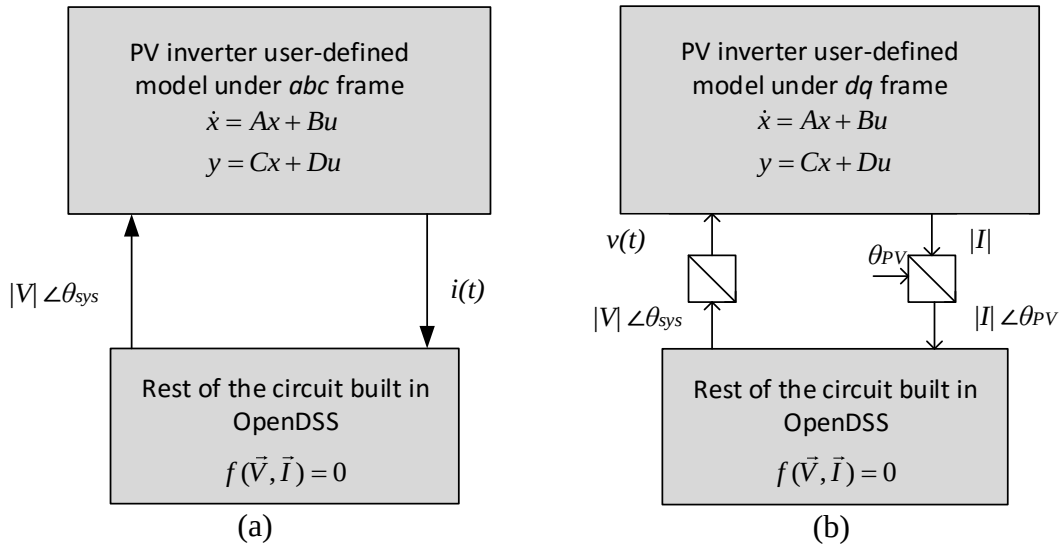

Figure 3.2 Original (a) and improved (b) interactions between the DLL and OpenDSS

By assuming a rotating *dq* frame, the state variables in the DLL can be solved as dc quantities. The calculated current values in the *dq* frame can be transformed back to the phasor values in the *abc* frames, based on the angle θ_{PV}, measured with respect to the *d*

frame. By this process, the PV inverter current *i(t)* is converted to the phasor $|I| \angle \theta_{PV}$ in OpenDSS. This transformation process is shown in Figure 3.2 (b).

The transformation from the *abc* frame to the *dq* frame given by (3.1) and (3.2) can only be used for three-phase balanced electrical quantities. Since the distribution system is unbalanced, the transformation method has to be modified to account for the unbalanced electrical quantities.

3.2.1 Single-phase dq frame design

The implementation of the *abc* frame to *dq* frame transformation for unbalanced electrical quantities requires the intermediate alpha-beta transformation for each phase. Before transforming the electrical quantities in the *abc* frame to the *dq* frame, the transformation between the *abc* frame and the *αβ* frame is executed. For example, for phase *a*, the *α* axis is assumed to be along the *a* axis, and the *β* axis is constructed by assuming a fictitious axis with 90° delay from the *a* axis. A single-phase electrical quantity $X_m cos(\omega t)$ is used to illustrate the *αβ* frame, where X_m is the peak value of the sinusoidal waveform. The *αβ* frame representation of $X_m cos(\omega t)$ is given by

$$\begin{bmatrix} X_\alpha \\ X_\beta \end{bmatrix} = \begin{bmatrix} \cos(\omega t) \\ \sin(\omega t) \end{bmatrix} X_m \tag{3.3}$$

where, X_α and X_β are the transformed electrical quantities under the *αβ* frame. The fictitious *β* axis helps in the *dq* transformation for each phase of the PV inverter. As shown in Figure 3.3 (a), by using the fictitious *β* axis, each phase of a plant in the *abc* frame can be transformed into the *dq* frame by

$$\begin{bmatrix} X_d \\ X_q \end{bmatrix} = \begin{bmatrix} \cos(\omega t) & \sin(\omega t) \\ -\sin(\omega t) & \cos(\omega t) \end{bmatrix} \begin{bmatrix} X_\alpha \\ X_\beta \end{bmatrix} \tag{3.4}$$

where, X_d and X_q are the electrical quantities under *dq* frame, X_α and X_β are the electrical quantities under *αβ* frame.

The controller outputs in the *dq* frame can be transformed to the *αβ* frame using by

$$\begin{bmatrix} X_\alpha \\ X_\beta \end{bmatrix} = \begin{bmatrix} \cos(\omega t) & -\sin(\omega t) \\ \sin(\omega t) & \cos(\omega t) \end{bmatrix} \begin{bmatrix} X_d \\ X_q \end{bmatrix} \tag{3.5}$$

where, X_α and X_β can then be transformed further to the *abc* reference frame.

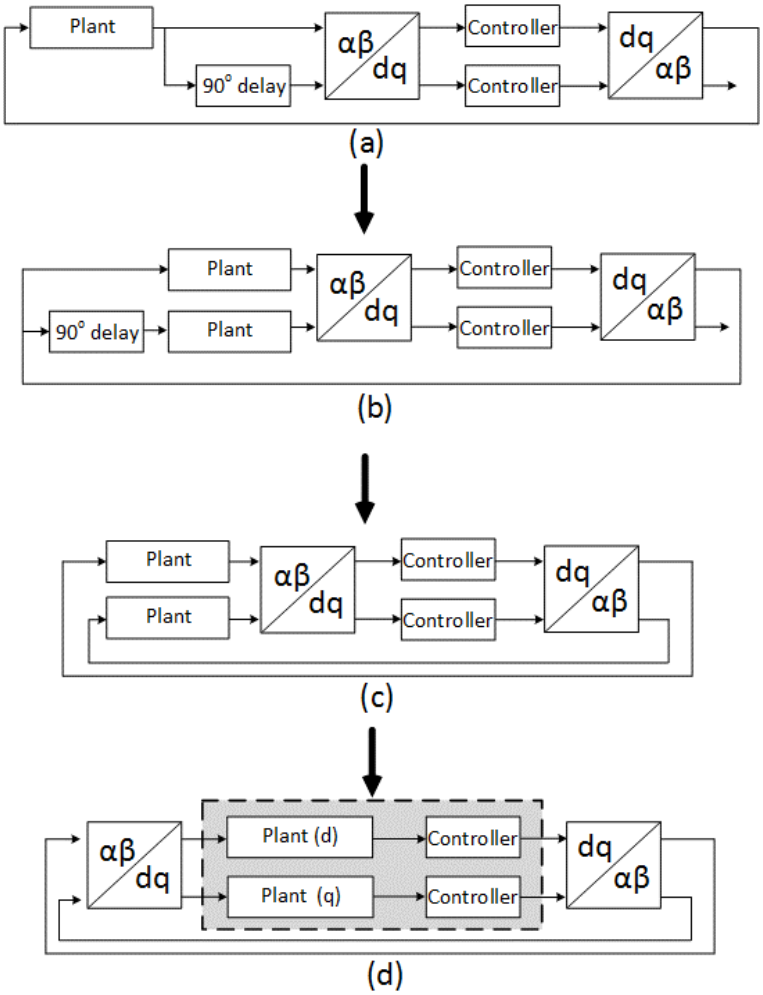

Figure 3.3 Frame transformation process for each phase of the PV inverter

By moving the 90° delay from the output of the plant to the input of the plant, as shown in Figure 3.3 (b) and Figure 3.3 (c), each phase of the PV inverter can be analyzed

as a two-phase system. Following this process, the PV inverter quantities can transformed to the *dq* frame, as shown in Figure 3.3 (d).

With the assumption of the fictitious β axis, each phase of the PV inverter can be implemented in the *dq* frame. By this method, the PV inverter can be modeled analytically under unbalanced operating conditions.

3.2.2 Switching of the reference frame between the PV inverters and the outside circuit

Based on the single-phase *dq* frame transformation, the output current $|I| \angle \theta_{PV}$ from the DLL containing the PV inverter model is injected into the network built in OpenDSS. θ_{PV} is the output current phasor angle with respect to the reference frame of each PV inverter. In this work, each PV inverter is modeled on its individual reference frame, whose rotation frequency is set by its own PLL.

The reference frame of the network model in OpenDSS is assumed to rotate at the system nominal frequency. Since the reference frames of the PV inverters and the network model are different, appropriate transformation needs to be done to inject the output current of the PV inverter model into the network model in OpenDSS. Figure 3.4 shows the transformation in the reference frames between the PV inverters and the network model in OpenDSS. The transformation based on the rotating angle difference between the two reference frames is given by

$$\begin{bmatrix} x_{d_j} \\ x_{q_j} \end{bmatrix} = \begin{bmatrix} \cos(\theta_j - \theta_i) & \sin(\theta_j - \theta_i) \\ -\sin(\theta_j - \theta_i) & \cos(\theta_j - \theta_i) \end{bmatrix} \begin{bmatrix} x_{d_i} \\ x_{q_i} \end{bmatrix} \tag{3.6}$$

where, x_{dj} and x_{qj} are the state variables under the *dq* frame of the outside circuit, x_{di} and x_{qi} are the state variables under the *dq* frame of the PV inverter. θ_j and θ_i are the rotating angle

of reference frame inside the PV inverter model and the OpenDSS network model respectively.

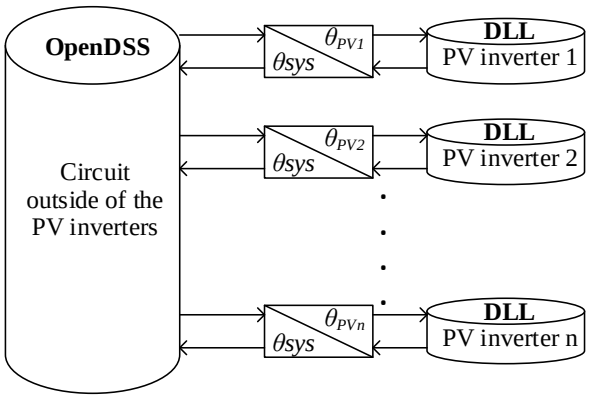

Figure 3.4 Reference frame changes between the PV inverters and the outside circuit

3.2.3 Implementation of the grid synchronization

The frequency of the network model in OpenDSS is assumed as constant (60 Hz). In steady state, the frequency of the PV inverter is the same as the frequency of the substation in the OpenDSS network model. In steady state, the reference frames of both the PV inverter and the OpenDSS network model are rotating at the same speed. During faults, for example, the frequency of the PV inverter deviates from the system frequency. The failure of the correct axis angle estimation will affect the current control loop in the controller, resulting in uncontrolled exchange of energy between the inverter and the grid. Therefore, the gird synchronization is required.

The grid synchronization is the estimation of the grid voltage angle at the PCC of each inverter. A PLL is typically used in grid-tied inverters to maintain a correct grid synchronization. The PLL is a closed-loop control system that automatically adjusts the output phase, so that the angle error between the output phase and the grid voltage at PCC is zero. The structure of a typical PLL is shown in Figure 3.5, where x_{in} and x_{out} are respectively

the input and rebuilt phases of the PLL. The PLL includes three main blocks: phase detector, loop filter and voltage controlled oscillator. The phase detector generates an error signal e_{phase} proportional to the difference between x_{in} and x_{out}. The loop filter is a low pass filter that attenuates the high frequency component in e_{phase}. The voltage controlled oscillator integrates the output from the loop filter, and generates the output phase x_{out}, which is fed back to complete the closed loop of the PLL.

In this work, the PLL is implemented for each PV inverter model. The reference frame of each PV inverter rotates at the frequency set by its own PLL.

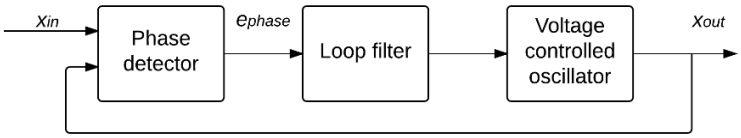

Figure 3.5 PLL algorithm

3.3 Analytical model of the PV inverter

In the following sections, the design and implementation of the filter, controller and PLL under the *dq* frame for each phase of the PV inverter are introduced. Based on the proposed single-phase *dq* frame transformation in Section 3.2, the state-space functions for each phase of the PV inverters are derived under the $\alpha\beta$ frame, and transformed to the ones under the *dq* frame.

3.3.1 State-space representation of the PV inverter filter

The α frame state-space equations of the PV filter shown in Figure 3.1 is given by

$$\begin{bmatrix} \dot{i}_{1\alpha} \\ \dot{i}_{2\alpha} \\ \dot{V}_{c\alpha} \end{bmatrix} = \begin{bmatrix} -\frac{R_1+R_3}{L_1} & \frac{R_3}{L_1} & \frac{1}{L_1} \\ \frac{R_3}{L_2} & -\frac{R_2+R_3}{L_2} & -\frac{1}{L_2} \\ -\frac{1}{C} & \frac{1}{C} & 0 \end{bmatrix} \begin{bmatrix} i_{1\alpha} \\ i_{2\alpha} \\ V_{c\alpha} \end{bmatrix} + \begin{bmatrix} -\frac{1}{L_1} & 0 \\ 0 & \frac{1}{L_2} \\ 0 & 0 \end{bmatrix} \begin{bmatrix} V_\alpha \\ E_\alpha \end{bmatrix} \tag{3.7}$$

where, $i_{1\alpha}$, $i_{2\alpha}$ and $V_{c\alpha}$ represent i_1, i_2 and V_c in the α frame respectively. V_α represents V_t in the α frame. By assuming a fictitious β axis, (3.7) can be re-written in the β frame as

$$\begin{bmatrix} \dot{i}_{1\beta} \\ \dot{i}_{2\beta} \\ \dot{V}_{c\beta} \end{bmatrix} = \begin{bmatrix} -\frac{R_1+R_3}{L_1} & \frac{R_3}{L_1} & \frac{1}{L_1} \\ \frac{R_3}{L_2} & -\frac{R_2+R_3}{L_2} & -\frac{1}{L_2} \\ -\frac{1}{C} & \frac{1}{C} & 0 \end{bmatrix} \begin{bmatrix} i_{1\beta} \\ i_{2\beta} \\ V_{c\beta} \end{bmatrix} + \begin{bmatrix} -\frac{1}{L_1} & 0 \\ 0 & \frac{1}{L_2} \\ 0 & 0 \end{bmatrix} \begin{bmatrix} V_\beta \\ E_\beta \end{bmatrix} \tag{3.8}$$

where, $i_{1\beta}$, $i_{2\beta}$ and $V_{c\beta}$ represent i_1, i_2 and V_c in the β frame respectively. V_β represents V_t in the β frame.

By applying the $\alpha\beta$ to dq transformation given by (3.4) to (3.7) and (3.8), the dq frame state-space equations are obtained. The state space equations in the dq frame are given by

$$\begin{bmatrix} \dot{i}_{1d} \\ \dot{i}_{1q} \\ \dot{i}_{2d} \\ \dot{i}_{2q} \\ \dot{V}_{cd} \\ \dot{V}_{cq} \end{bmatrix} = \begin{bmatrix} -\frac{R_1+R_3}{L_1} & \dot{\theta} & \frac{R_3}{L_1} & 0 & \frac{1}{L_1} & 0 \\ -\dot{\theta} & -\frac{R_1+R_3}{L_1} & 0 & \frac{R_3}{L_1} & 0 & \frac{1}{L_1} \\ \frac{R_3}{L_2} & 0 & -\frac{R_2+R_3}{L_2} & \dot{\theta} & -\frac{1}{L_2} & 0 \\ 0 & \frac{R_3}{L_2} & -\dot{\theta} & -\frac{R_2+R_3}{L_2} & 0 & -\frac{1}{L_2} \\ -\frac{1}{C} & 0 & \frac{1}{C} & 0 & 0 & \dot{\theta} \\ 0 & -\frac{1}{C} & 0 & \frac{1}{C} & -\dot{\theta} & 0 \end{bmatrix} \begin{bmatrix} i_{1d} \\ i_{1q} \\ i_{2d} \\ i_{2q} \\ V_{cd} \\ V_{cq} \end{bmatrix} + \begin{bmatrix} -\frac{1}{L_1} & 0 & 0 & 0 \\ 0 & -\frac{1}{L_1} & 0 & 0 \\ 0 & 0 & \frac{1}{L_2} & 0 \\ 0 & 0 & 0 & \frac{1}{L_2} \\ 0 & 0 & 0 & 0 \\ 0 & 0 & 0 & 0 \end{bmatrix} \begin{bmatrix} V_d \\ V_q \\ E_d \\ E_q \end{bmatrix} \tag{3.9}$$

where, $\dot{\theta}$ is the frequency inside the PV inverter. The appearance of $\dot{\theta}$ is due to the cross coupling during the $\alpha\beta$ to dq transformation. i_{1d}, i_{1q}, i_{2d}, i_{2q}, V_{cd}, V_{cq}, E_d and E_q are time-invariant values of i_1, i_2, V_c and E_c in the d frame and q frame respectively. V_{cd} and V_{cq}. V_d and V_q represent V_t in the d frame and the q frame respectively.

3.3.2 State-space representation of the PV inverter controller

Similarly, the state-space representation of the PV inverter controller shown in Figure 3.1 can also be derived using the single-phase dq transformation. The frequency domain transfer function $G_c(s)$ of the proportional resonant controller for the inverter current control loop is given by

$$G_c(s) = \frac{K_R s}{s^2 + 0.6s + (2\pi f)^2} + K_P \tag{3.10}$$

where, K_R and K_P are parameters in the controller.

The state-space representation of the controller under the $\alpha\beta$ frame can be derived as

$$\begin{bmatrix} \dot{x}_{1\alpha} \\ \dot{x}_{1\beta} \end{bmatrix} = -0.6 \begin{bmatrix} x_{1\alpha} \\ x_{1\beta} \end{bmatrix} - 277.6 \begin{bmatrix} x_{2\alpha} \\ x_{2\beta} \end{bmatrix} + \begin{bmatrix} I_d^* - i_d \\ I_q^* - i_q \end{bmatrix} \tag{3.11}$$

$$\begin{bmatrix} \dot{x}_{2\alpha} \\ \dot{x}_{2\beta} \end{bmatrix} = 512 \begin{bmatrix} x_{2\alpha} \\ x_{2\beta} \end{bmatrix} \tag{3.12}$$

$$\begin{bmatrix} y_\alpha \\ y_\beta \end{bmatrix} = \begin{bmatrix} K_R & 0 \\ K_R & 0 \end{bmatrix} \begin{bmatrix} x_{1\alpha} \\ x_{1\beta} \end{bmatrix} + \begin{bmatrix} K_P & 0 \\ K_P & 0 \end{bmatrix} \begin{bmatrix} I_d^* - i_d \\ I_q^* - i_q \end{bmatrix} \tag{3.13}$$

$$\begin{bmatrix} E_\alpha \\ E_\beta \end{bmatrix} = \begin{bmatrix} y_\alpha \\ y_\beta \end{bmatrix} + \begin{bmatrix} V_\alpha \\ V_\beta \end{bmatrix} \tag{3.14}$$

where. $x_{1\alpha}$ and $x_{2\alpha}$ are the values of the state variables x_1 and x_2 in the α frame, and $x_{1\beta}$ and $x_{2\beta}$ are the values of the state variables x_1 and x_2 in the β frame. E_α, E_β are respectively E_c in the α frame and β frame.

The $\alpha\beta$ to dq transformation given by (3.4) is applied to (3.11)-(3.14), and the controller outputs E_d and E_q are obtained from (3.14). After replacing the terms E_d and E_q in (3.9) by the state-space variables x_{1d}, x_{1q}, x_{2d} and x_{2q}, the state-space function for each phase of the circuit under the d frame and q frame is obtained as

$$\begin{bmatrix} \dot{i}_{1d} \\ \dot{i}_{1q} \\ \dot{i}_{2d} \\ \dot{i}_{2q} \\ \dot{V}_{cd} \\ \dot{V}_{cq} \\ \dot{x}_{1d} \\ \dot{x}_{1q} \\ \dot{x}_{2d} \\ \dot{x}_{2q} \end{bmatrix} = \begin{bmatrix} -\frac{R_1+R_3}{L_1} & \dot{\theta} & \frac{R_3}{L_1} & 0 & \frac{1}{L_1} & 0 & 0 & 0 & 0 & 0 \\ -\dot{\theta} & -\frac{R_1+R_3}{L_1} & 0 & \frac{R_3}{L_1} & 0 & \frac{1}{L_1} & 0 & 0 & 0 & 0 \\ \frac{R_3-K_P}{L_2} & 0 & -\frac{R_2+R_3}{L_2} & \dot{\theta} & -\frac{1}{L_2} & 0 & \frac{K_R}{L_2} & 0 & 0 & 0 \\ 0 & \frac{R_3-K_P}{L_2} & -\dot{\theta} & -\frac{R_2+R_3}{L_2} & 0 & -\frac{1}{L_2} & 0 & \frac{K_R}{L_2} & 0 & 0 \\ -\frac{1}{C} & 0 & \frac{1}{C} & 0 & 0 & \dot{\theta} & 0 & 0 & 0 & 0 \\ 0 & -\frac{1}{C} & 0 & \frac{1}{C} & -\dot{\theta} & 0 & 0 & 0 & 0 & 0 \\ -1 & 0 & 0 & 0 & 0 & 0 & -0.6 & \dot{\theta} & -277.6 & 0 \\ 0 & -1 & 0 & 0 & 0 & 0 & -\dot{\theta} & -0.6 & 0 & -277.6 \\ 0 & 0 & 0 & 0 & 0 & 0 & 512 & 0 & 0 & \dot{\theta} \\ 0 & 0 & 0 & 0 & 0 & 0 & 0 & 512 & -\dot{\theta} & 0 \end{bmatrix} \begin{bmatrix} i_{1d} \\ i_{1q} \\ i_{2d} \\ i_{2q} \\ V_{cd} \\ V_{cq} \\ x_{1d} \\ x_{1q} \\ x_{2d} \\ x_{2q} \end{bmatrix} + \begin{bmatrix} -\frac{1}{L_1} & 0 & 0 & 0 \\ 0 & -\frac{1}{L_1} & 0 & 0 \\ \frac{1}{L_2} & 0 & \frac{K_P}{L_2} & 0 \\ 0 & \frac{1}{L_2} & 0 & \frac{K_P}{L_2} \\ 0 & 0 & 0 & 0 \\ 0 & 0 & 0 & 0 \\ 0 & 0 & 1 & 0 \\ 0 & 0 & 0 & 1 \\ 0 & 0 & 0 & 0 \\ 0 & 0 & 0 & 0 \end{bmatrix} \begin{bmatrix} V_d \\ V_q \\ I_d^* \\ I_q^* \end{bmatrix} \quad (3.15)$$

where, x_{1d}, x_{1d}, x_{2d}, x_{2q} are time-invariant values of x_1, x_2 under the d frame and q frame respectively. $\dot{x}_{1d}$, $\dot{x}_{1q}$, $\dot{x}_{2d}$ and $\dot{x}_{2q}$ represent respectively the first-order time differential of x_{1d}, x_{1q}, x_{2d}, x_{2q}.

3.3.3 State-space function of PLL

In this work, the PLL is implemented in the *abc* frame. The state-space representation of the PLL is given by

$$\begin{bmatrix} \dot{x}_3 \\ \dot{x}_4 \end{bmatrix} = -46.9 \begin{bmatrix} x_3 \\ x_4 \end{bmatrix} + \begin{bmatrix} 2 \\ 0 \end{bmatrix} u_{PLL} \quad (3.16)$$

$$u_{PLL} = \begin{bmatrix} -\sin(\theta) & -\sin(\theta - \frac{2\pi}{3}) & -\sin(\theta + \frac{2\pi}{3}) \end{bmatrix} \begin{bmatrix} X_a \\ X_b \\ X_c \end{bmatrix} \tag{3.17}$$

$$y_{PLL} = \dot{\theta} = \begin{bmatrix} 2.357 & 7.938 \end{bmatrix} \begin{bmatrix} x_3 \\ x_4 \end{bmatrix} + 2\pi 60 \tag{3.18}$$

where, x_3 and x_4 are the state variables in the PLL. u_{PLL} represents the input of PLL, which is the PV inverter terminal voltage at the PCC along the q axis. X_a, X_b and X_c represent respectively the electrical quantities $|V_a|cos(\omega t)$, $|V_b|cos(\omega t)$ and $|V_c|cos(\omega t)$, where $|V_a|$, $|V_b|$ and $|V_c|$ are peak values of the sinusoidal voltage waveform V_t of Phase A, B and C respectively, ω is the nominal frequency. The output y_{PLL} of the PLL is the angle of the PV inverter reference frame at each time step, denoted as θ.

The output θ of the PLL is used to exchange the electrical quantities between the PV inverter model and the OpenDSS network model. The rotating angle of the reference frame of the OpenDSS circuit can be calculated based on the assumed constant nominal frequency (60 Hz). The interfacing of the DLL containing the PV inverter model and the network model in OpenDSS is explained in the following section.

3.4 Interface between the PV inverter DLL and the OpenDSS circuit

The state-space model of the PV inverter components is programmed in the DLL using the Object Pascal (Delphi) programming language [108]. During the dynamic simulation, the dynamic models of PV in the DLL interact with the network model in OpenDSS. Figure 3.6 describes the process to exchange data between the DLL containing the PV inverter model and the rest of the network model in OpenDSS.

The dynamic simulation includes the three main steps:

1. Initialization: Before executing the dynamic study, a snapshot power flow simulation is performed in OpenDSS for the circuit without the PV inverter. The initial voltage at the PV inverter PCC is calculated and transferred to the PV inverter model stored in the DLL. The algebraic equations of the state variables are then solved, and the initial values of the state variables are stored for the dynamic study.
2. Integration: The state-space equations (3.15)-(3.18) are solved to obtain the time differential of all the state variables. Based on the time derivatives of the state variables, the state variables are updated using the improved Euler-Cauchy method [109].
3. Export and update: The calculated current values from the integration procedure are injected into the network model in OpenDSS. At the same time, the voltage values at the PCC of the PV inverter are also imported from the network model in OpenDSS to the PV inverter model. The voltage values are computed based on the current injected by the PV inverter model into the network model in OpenDSS, in the previous time step. The reference frame transformation illustrated in Section 3.2 needs to be applied during the exchange of the voltage and current values between the network model and the inverter model.

The process is continued until the dynamic simulation reaches the final time step, as illustrated in Figure 3.6.

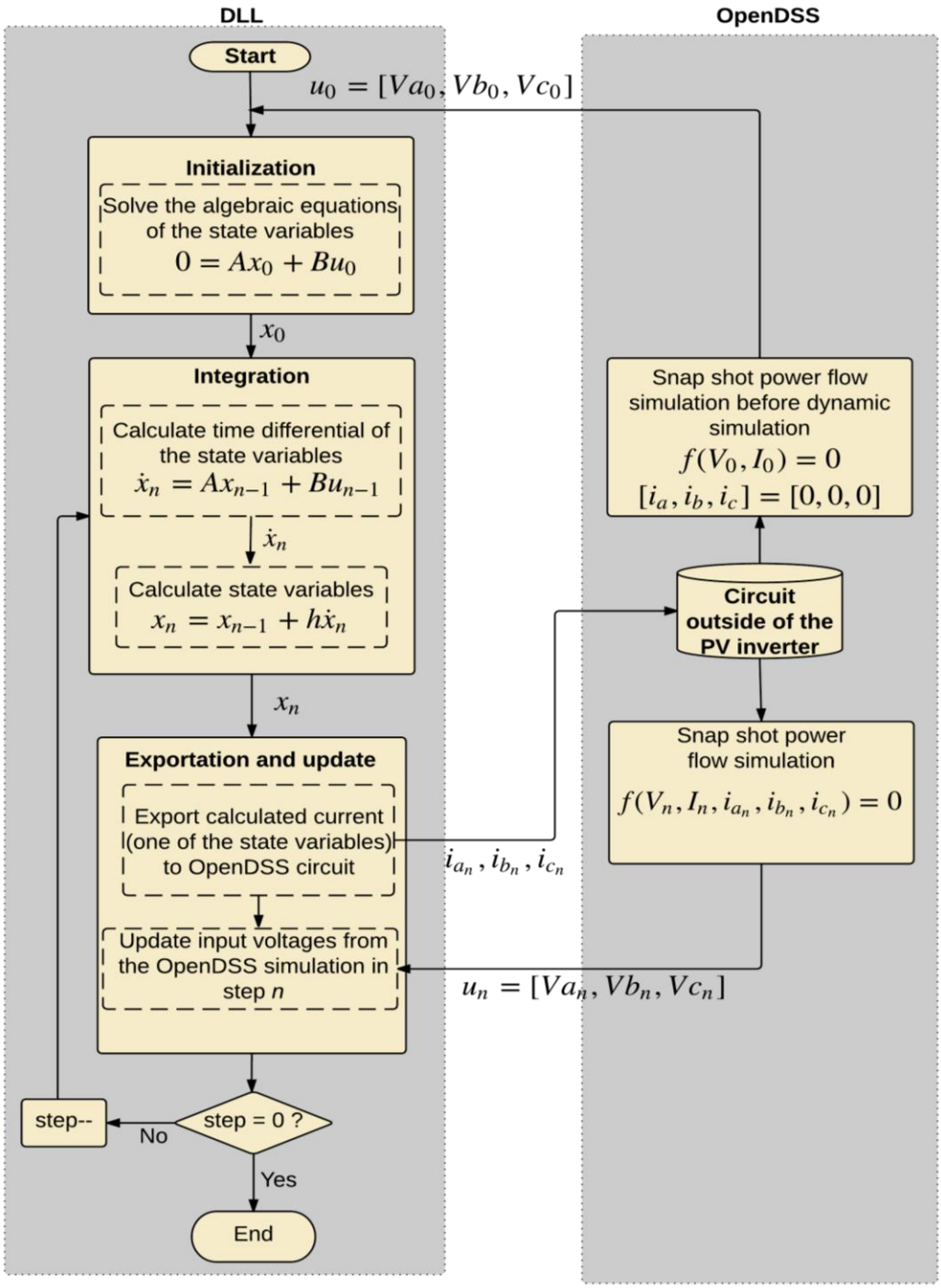

Figure 3.6 Algorithm of the interaction between PV inverter DLL and OpenDSS circuit

3.5 Validation of the PV inverter DLL

To verify the accuracy of the unbalanced PV inverter DLL, a three-bus system, as shown in Figure 3.8, is built and simulated in both OpenDSS and PLECS. Both balanced and unbalanced cases are considered and applied to the PV inverters. In addition, a balanced PV inverter is built in a separate DLL to illustrate the advantage of the single-phase frame based PV inverter model.

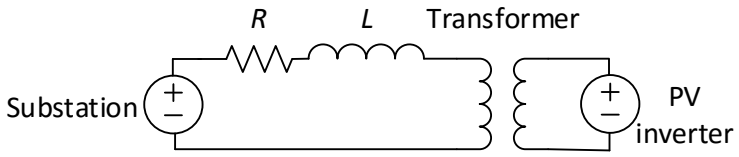

Figure 3.7 Three-bus system used for verification of the PV inverter DLL

In PLECS, which is an EMTP-type solver, all network elements as well as the PV inverters are represented by differential equations. On the other hand, in OpenDSS, only the PV inverters are represented by differential equations, and the network model is represented by algebraic equation.

3.5.1 Balanced case verification

Two balanced system disturbances were analyzed. The cases include:

1. The change of the reference values in the PV inverter
2. The system response to a three-phase fault.

Case 1: Reference changes in the PV inverter

At 0.05 s, a change of the solar irradiation from 1 p.u. to 0.5 p.u. is applied to the PV inverter of 300 kW rating. The simulated PV inverter current outputs are shown in Figure 3.8. PLECS provides the instantaneous values of the output current of the PV inverters,

and OpenDSS monitors the output current phasors from the PV inverters in both the balanced and unbalanced PV inverter models. As seen from Figure 3.8, the current values from the positive-sequence PV inverter model overlap the ones from the inverter model proposed in this work. The peak current values from the both models closely match the results from PLECS in the balanced case.

In OpenDSS, values of the electrical quantities are analyzed as phasors. Within the DLL containing the PV inverter model, the instantaneous current can be calculated from the state variables i_{1d}, i_{1q}, based on the *dq* to *abc* transformation given by (3.2). The PLL output θ indicates the angle of the PV reference frame and is used in (3.2) for the transformation. Figure 3.9 shows the calculated instantaneous current from the unbalanced PV inverter model, as well as the simulated current phasors from OpenDSS. The ability to obtain the instantaneous value of the current from the PV inverter model extends the capability of OpenDSS to perform dynamic analysis. The results of the proposed method were compared to the results obtained by a detailed simulation performed in PLECs. The instantaneous current values obtained by the proposed method were found to match the detailed simulation output closely.

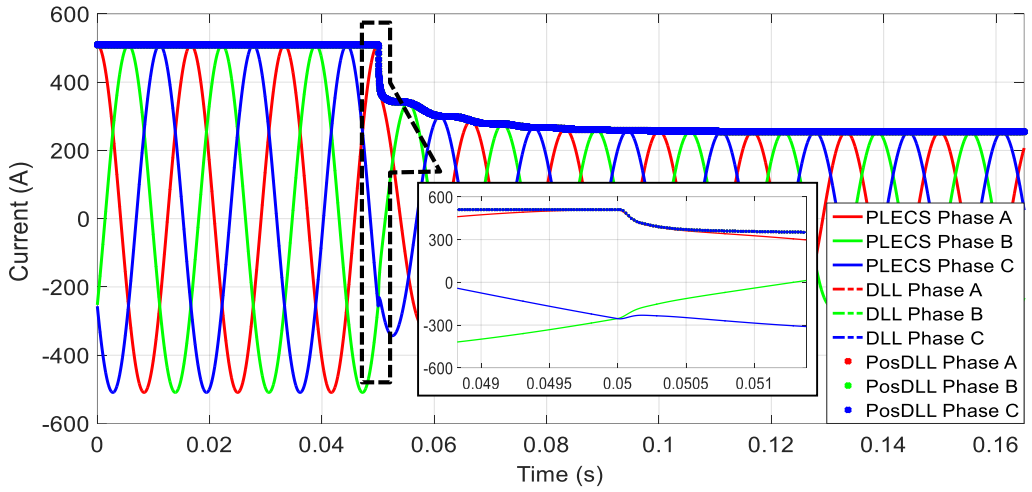

Figure 3.8 PV inverter output current (instantaneous and peak values) corresponding to reference changes from the PV inverter in PLECS, DLL, and positive sequence DLL

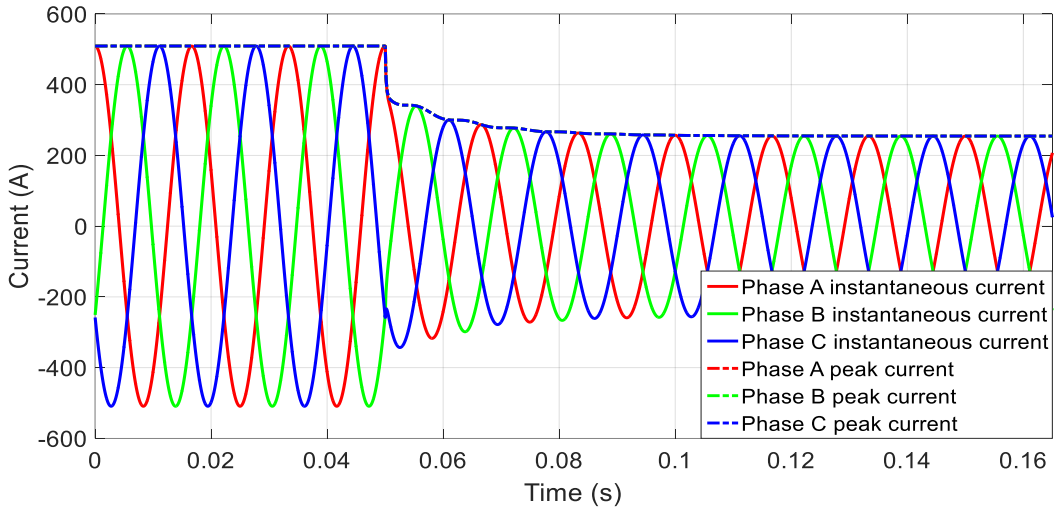

Figure 3.9 Simulated PV inverter output current (instantaneous and peak values) during reference changes in OpenDSS

Case 2: Three-phase fault in the system

At 0.05 s, a three-phase fault with a fault resistance of 0.05 Ω is applied on the transformer primary side shown in Figure 3.7. The outputcurrent using a balanced and an unbalance inverter in OpenDSS and PLECS are plotted in Figure 3.10. During the balanced faults, the fault current contributions from both the balanced and the unbalanced PV inverter models are same. As shown in Figure 3.10, the output current phasors from the two inverter models are overlapping. These results match the output obtained from the detailed simulations performed in PLECS. Figure 3.11 shows the PV terminal voltage at PCC from the simulation results in OpenDSS and PLECS. The terminal voltages closely match the three simulation results.

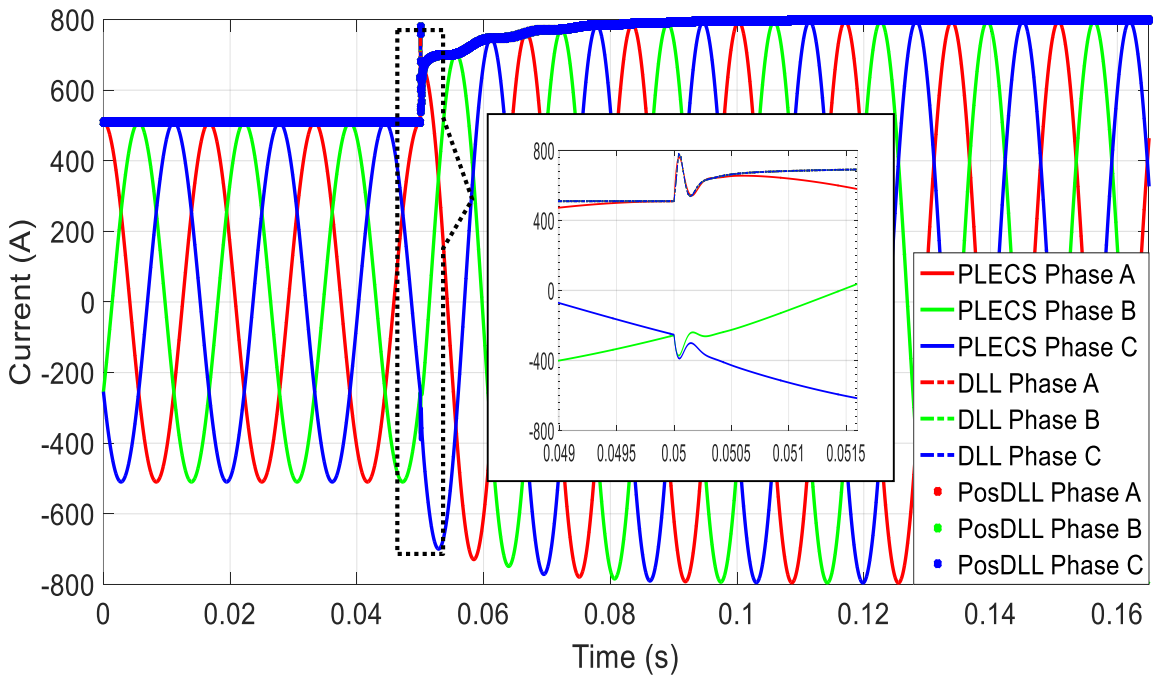

Figure 3.10 Output current (instantaneous and peak values) during three-phase fault in PLECS, DLL, and positive sequence DLL

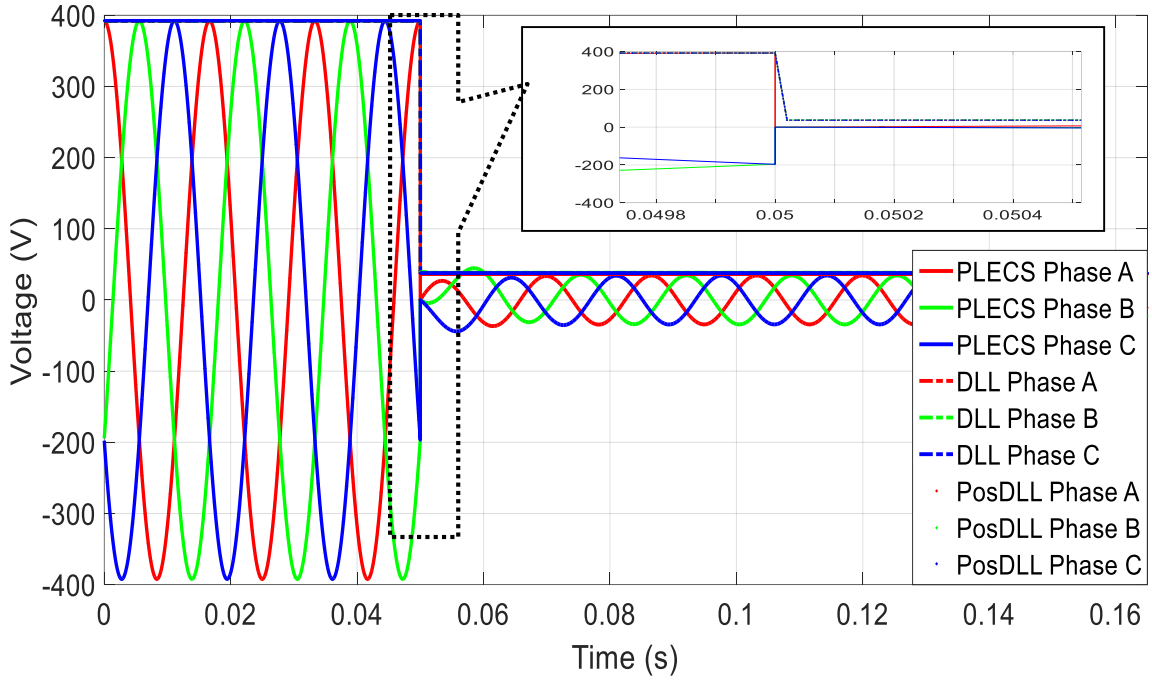

Figure 3.11 PV terminal voltage (instantaneous and peak values) during three-phase fault in PLECS, DLL, and positive sequence DLL

3.5.2 Unbalanced case verification

Due to the adoption of the single-phase *dq* frame method, the PV inverter can also be used for studying unbalanced conditions. A single phase to ground fault is applied to phase A on the primary side of the transformer at 0.05 s. A model of a positive-sequence PV inverter is also simulated to compare the results of the study. For a better illustration of the results, the instantaneous current obtained by the proposed method as well as those obtained from the detailed simulation in PLECS are plotted in Figure 3.12. As shown in Figure 3.12, the PV output current obtained by using the unbalanced PV inverter model closely matches with those obtained via detailed simulation in PLECS. However, the output current waveforms are markedly different from the PLECS output when the balanced

inverter model is used in OpenDSS. Figure 3.12 shows the advantage of the unbalance modeling of the PV inverters in this work.

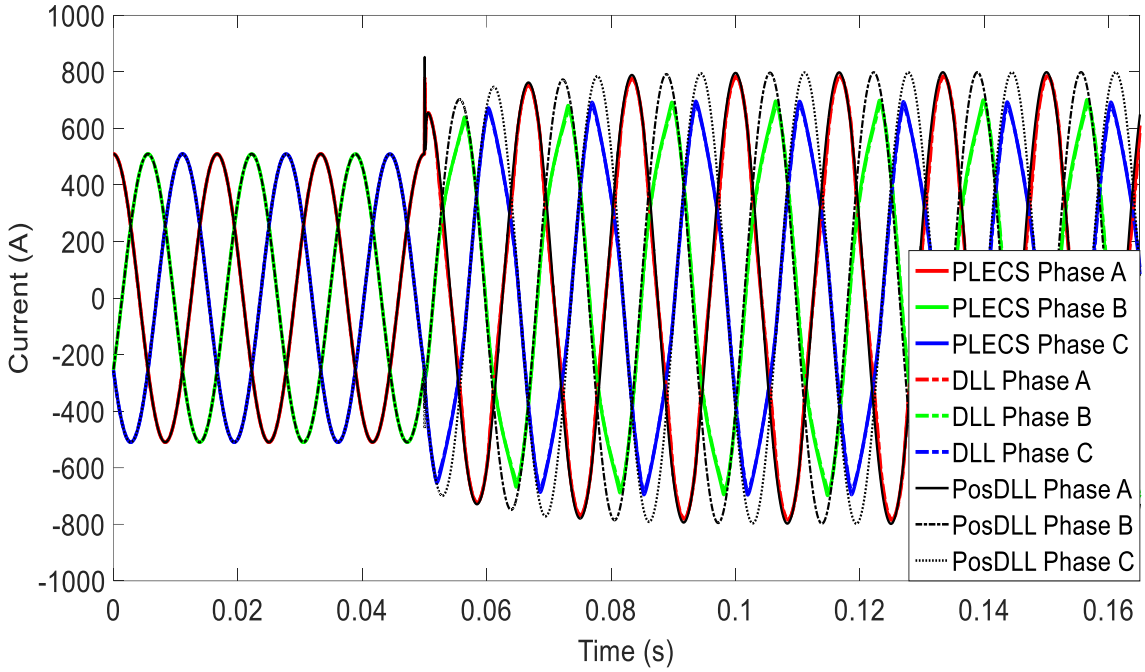

Figure 3.12 Simulated PV inverter output current during Phase A fault in PLECS, DLL, and positive sequence DLL

3.6 DAE based dynamic analysis of the three-phase and single-phase PV inverters in large power systems

In order to show that the proposed modeling method can be applied to large-scale systems, simulations are conducted on the IEEE 8500-node distribution test feeder in OpenDSS [110]. Due to the complexity of building and simulating such large-scale system in PLECS, the simulated results are not validated against the results from PLECS.

A three-phase 700 kW PV inverter is built and the model is stored in a DLL. This inverter model can capture the effect of unbalanced voltages and currents in the system. Three PV inverters, PV 1, PV 2, and PV 3 are installed along the feeder, at bus M1142843,

bus M1069517 and bus M1047522 respectively. The fault current contribution from the inverter is limited to 1.5 times of the rated current capacity of the respective inverter. Traditionally, the fault current contribution from the PV inverters is obtained by applying a fault at the PV inverter terminal, and measuring the output current either through hardware testing or by simulation using EMTP solvers. The fault current contribution from PV systems is highly dependent on the location of the fault and the PV inverter terminal voltage. The traditional testing results do not reflect the variation in the fault current contribution for different cases due to the limitations of building large-scale systems with dynamic model of PV inverters.

Two separate cases of three-phase fault are studied. The faults are applied at two different locations in the feeder. Fault 1 is applied at bus L2973162, which is located in the middle of the feeder downstream of PV 3 at 0.05 s. The simulated output current of the three PV units are plotted in Figure 3.13. As seen from Figure 3.13, the PV output current contains an oscillation of double frequency before the fault is applied. The oscillation in current is due to the voltage unbalance in the 8500-bus feeder and the PLL design. As describes in Section 3.3, the PLL is implemented based on assumption that the three-phase PV inverter terminal voltage is balanced. The voltage unbalance in the feeder produces double-frequency oscillations in the PLL output, and thus affects the output of the PV system. The double frequency oscillations can be eliminated by other designs of the PLL, such as the double synchronous frame PLL (DSF-PLL) [111], [112]. Since this work aims to illustrate the applicability of DAE based PV inverter for large distribution systems, the improved design of the PLL is not pursued here.

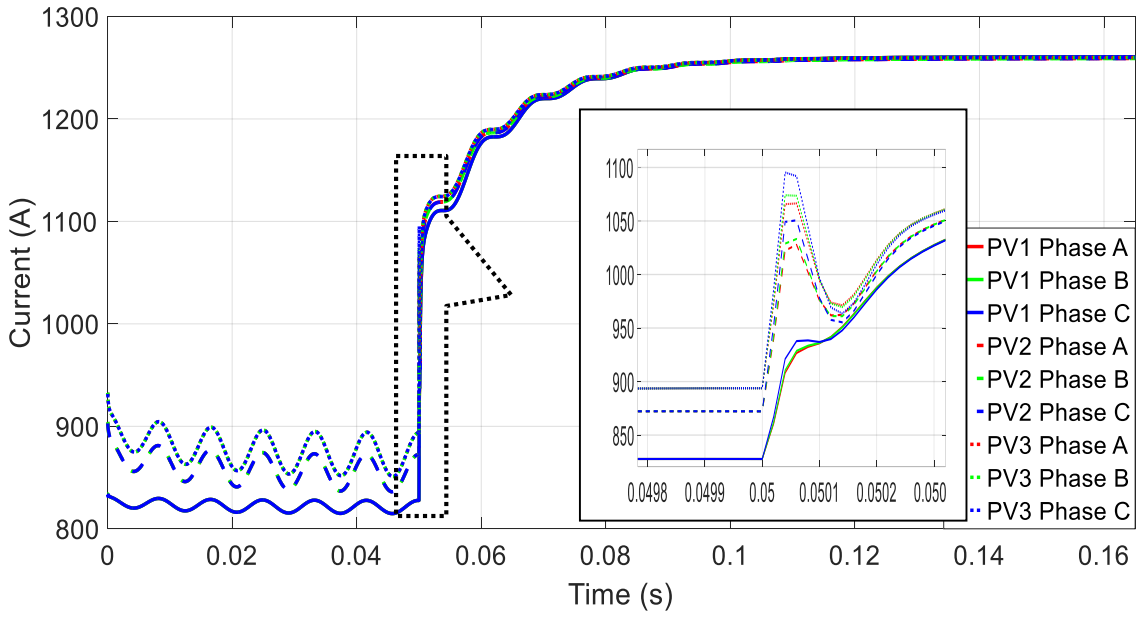

Figure 3.13 Simulated PV inverter output currents during Fault 1 in OpenDSS

As shown in Figure 3.13, the output current of the three PV systems increase to the maximum limit after the fault is applied. Since the fault is applied at the middle of the feeder, the large drop of the terminal voltages of the PV units result in the output current to reach the maximum limit. Since Fault 1 isolates the part of the feeder with significant unbalance, less double-frequency oscillation are observed after the fault is cleared, as seen from Figure 3.13.

The fault current measured at the substation is plotted in Figure 3.14, with and without the three-phase PV units connected to the system. The fault current contributions from the PV units reduce the current seen by the protective device near the substation, thereby reducing its sensitivity. The ratings of the protective devices need to be redesigned based on the fault current contribution of the PV units.

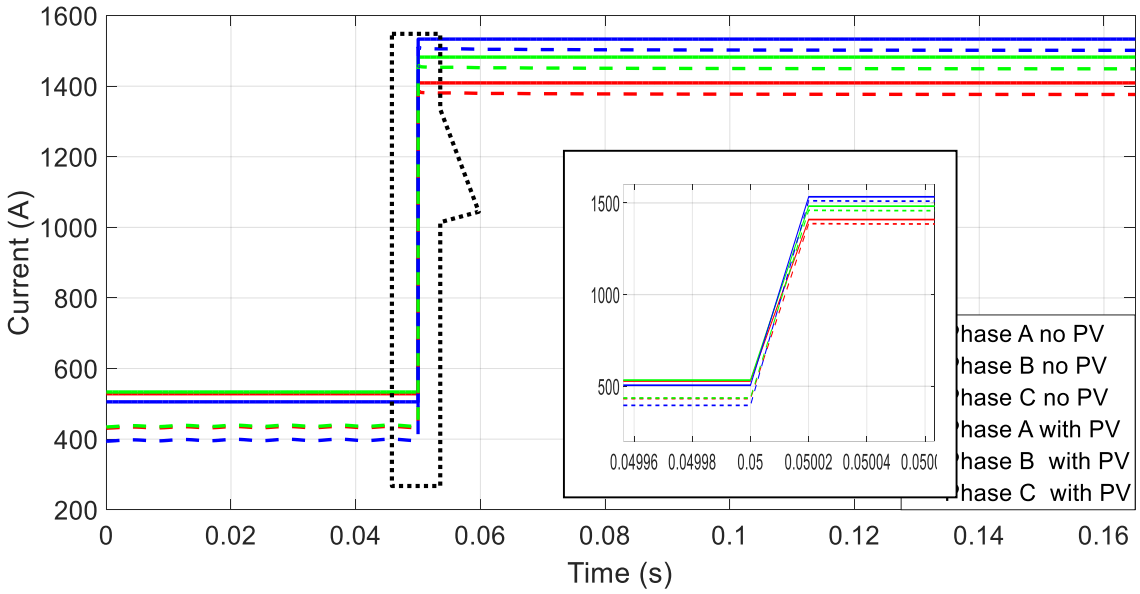

Figure 3.14 Simulated current through substation during Fault 1 in OpenDSS

Another three-phase fault, Fault 2 is applied at bus L3066815 at 0.05 s. The simulated output current of the three PV units are plotted in Figure 3.15. Since Fault 2 is at the feeder end, less voltage drop occurs at the terminals of the three PV units as compared to during Fault 1. The fault current contributions from the three PV units differ from each other due to different terminal voltages. The double-frequency oscillation exists before and after the fault, as the unbalanced portion of the system is not disconnected when the fault is cleared. The fault current measured at the substation is plotted in Figure 3.16, with and without the three-phase PV units connected to the system. The current measured at the substation for Fault 2 differs significantly from the measurement made during Fault 1. The results indicate that the change in the fault location has a significant impact on the fault current contribution by the PV units. Such studies can help planners design distribution systems with proper protective device settings, considering different fault scenarios with dynamic PV unit models, based on manufacturer data.

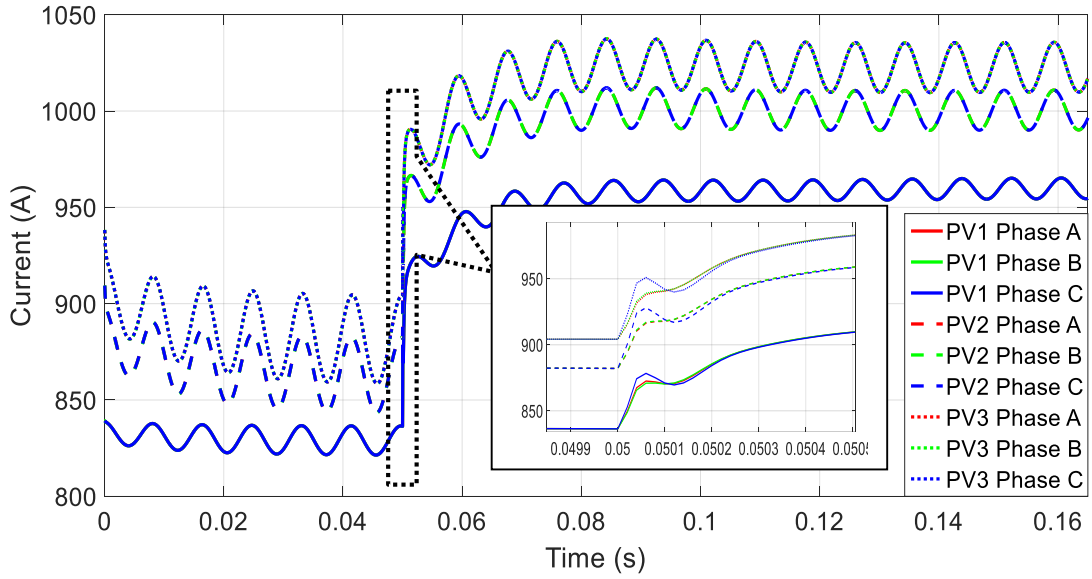

Figure 3.15 Simulated PV inverter output current during Fault 2 in OpenDSS

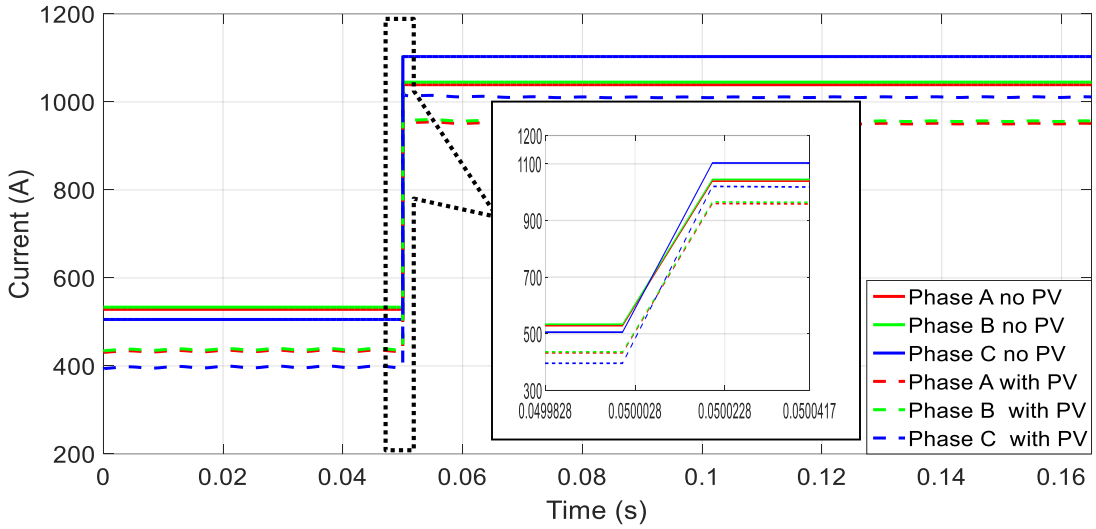

Figure 3.16 Simulated current through substation during Fault 2 in OpenDSS

3.7 DAE based dynamic analysis of the anti-islanding scheme of PV inverters

According to IEEE standard 1547, the islanding of the PV inverters occurs when a portion of an electric power system containing PV inverters is disconnected from the main

system, while the independent PV inverters continue energizing the isolated system. Failure of islanding detection can lead to several negative impacts, including danger to maintenance personnel, poor power quality and damages to the utility equipment.

The anti-islanding techniques have been proposed and tested through electromagnetic transient simulations and hardware implementations [113-114]. However, the anti-islanding schemes have not been tested for large systems due to the limitations of the EMTP-type solvers and hardware testing. The proposed DAE based dynamic modeling and analysis method of the PV inverters can assist in the design of anti-islanding control for PV inverters.

In this section, the capability of the proposed method to model and test the anti-islanding controls in large distribution systems is demonstrated. The basic passive anti-islanding scheme based on over/under voltage detection is adopted in the proposed DAE based method. Other anti-islanding schemes including passive and active schemes can be implemented in the DAE based dynamic models in a similar manner.

3.7.1 Design of the anti-islanding scheme

The design of the anti-islanding control of the PV inverter based on the worst-case scenario [114] is shown in Figure 3.17. In Figure 3.17, the load is modeled as a *RLC* load with a high quality factor. The quality factor q [114] is given by

$$q = R_{Load}\sqrt{\frac{C_{Load}}{L_{Load}}} \tag{3.19}$$

where, R_{Load}, L_{Load} and C_{Load} represent respectively the resistance, inductance and capacitance component of the load in Figure 3.17.

The *RLC* load is used as the worst-case scenario, since *RLC* loads with a high q are the most problematic for islanding detection.

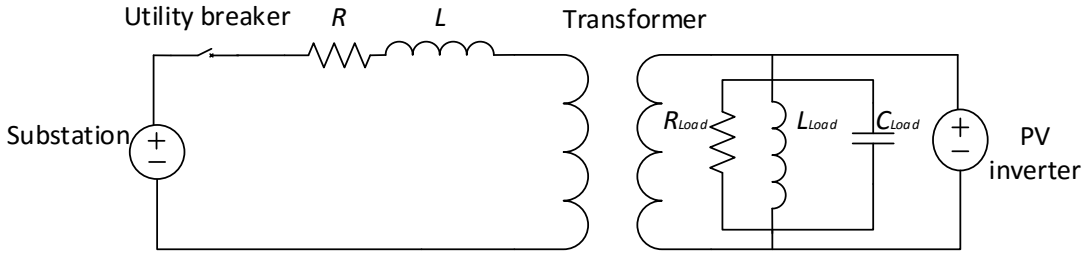

Figure 3.17 Worst-case scenario with *RLC* load

In Figure 3.17, the real power of the *RLC* load is given by

$$P_{Load} = \frac{V_{Load}^2}{R_{Load}} \tag{3.20}$$

where, V_{Load} is the voltage at the *RLC* load in Figure 3.17.

Based on (3.20), a positive voltage feedback mechanism is established, as shown in Figure 3.18. From Figure 3.18, it can be seen that when the PV inverter senses an increase in the voltage at the PCC, the anti-islanding control increases the PV inverter active power output. The current controller in the PV inverter follows the command, and increases the PV inverter active power output P_{output}. Due to the load characteristics given by (3.20), the voltage at the *RLC* load increases to balance the active power. The increase in voltage further increases the inverter active power output because of the positive feedback. By this mechanism, the voltage at PCC will keeps increasing until the islanding is detected. The scheme works in a similar way if there is an initial dip in the PCC voltage due to the islanding. The voltage is driven below the lower voltage threshold if an intial dip in the PCC voltage is recoded.

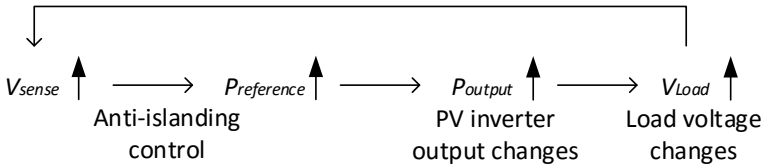

Figure 3.18 Positive voltage feedback in the anti-islanding scheme

Figure 3.19 shows the average model of the PV inverter with the anti-islanding scheme. The anti-islanding control comprises of three main parts, a band-pass filter (BPF), a gain and a limiter. The BPF is used to avoid noise injection and dc offset. The gain is designed to be small enough to keep a stable system during the grid-connected mode, and large enough to make the system unstable during an islanded condition. The limiter specifies the maximum value of the signal Δi in the anti-islanding controller. V_d is the input of the anti-islanding controller, and the output of the controller Δi will be added to i_{ref}.

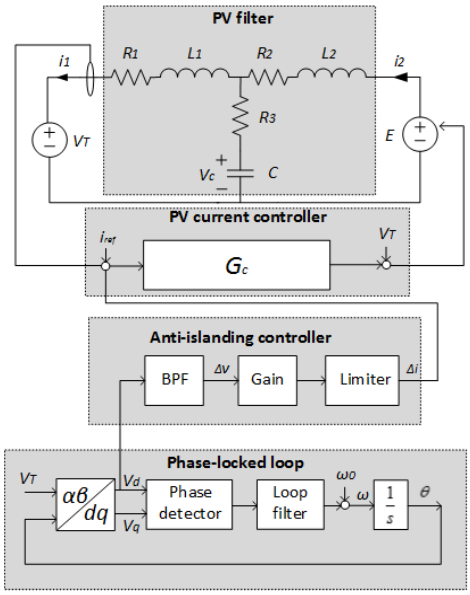

Figure 3.19 Average model of the PV inverter with anti-islanding scheme added

3.7.2 Implementation of the anti-islanding scheme in small system

The PV inverter shown in Figure 3.19 is implemented in a DLL, and connected to the system shown in Figure 3.17 in OpenDSS. In the OpenDSS network model, the power

consumed by the *RLC* load is set equal to the output of the PV inverter, so that the worst-case scenario can be studied. To illustrate the benefits of the anti-islanding scheme, the DAE based simulations are run without and with the anti-islanding controller enabled.

Anti-islanding scheme disabled

For this case, the simulations are run after disabling the anti-islanding controls on the inverter. At 0.05 s, the circuit breaker shown in Figure 3.17 is opened. The output current of the PV inverter and the voltage at PCC is monitored before and after the opening of the breaker. Figure 3.20 shows the instantaneous and peak current output monitored from the PV inverter DLL. Figure 3.21 shows the voltage at the PCC and the lower and upper voltage thresholds set for island detection. The upper threshold of the voltage at PCC is set as 1.1 times the base voltage, and the lower threshold is set to 0.88 times the base voltage [114]. The PV inverter is disconnected if the measured voltage violates the upper or the lower threshold.

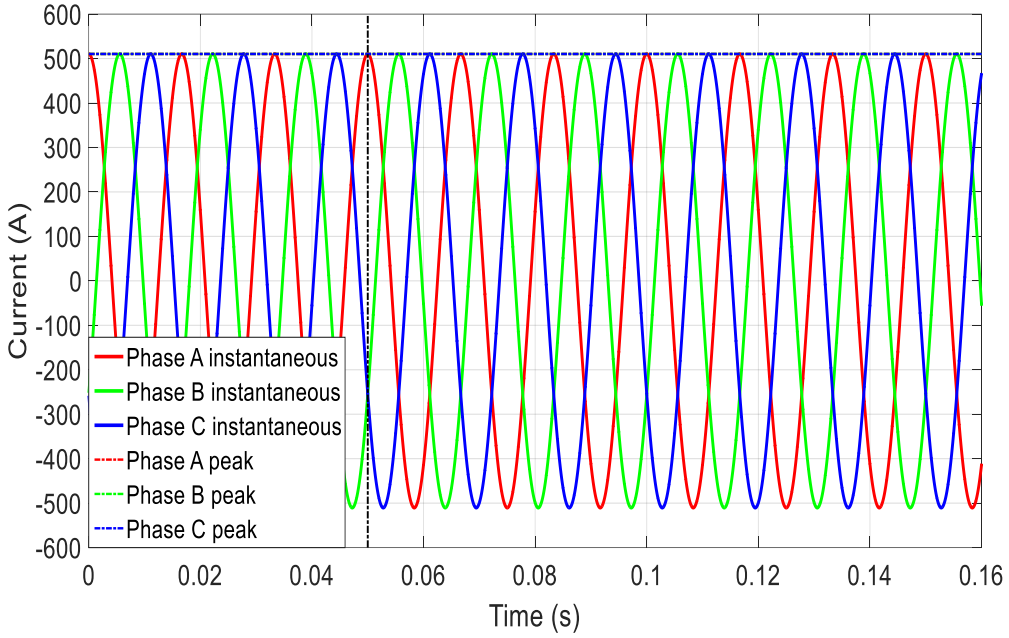

Figure 3.20 PV current output before and after the breaker opens (anti-islanding scheme disabled)

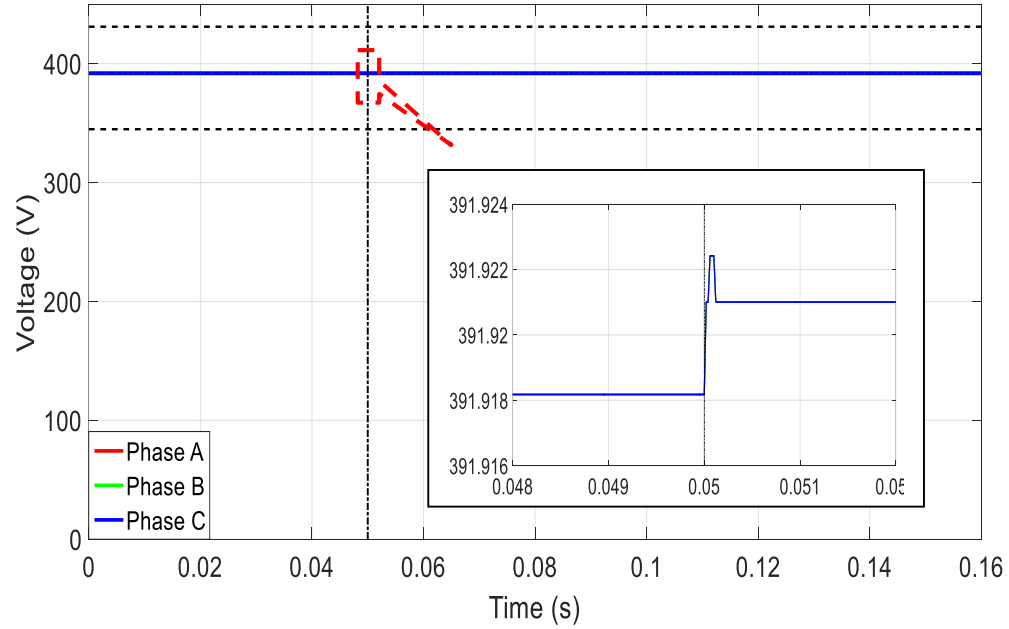

Figure 3.21 Voltage at PCC before and after the breaker opens (anti-islanding scheme disabled)

As shown in Figure 3.20 and Figure 3.21, the PV inverter cannot detect the islanding if the anti-islanding controller is disabled. From Figure 3.21, it can be seen that there is a small increase in the voltage at PCC after the breaker is opened. The opening of the breaker does not have any significant effect on the voltage at the PCC as the power consumed by the *RLC* load is equal to the inverter power supply. The PV inverter will continue supplying power to the load in the islanded condition.

Anti-islanding scheme enabled

For this case, the simulations are conducted with the anti-islanding controls enabled in the PV inverters. At 0.05 s, the circuit breaker shown in Figure 3.17 is opened. The output current of the PV inverter and the voltage at the PCC is monitored before and after the breaker is opened. Figure 3.22 shows the instantaneous and peak current output monitored at the PV inverter terminals. Figure 3.23 shows the voltage at the PCC and the upper and lower voltage thresholds for island detection.

As shown in Figure 3.22 and Figure 3.23, the PV inverter detects the islanding condition when the anti-islanding control is enabled. After the breaker opens, the initial increase of the voltage is applied at the positive feedback loop of the anti-islanding controller causing voltage at PCC to increase gradually. When the voltage exceeds the upper voltage threshold (at 0.11394 s), the inverter is disconnected from the grid.

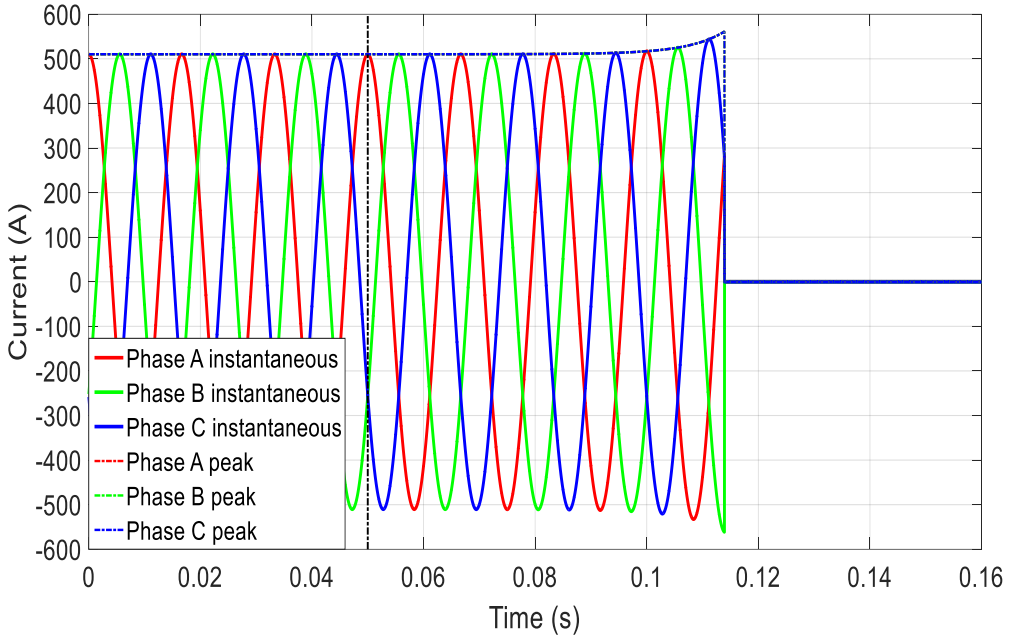

Figure 3.22 PV current output before and after the breaker opens (anti-islanding scheme enabled)

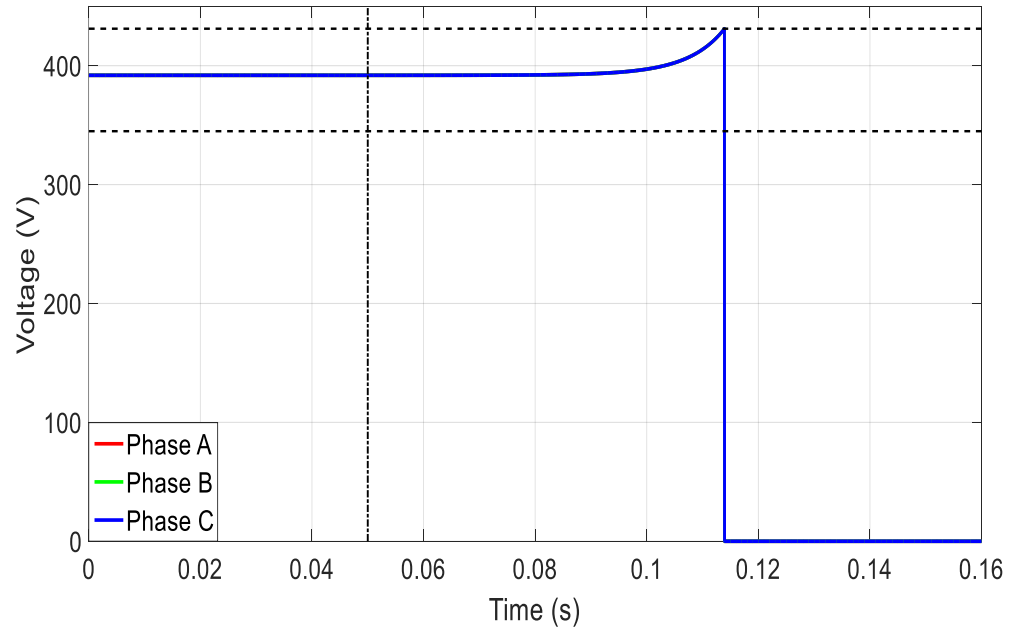

Figure 3.23 Voltage at PCC before and after the breaker opens (anti-islanding scheme enabled)

3.7.3 Study of the anti-islanding scheme in large systems

The implementation of the DAE based dynamic analysis can be used for testing of the anti-islanding controls for inverters connected to realistic large systems. The IEEE 123-node distribution test feeder in OpenDSS [110] is used for studying the anti-islanding controls of the connected PV inverters.

To study the worst-case scenario, the loads in the 123-node feeder are converted to constant impedance loads. In addition, to balance the total power consumed by the loads, single-phase and three-phase PV system is installed near each single-phase or three-phase load. The real and reactive power of each load is set equal to the power supplied by the PV system installed nearby. 91 PV systems are installed in the feeder. The total power supplied by the substation is nearly zero at the steady state. To illustrate the benefits of the anti-islanding controls, the simulations are run without and with the anti-islanding controller enabled.

Anti-islanding scheme disabled

The simulations are run after disabling the anti-islanding controls on the inverter. At 0.08 s, the circuit breaker near the substation is opened. The output current of the PV systems (91 PV units) and the voltages at PCC are monitored before and after the opening of the breaker. Figure 3.24 shows that the current outputs from all the PV systems remain almost the same after the breaker opens. Figure 3.25 shows that little voltage drops happen at PCC when breaker opens.

From Figure 3.24 and Figure 3.25 it can be seen that the PV inverter cannot detect islanding if the anti-islanding scheme is disabled. The PV inverters continue to supply the loads in an islanded condition.

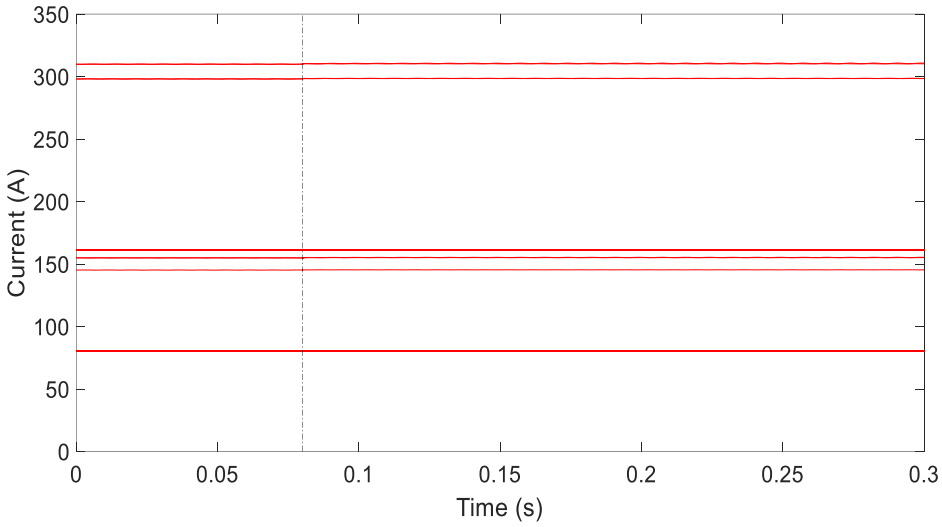

Figure 3.24 All PV (91 PVs) current outputs before and after the breaker opens (anti-islanding scheme disabled)

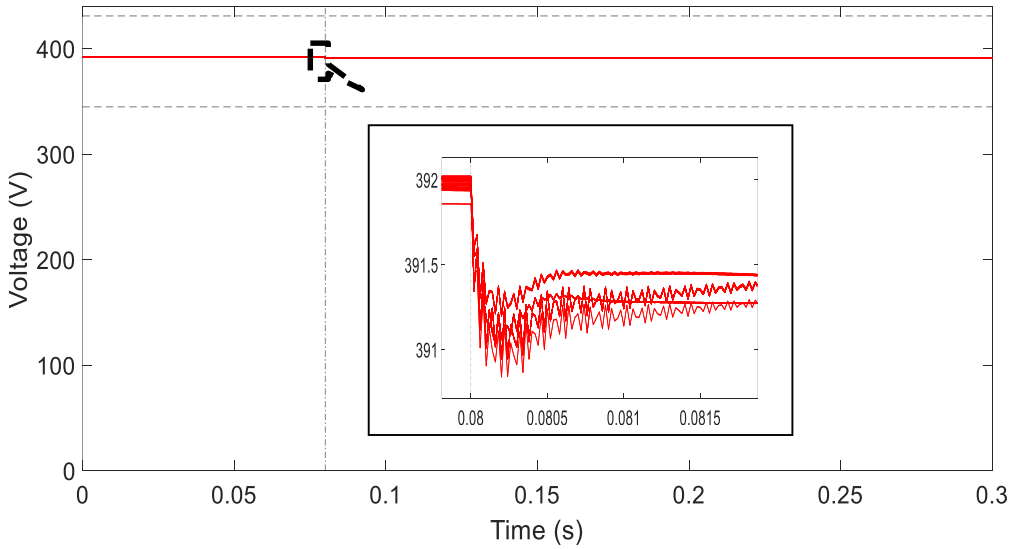

Figure 3.25 All PV (91 PVs) voltages at PCC before and after the breaker opens (anti-islanding scheme disabled)

Anti-islanding scheme enabled

The simulations are run after enabling the anti-islanding controls in the PV inverters. At 0.08 s, the circuit breaker near the substation is opened. The output current and the voltages at the PCC of the PV systems are monitored.

As shown in Figure 3.26 and Figure 3.27, the anti-islanding controls detect the disconnection of the grid. After the circuit breaker opens, the initial dip in the voltage at PCC initializes the positive feedback control of the anti-islanding scheme. At 0.08716 s, the voltage dips below the lower voltage threshold causing the inverter to disconnect from the system. As shown in Figure 3.26, the output currents from all the PV systems become zero after 0.08716 s.

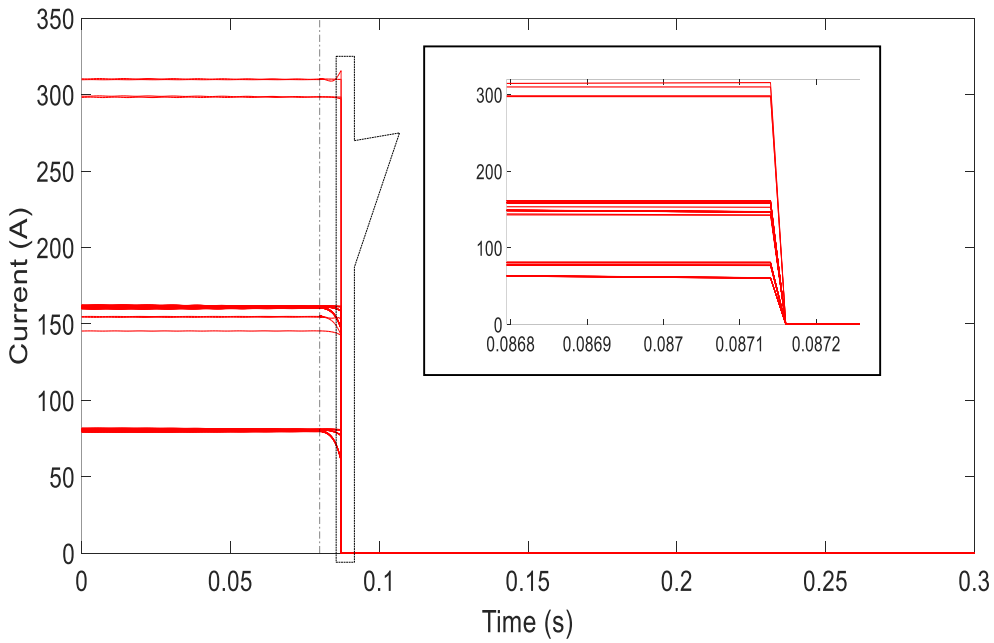

Figure 3.26 All PV (91 PVs) current outputs before and after the breaker opens (anti-islanding scheme enabled)

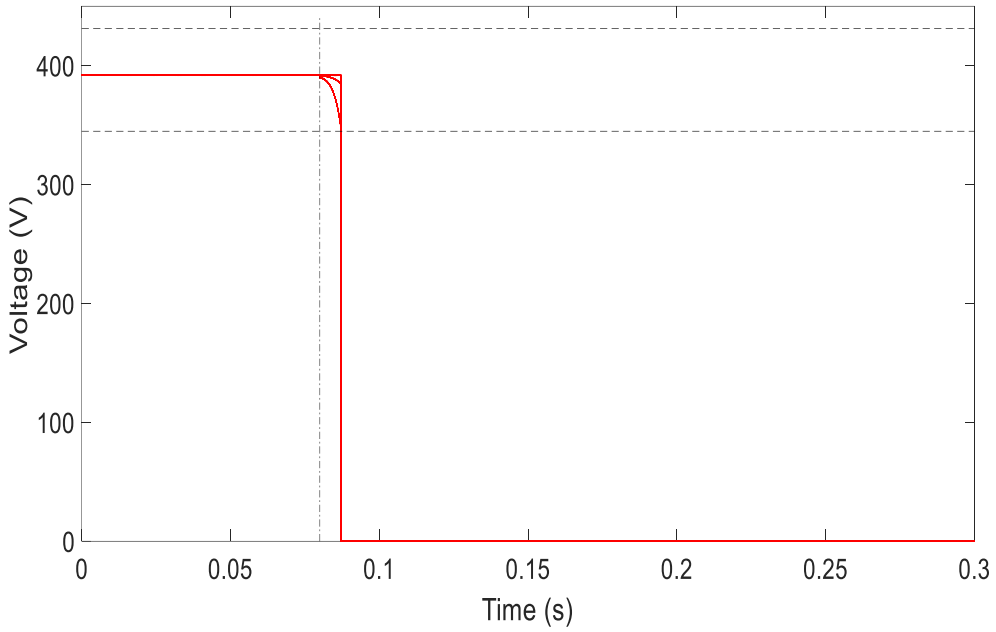

Figure 3.27 All PV (91 PVs) voltages at PCC before and after the breaker opens (anti-islanding scheme enabled)

3.8 DAE based dynamic analysis of the PV inverters in microgrid

In recent years, the cost reduction and technology improvements of power electronic devices are enabling the concept of microgrid. Microgrid is defined as a subsystem of DGs and associated loads that can be operated either in grid-connected mode, or in autonomous mode [115]. In the grid-connected mode, the main grid determines the frequency and voltages of the system, while the DGs are controlled to inject the desired level of power into the system. In the autonomous mode, the frequency and voltages of the system are controlled by the DGs. In addition, a droop control is used to share the loads among the DGs installed in the system. The benefits of the autonomous operation of the microgrid include the convenience of maintenance by preplanned islanding and the consistent power supply

during the unplanned islanding. To maintain the power balance between the load and the DG output, the DGs are required to operate under the well-established controls.

Several control strategies have been proposed for the DGs during the autonomous operation of the microgrid [115-118]. Such controls are designed and verified through EMTP simulations and hardware testing in small-scale microgrid systems. In this section, the proposed DAE based dynamic modeling and analysis method is used to design and verify the PV inverter controllers, for the autonomous operation of larger-scale microgrid.

3.8.1 Controller design for autonomous microgrid

As shown in Figure 3.28, the average model of the PV inverter for the autonomous microgrid includes a PV filter, a power controller and a voltage controller. For each phase, state space models are derived for each PV inverter components in *dq* frame.

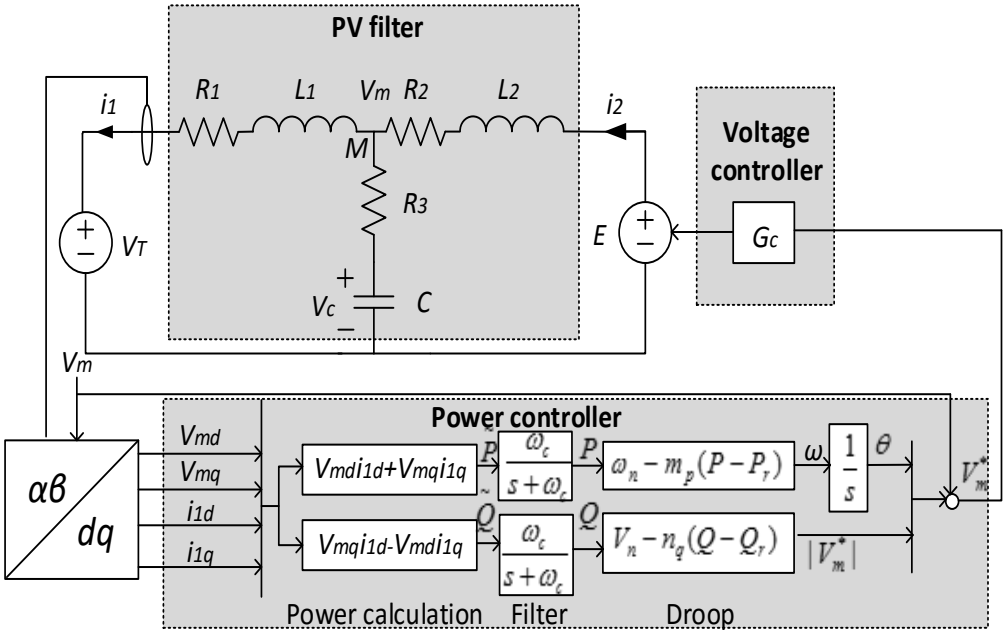

Figure 3.28 Average model of the PV inverter for autonomous microgrid mode

The instantaneous active and reactive power components $\tilde{P}$ and $\tilde{Q}$ are given by

$$\tilde{P} = V_{md} i_{1d} + V_{mq} i_{1q} \tag{3.21}$$

$$\tilde{Q} = V_{mq} i_{1d} - V_{md} i_{1q} \tag{3.22}$$

where, V_{md} and V_{mq} are the voltage V_m on the d frame and q frame respectively.

The calculated $\tilde{P}$ and $\tilde{Q}$ are passed through low-pass filters to remove the fluctuations of the 120 Hz components, and produce average values of the output powers P and Q. The average values of P and Q are given by

$$P = \frac{\omega_c}{s + \omega_c} \tilde{P} \tag{3.23}$$

$$Q = \frac{\omega_c}{s + \omega_c} \tilde{Q} \tag{3.24}$$

where, ω_c is chosen to be one-tenth of the fundamental frequency.

In the power controller, the droop control block is designed based on the method used in the conventional synchronous generators. In the droop controller, the active power output of the inverter is a function of the frequency. In addition, the reactive power output is controlled by controlling voltage magnitude of V_m. The relation between active power and frequency, and reactive power and voltage is given by

$$\omega = \omega_n - m_p (P - P_r) \tag{3.25}$$

$$V_m = V_n - n_q (Q - Q_r) \tag{3.26}$$

where, ω_n, V_n, P_r and Q_r are the rated frequency, rated voltage, rated active power and rated reactive power of the system respectively. m_p, n_q are the active power droop coefficients and reactive power droop coefficient of the inverter respectively.

Droop control characteristic plots based on (3.25) and (3.26) are shown in Figure 3.29.

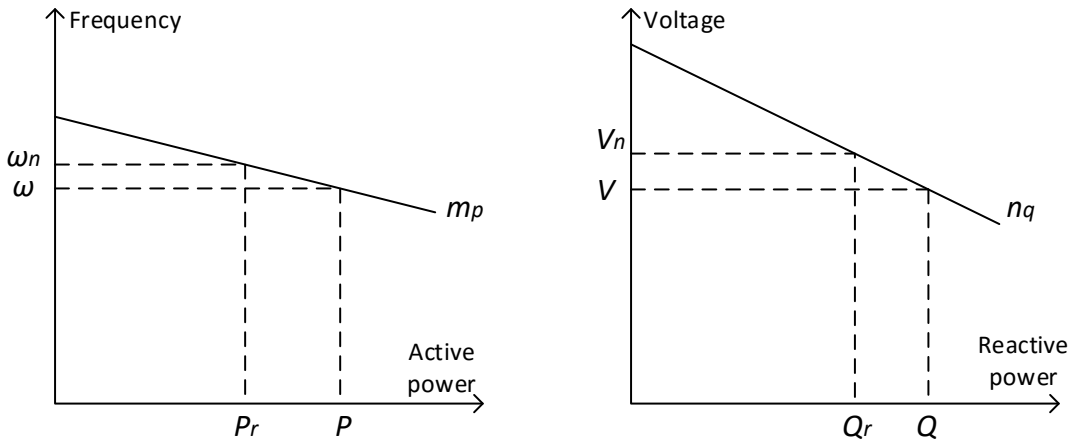

(a) (b)

Figure 3.29 Droop control characteristic plots of (a) real power and (b) reactive power

The outputs of the power controller are the voltage magnitude and angular frequency. The voltage magnitude and angular frequency serve as input to the voltage controller. The output of the voltage controller determines the terminal voltage *E*, as shown in Figure 3.28.

The complete state space models are written into a DLL based on (3.9) and (3.21)-(3.26). Separate DLLs are created for PV inverters with different ratings. Each PV inverter DLL has its own reference frame rotating at a speed of ω, calculated from (3.25). To interface the PV inverters with the OpenDSS network model, a common reference frame is defined with a nominal frequency. The output current from each PV inverter is converted to the common reference frame, using the transformation given by (3.6). Similarly, the input voltage at each PV inverter PCC is transformed to the reference frame by (3.6).

3.8.2 Implementation of the PV inverters in small-scale microgrid system

A small-scale microgrid system is built in OpenDSS to verify the control capabilities illustrated in Figure 3.28. The system is a four-bus system with two PV units and one unbalanced load illustrated in Figure 3.30. The two PV units, PV1 and PV2 are rated at 75

kW each. The droop coefficients m_p and n_q of the two PV units are same, as shown in Table 3.1.

Table 3.1 Droop coefficients used for the PV systems

m_p	0.000041867
n_q	0.0001

Initially, the substation is providing power to the circuit. At 1 s, the utility breaker is opened and the total loads are shared equally by the two PV units. Figure 3.31and Figure 3.32 show the real and reactive power supplied by the PV units before and after the breaker opens.

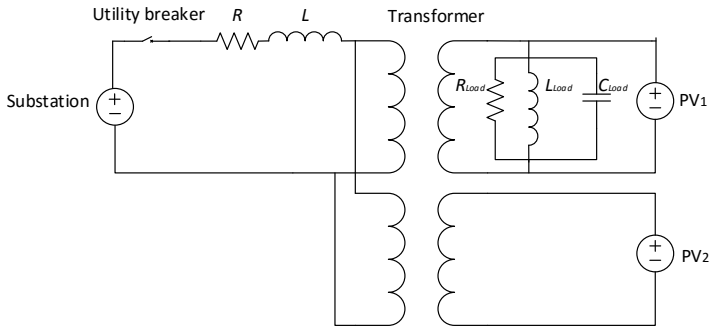

Figure 3.30 Small-scale system used for droop controller verification

Before the breaker opens, the PV units are operating at the rated power. After the breaker opens, the real and reactive power of the PV units are controlled based on the inverter frequency and terminal voltages. After the transients, the PV units settle at the same frequency. In addition, in the small system, the terminal voltages of the PV units are close to each other. Therefore, with the same droop coefficients and power ratings defined for the two PVs, the real and reactive power is shared by the two PV units, equally for each phase. This is shown in Figure 3.31and Figure 3.32

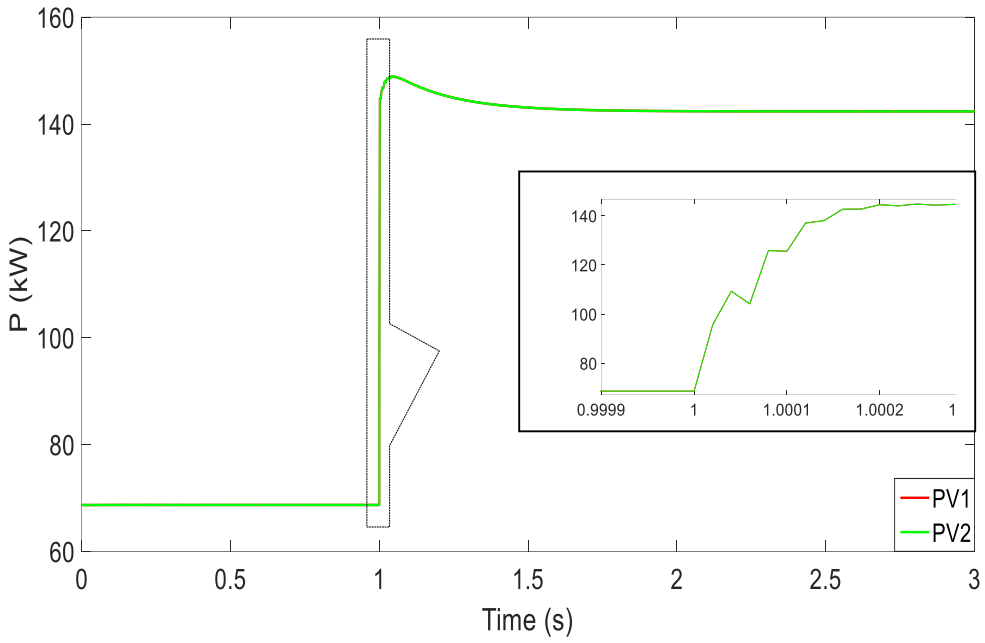

Figure 3.31 Real power outputs from the two PVs before and after islanding in small-scale microgrid

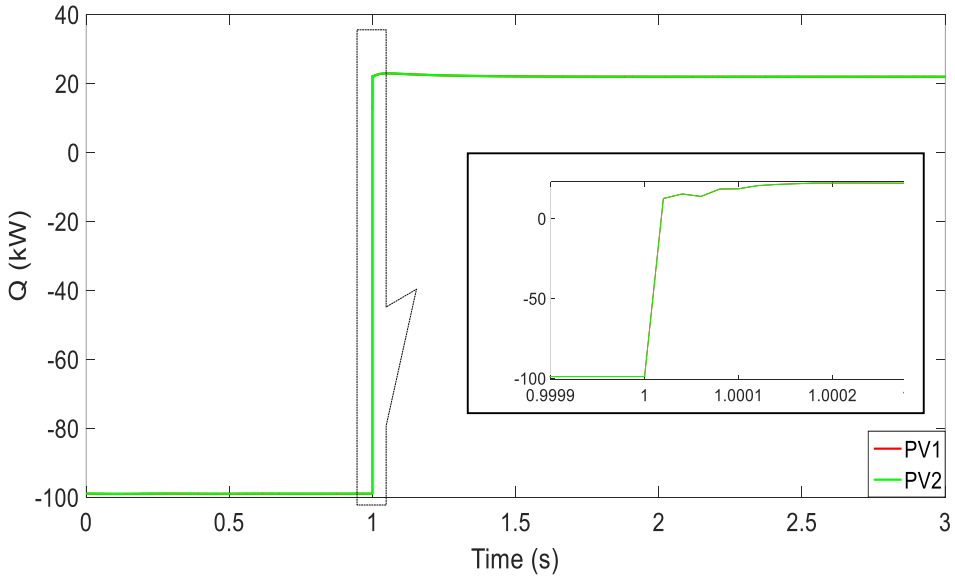

Figure 3.32 Reactive power outputs from the two PVs before and after islanding in small-scale microgrid

3.8.3 Implementation of the PV inverters in 123-bus microgrid system

To illustrate the advantages of the DAE based dynamic analysis method proposed in this work, the microgrid operations are tested on the IEEE 123-bus system. Three large-scale PV systems are installed respectively at bus 1, bus 7 and bus 47. The ratings of the three PV systems are 525 kW each. The power controller of the three PV units has the same droop settings, as shown in Table 3.1.

At 1 s, the breaker near the substation is opened. The power supplied by the three PV systems is plotted in Figure 3.33 and Figure 3.34. Before the breaker opens, the three PV systems are supplying power based on their ratings. After the breaker opens, the lost generation is picked up by the PV units based on the droop characteristics. With the selected droop coefficients and power ratings, the PV units share the lost generation equally. With the selected droop coefficients and power ratings, the PV units share the total loads equally, as shown in Figure 3.33. The reactive power outputs of the three CIGs are different as shown in Figure 3.34, due to different impedance seen by each PV unit.

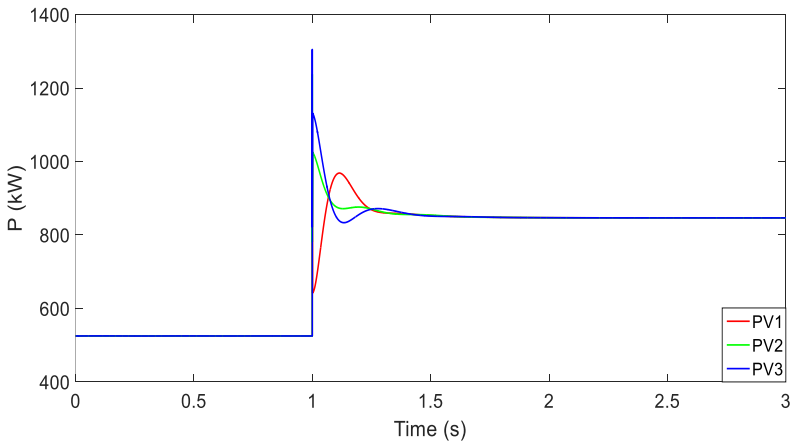

Figure 3.33 Real power outputs from the three PVs before and after islanding in 123-bus microgrid

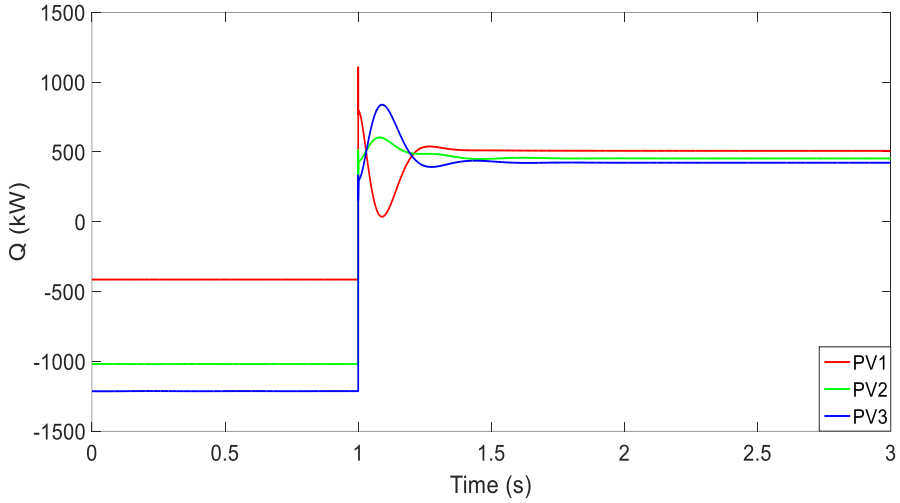

Figure 3.34 Reactive power outputs from the three PVs before and after islanding in 123-bus microgrid

CHAPTER 4: AUTOMATED PROTECTION ANALYSIS FOR A LARGE DISTRIBUTION FEEDER WITH HIGH PENETRATION OF PHOTOVOLTAIC SYSTEM

4.1 Introduction

A conventional distribution feeder is usually designed as a radial system with a single source feeding the downstream system. Protective devices including circuit breakers, reclosers and fuses are installed in the system under proper protection coordination [80]. The circuit breakers and the reclosers are located on the main line system, while the fuses are placed on the laterals, the sub-laterals and the customer locations. A typical distribution feeder is composed of thousands of overhead lines and secondary lines, with hundreds of fuses installed in the system. An accurate system model is therefore required to examine whether the system is under proper protection coordination for all possible types and locations of the faults. Protection coordination includes relay-fuse coordination, relay-recloser coordination, recloser-fuse coordination and fuse-fuse coordination in both primary and secondary sides.

Based on the accurate feeder model built and verified in Chapter 2, a protection analysis approach is proposed here. This approach helps in a thorough verification and design of a proper system protection under all types of protection coordination.

The penetration levels of distributed renewable resources especially PV in power distribution systems are increasing at a rapid rate. Present distribution infrastructure that is designed mainly for unidirectional power flow with well-controlled generation, poses challenges to integration of large scale PV in terms of the protection.

Possible loss of protection coordination caused by DG has been discussed in the literature [48-54]. Integrating PV in distribution systems could affect the fuse-fuse coordination. When a PV system is located upstream of the two existing coordinated fuses, the fault currents flowing through both fuses under downstream faults would increase due to the additional current contribution from the upstream PV system. If the fault currents exceed the ratings specified in the fuse curves, the fuse-fuse coordination is lost. When a PV system is installed downstream of the fuses, the fault contribution from PV may cause the upstream fuse to blow during upstream faults. However, this action cannot isolate the faults. In addition, PV systems can affect the recloser-fuse and relay-fuse coordination. The sensitivity of the phase and ground relay/recloser may be reduced while the fault current seen by fuses can be increased due to PV fault contribution, depending on the PV locations relative to the location of the faults. The PV interface transformer connections also have a substantial influence on the recloser-fuse and relay-fuse coordination.

There are five commonly used DG interface transformer connections [47]. The commonly used interface transformer connections are as follows:

1. HV side delta and LV side delta
2. HV side delta and LV side ungrounded wye
3. HV side ungrounded wye and LV side delta
4. HV side grounded wye and LV side delta
5. HV side grounded wye and LV side grounded wye.

The grounded transformer secondary would create ground paths between the transformer and the PV inverter [95], which allows short circuit current flowing through the anti-parallel diode during the grid voltage's negative half-cycle. Therefore, in this work,

only the connection types of 1 to 4, including the HV side delta or ungrounded wye, and the HV side grounded wye/LV side delta, are considered. Each type of the connection has both advantages and disadvantages, as listed in Table 4.1.

Table 4.1 Disadvantage and advantages of different interconnection transformer connections

<table>
<tr><th>HV side connection</th><th>LV side connection</th><th>Disadvantage</th><th>Advantage</th></tr>
<tr><td>Delta</td><td>Delta</td><td rowspan="3">Overvoltage may occur on the healthy phase during the grid-side ground fault</td><td rowspan="3">1. No source of zero-sequence current for grid-side ground fault
2. No ground current seen at the grid side during LV side faults</td></tr>
<tr><td>Delta</td><td>Ungrounded wye</td></tr>
<tr><td>Ungrounded wye</td><td>Delta</td></tr>
<tr><td>Grounded wye</td><td>Delta</td><td>Establish a zero-sequence current source for grid-side ground fault</td><td>No overvoltage problem</td></tr>
</table>

When the HV side is connected as delta or ungrounded wye, there is no source of zero-sequence current to affect the ground relay/recloser sensitivity. In addition, no ground current is seen by the grid-side protective devices during the inverter LV side faults. However, overvoltage problems of the inverter may occur during the grid-side faults with ungrounded HV side connections. When the HV side is connected as grounded wye and the LV side as delta, no overvoltage problems occur during the grid-side faults. This is due to

the low-impedance grounded neutral at the high-voltage side. However, the ground-relay/recloser sensitivity is much affected. During the grid-side ground faults, the zero-sequence fault current flows towards the substation as well as the grounded neutral of the PV interconnection transformer. This reduces the fault current seen by the ground-relay/recloser. As the PV ratings increase, the impedance of the interconnection transformer decreases. This further worsens the sensitivity problems of the relay/recloser. During the grid-side phase faults, the sensitivity of the phase-relay/recloser is also affected with all types of transformer connections due to presence of PV systems. However, the impacts are not as significant compared to the ground faults. The reduced sensitivity of the relay/recloser may cause mis-coordination of relay-fuse and recloser-fuse under fuse-saving scheme. The potential problems of the interface transformers connections have been probed in literatures. However, a complete investigation of the impact of PV during both ground faults and phase faults with all the possible PV interface transformer connections in realist feeder has not been done yet. Table 4.2 summarizes the impact of PV on the ground and phase relay/recloser under different transformer connections respectively. With the detailed model of the real distribution system, PV systems and loads, all the cases listed in Table 4.2 are thoroughly studied in this work.

Protection coordination is closely related to the fuse schemes adopted in the systems. Either a fuse-saving scheme or a fuse-clearing scheme is implemented in the system based on reliability requirements of the utility [91]. In a fuse-saving scheme [82], the relay and fast recloser operate faster than the downstream fuses. Since the system faults are mostly temporary faults, a fuse-saving scheme can prevent the sustained interruptions due to fuse tripping under momentary faults. In a fuse-clearing scheme [83], fuses are set to clear the

faults and the upstream relay and reclosers as back-up protection. The fuse-clearing scheme prevents the system upstream to the opened fuse from fault interruptions. The advantages and disadvantages of the fuse-saving and fuse-clearing scheme are not the topic of this work. The effects of PV on both the schemes have been studied here.

Table 4.2 Impacts of PV interface transformer connections on phase/ground relay/recloser

	HV side delta or ungrounded wye connection	HV side grounded wye/LV side delta connection
Phase relay/recloser	Positive-sequence current contributed from PV reduces the sensitivity	Positive-sequence current contributed from PV reduces the sensitivity
Ground relay/recloser	PV interconnection transformer is not included in the zero-sequence circuit, the sensitivity is not affected	1. PV interconnection transformer is included in the zero-sequence circuit, and the sensitivity is much affected, depending on the PV ratings. 2. The sensitivity is independent of the PV status

The system under study is being operated by the utility under the fuse-clearing scheme. The protective devices including fuses, relay and recloser are modeled based on the types and ratings provided by the utility. Further, all types of the protection coordination are verified in the system without and with PV, under the fuse-clearing scheme. In addition, the system is studied under the fuse-saving scheme. Under the fuse-saving

scheme, the relay and recloser are re-designed to coordinate properly for all fault cases. This is done by using an optimization method based on the fault cases applied, without and with PV systems. The methodology introduced in this work includes both verification and re-design of the protective devices. This can be used in other feeders under either a fuse-clearing scheme or a fuse-saving scheme.

4.2 System settings under protection analysis

Protective devices including fuses, reclosers and relays are utilized in the feeder studied under the fuse-clearing scheme. The types and ratings of the protective devices are defined accordingly. This chapter introduces the method of defining the protective devices in the system model built in Chapter 2. To study the switching from the fuse-clearing scheme to the fuse-saving scheme, settings of all protective devices except the fuses already installed in the system need to be re-defined. This topic has also been addressed in this chapter.

4.2.1 Modeling of the fuses

All fuses in the system, including lateral fuses, transformer fuses and load-side fuses are modeled in this work. GIS data and utility standards are used for modeling the fuses in the system. The modelling process is further illustrated as follows:

Lateral fuses

Totally around 200 lateral and sub-laterals fuses are installed in the feeder. The location, make and rating of these fuses are given in GIS data provided by the utility. Since OpenDSS does not provide time-current-curve (TCC) for protective devices, TCCs of all fuse types used were defined in the model.

Protective device library in CYMTCC is used to extract several corresponding time and current values for each fuse type and these values are stored in MATLAB as fuse type libraries. The fault current through the fuse known is obtained from the fault simulations. Based on the simulated fault current, the fuse melting and clearing time is computed by linear interpolation of the stored TCC values in the corresponding fuse type library. Fuse libraries are also created for transformer fuses and load-side fuses.

Transformer fuses

There are 1000 single-phase and three-phase transformers in the feeder. External primary-side fuses are installed for both the protection of the transformers as well as back-up protection for the secondary sides. Based on the utility standards, each transformer fuse is determined by its transformer kVA rating. This enables the transformer fuses to withstand the inrush currents when transformers are energized [84], and not operate under normal transformer loading.

Load-side fuses

The types and ratings of the load-side fuses are not included in the GIS data. To verify the transformer fuse-lateral fuse coordination, the load-side fuses are placed downstream of all the transformer secondary terminals. The load-side fuses are defined from the fault simulation results according to the following criteria:

- The load-side fuse can operate under minimum fault current of the secondary branches
- The maximum fault current cannot exceed the load-side fuse ratings.

Since in distribution systems, most faults are low-impedance faults, in this work only bolted fault cases are considered. The minimum fault levels for the load-side fuses are due

to faults at the load branch ends. The maximum faults levels are due to the faults at the nearest nodes downstream of the load-side fuse.

All fault cases including the load-side fuse fault cases will be introduced later in the chapter. After finding the maximum and minimum fault currents seen by the load-side fuses due to the load-side fuse fault cases, rating of each load-side fuse is defined accordingly to satisfy the above criteria.

4.2.2 Modeling of the relay and recloser

Relay and recloser settings given in the GIS data are suitable for the fuse-clearing scheme. Similar to the process of defining the lateral fuses, the extracted time and current values for the corresponding ground and phase relay/recloser are stored separately in MATLAB as libraries. The linear interpolation method is applied to calculate the operation time of the relay/recloser from the fault current obtained by performing fault simulations.

4.2.3 Modeling of the PV systems

There are over 100 small residential PVs and two large-scale PVs in the feeder studied. The inverters connected to PVs produce the fault currents between 1 to 5 times the inverter rated current for 1 to 4.25 ms, depending on the inverter types [85]. In the protection coordination study of this work, fault contributions for these PVs are set as 120% of the inverter rated current for all the fault cases.

4.3 Validation of the protection coordination under fuse-clearing scheme

There are around 5000 overhead lines and secondary lines, and 200 fuses installed in the system. Hence, an automated process is required to find out all the fault cases to conduct a complete protection coordination study. The protection coordination study includes:

1. Transformer fuse-load side fuse coordination

2. Lateral fuse-lateral fuse coordination
3. Recloser-lateral fuse coordination
4. Relay-lateral fuse coordination
5. Relay-recloser coordination.

To study each protection coordination, the most critical cases of faults need to be studied. Therefore, the maximum and minimum fault current cases, which are the most critical cases from a protection perspective, need to be found. Additionally, the protection zone for each type of the protective device is defined. The locations nearest to the downstream protective device under protection coordination are set as the maximum fault current locations. The locations farthest to the downstream protective device under protection coordination are set as the minimum fault current locations. The load-side fuses protect the region from the corresponding transformer secondary terminals to the load branch ends. The transformer fuses protect the region from the transformer primary side to the load end, and act as a back-up protection for the load-side fuses. Lateral fuses protect the region from downstream of the lateral fuses until the transformer primary sides. The recloser and the relay protect the system primary sides, and act as back-up protection for the downstream lateral fuses since they are at the same voltage level. In addition, the relay is coordinates with the recloser and acts as a back-up protection.

To illustrate more clearly, Figure 4.1 gives an example of the protection zones for the protective devices in a small system. Figure 4.1 shows all the possible protection coordination types that are present in the real system under study. In Figure 4.1, the blue-dash circles, red-dash circles and purple-dash circles represents respectively the protection

zones for the fuses, the recloser, and the relay. In each circled protection zones of the protective devices in Figure 4.1, the black boxes labeled from F1 to F26 represent the fault locations to conduct the maximum or minimum fault current cases. In the real feeder studied, the protection zones are defined in a similar way, but more number of zones are found.

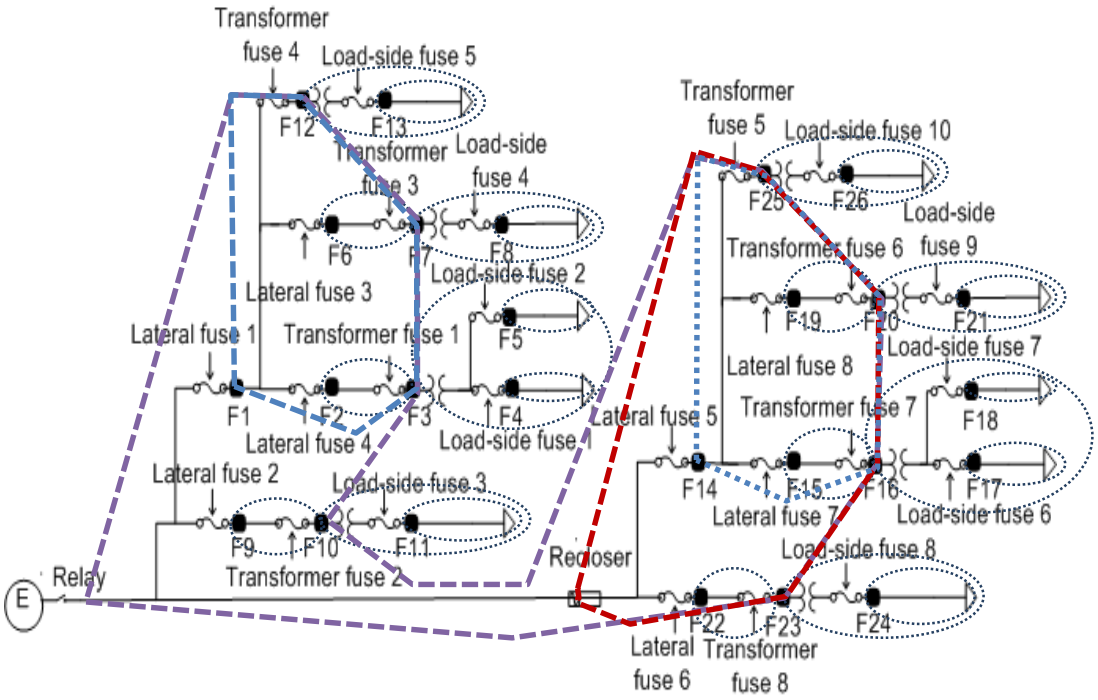

Figure 4.1 The example for protection zones under fuse-clearing scheme (purple zone is protected by the relay, red zone is protected by the recloser, and the blue zone is protected by the fuses)

In order to find all the coordinated protective devices, and define the corresponding fault locations for the maximum and minimum fault current cases in the large feeder, a fast and automated way is required. Based on the feeder topology, an adjacency matrix is constructed, storing information about which feeder sections are adjacent to the other sections, starting from the substation node to the ends of all the sections in the feeder. The pseudo code for the creation of the adjacency matrix is illustrated in Figure 4.2.

Algorithm Creation of adjacency matrix

```
1: AdjMatrix ← ∅, NdList ← ∅, SecList ← ∅
2: Enqueue(NdList,HeadNd)
3: for each nd ∈ Section[HeadNd].Node & nd ∉ NdList do
4:    Enqueue(NdList,nd)
5:    Enqueue(SecList,Section[HeadNd])
6:    NewNd ← nd
7: end for
8: Count ← 0
9: while Count≠0 do
10:   for each nd ∈ NewNd  do
11:      NewSec ←SUB Nd2Sec(nd,SecList)
12:      if NewSec∉∅ then
13:         for each sec ∈ NewSec do
14:            Enqueue(SecList,sec)
15:            DwNd←SUB Sec2Nd(sec,NdList)
16:            AdjMatrix[nd,DwNd] ← 1
17:            Enqueue(NdList,DwNd)
18:            Count+=1
19:         end for
20:      end if
21:   end for
22: end while
23: SUB Nd2Sec(nd,SecList)
24: sec ← Section[nd]
25: NewSec ← ∅
26: for each sec do
27:   if sec ∉SecList then
28:      Enqueue(NewSec,sec)
29:   end if
30: end for
31: SUB Sec2Nd(sec,NdList)
32: nd ← Node[sec]
33: DwNd ← ∅
34: for each nd do
35:   if nd ∉NdList then
36:      Enqueue(DwNd,nd)
37:   end if
38: end for
```

Figure 4.2 Algorithm used to create the adjacency matrix

In Figure 4.2, the creation of the adjacency matrix starts by storing the substation node (head node) into the node list, and the section connecting to the substation node into the section list (see lines 1-7). The main loop of the program is defined in lines 8-22. In each loop, the downstream nodes/sections directly connected to the nodes/sections in the node lists/section list are found and stored into the node list/section list. In addition, the information of the directly connected upstream node and downstream node is recorded into the adjacency list. The loop iterates as long as there are new nodes/sections found. From the adjacency matrix, the upstream and downstream relations of the nodes and sections in the feeder topology can be clearly obtained.

By associating the feeder sections to the protective devices, all the coordinated upstream and downstream protective devices are found. Additionally, the downstream fault locations for maximum and minimum fault current cases are found. The information of the coordinated protective devices and the corresponding fault cases to be applied are stored as fault case packages. The fault case packages are categorized under the five protection coordination schemes, as shown in Table 4.3. As listed in Table 4.3, the fault cases under the recloser-lateral fuse and relay-recloser coordination studies are the same. This is because the relay is working as a backup protection for the recloser in the protection zone of the recloser, as shown in the red zone in Figure 4.1.

Table 4.3 Fault case packages

Protection coordination type	Numbers of ground-fault cases found	Numbers of phase-fault cases found
Transformer fuse-load fuse	2483	24
Lateral fuse-lateral fuse	637	39
Recloser-lateral fuse	479	55
Relay- recloser	479	55
Relay-lateral fuse	398	46

The fault cases in the fault case packages are applied to the OpenDSS feeder model through MATLAB component object module (COM) interface, from which the simulation results of the fault current values are sent back to MATLAB and analyzed. This process is illustrated in Figure 4.3. The procedure for the protection coordination study through OpenDSS and MATLAB depicted in Figure 4.3 can help either verify or design new TCC settings of the protective devices.

With all the protective devices designed in the system under the fuse-clearing scheme, verification of the protection coordination is conducted without including any PV systems. All the fault cases in the packages are applied to the feeder model in OpenDSS and the fault current seen by the corresponding protective devices are recorded and sent back to the respective MATLAB protective device library. The operation time of the up-stream and downstream protective devices are calculated and compared to justify the co-ordination. The criteria for the proper coordination in the fuse-clearing scheme requires the downstream fuses blow faster than the upstream ones, and relay/recloser operate slower than the downstream fuses. Several mis-coordination cases were found with the existing protective device settings for lateral fuse-lateral fuse coordination. The fault locations for these cases are plotted in Figure 4.4. The cause of the mis-coordination is due to the higher fault current values seen by the upstream and downstream fuses compared to the intersec-tion current values of the two fuse TCCs. One example of such a mis-coordination case is shown in Figure 4.4.

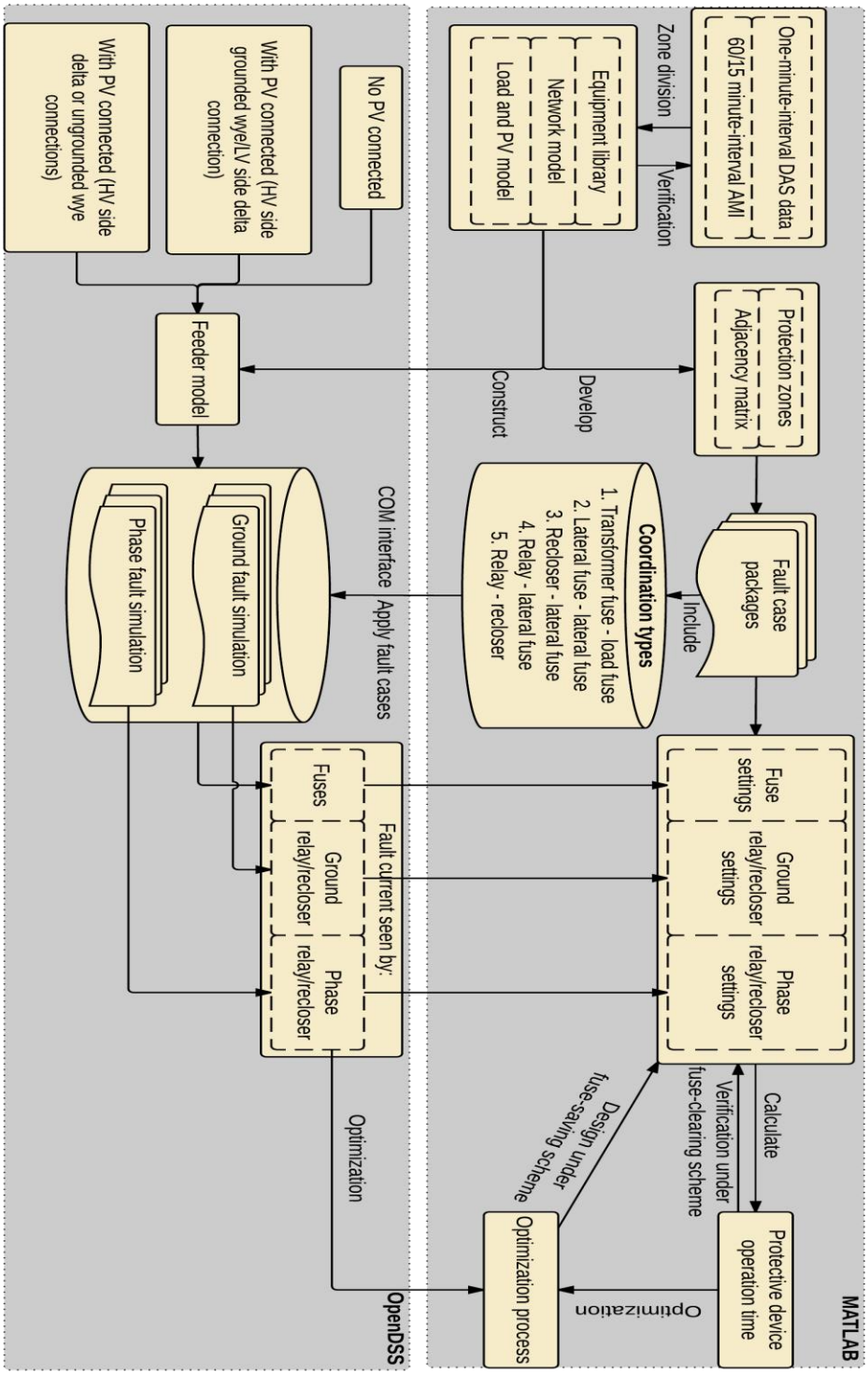

Figure 4.3 Procedure of the protection coordination study through OpenDSS and MATLAB

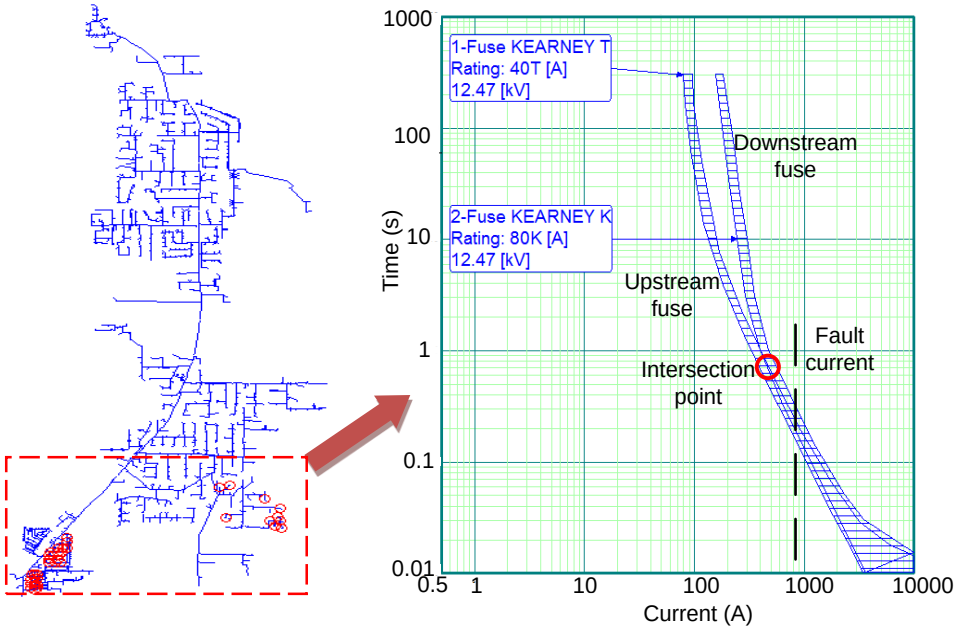

Figure 4.4 Fault locations in the mis- coordination fault cases (shown as small red circles in the left feeder diagram), and the upstream and downstream fuse TCCs (shown in the right diagram) in one mis-coordination case found

With PV systems in the feeder, all fault cases are reapplied to investigate the impact of PV. As discussed in section 4.1, fuse-fuse coordination may be lost under the following conditions:

1. When the fault current contribution from upstream PV systems exceeds the fuse ratings
2. The fault current contribution from the downstream PV systems trips the downstream fuses faster than opening the upstream fuses.

As the peak load in the system is around 5000 kW, the output of the large-scale PV system is increased from 0 to 5000 kW to achieve a 100% penetration level. Simulation and analysis of the results show that fuse-fuse coordination is not adversely affected due to the high PV penetration in the system. In addition, PV systems with different interface

transformers will not cause relay-fuse and recloser-fuse coordination problems. The simulation results reveal that all types of device coordination are not adversely affected under the fuse-clearing scheme due to increase in PV penetration levels.

4.4 Design of the protective device under fuse-saving scheme

If a utility plans to move from a fuse-clearing to a fuse-saving scheme, the impact of PV on such a scheme needs to be evaluated. To switch from a fuse-clearing scheme to a fuse-saving scheme, the following changes need to be made:

1. The ground and phase recloser and relay need to be re-designed, so that the fast relay/recloser operates before the melting of the corresponding downstream fuses
2. The slow relay/recloser needs to be reset accordingly to act as a backup protection.

With more than 4000 fault cases stored in the fault case packages, the trial and error method is of low efficiency. This is because the settings of the relay and the recloser need to be changed based on each fault case simulation to obtain the proper coordination. Since the operation time of the relay/recloser is an inverse function of the fault current seen by the device [85], the TCC characteristic can be expressed as

$$t(I_{fault}) = TD \cdot \left[\frac{A}{\left(\frac{I_{fault}}{I_{pickup}} \right)^{p} - 1} + B \right] \tag{4.1}$$

where, t is relay/recloser operation time in seconds with fault current I_{fault} seen by relay/recloser, TD is the time dial setting and I_{pickup} represents relay/recloser pickup current, A, B and p are the constants of the TCC expressions.

An optimization method is proposed here to determine the fast relay/recloser settings that the proper coordination can be maintained under all fault cases.

The same make and type of the relay/recloser are chosen for the fuse-saving scheme as in the fuse-clearing scheme. The values of the parameters *A*, *B* and *p* are found by curve fitting of the equation (4.1) to the relay/recloser curves in CYMTCC library. The values of *A*, *B* and *p* are listed in Table 4.4. The nonlinear curve-fitting function *lsqcurvefit* in MATLAB is used for this purpose.

Table 4.4 Values of parameters *A*, *B* and *p*

	A	*B*	*p*
Recloser	0.0006717	0.0672	2
Relay	0.4468	0.0834	2

The unknown values of *TD* and I_{pickup} for the relay/recloser are to be determined by the proposed optimization method based on the simulation results of all the fault cases in the fault case packages. The pickup current I_{pickup_phase} for the phase relay/recloser is required to be at least 30% higher than the maximum load current I_{maxL}, while being less than the minimum phase fault current I_{min_phase} in the system. The pickup current I_{pickup_ground} for the ground relay/recloser should be at least 2 times of the maximum unbalanced current I_{0maxL}, while being less than the minimum ground faults in the system, as shown in (4.2)-(4.3) respectively.

$$I_{min\_phase} > I_{pickup\_phase} > 1.3 I_{maxL} \tag{4.2}$$

$$I_{min\_ground} > I_{pickup\_ground} > 2 I_{0maxL} \tag{4.3}$$

Since the lower boundaries of I_{pickup} vary with time, feeder configuration, resident numbers and PV penetration levels, finding the maximum I_{pickup} and *TD* values as the threshold values is critical so that there is no risk of false operation due to possible increased I_{pickup} lower boundary values.

The optimization process determines the pickup current and *TD* values for the ground relay/ recloser based on the ground fault cases, and for the phase relay/recloser based on the phase fault cases. Only the process to determine the pickup current and *TD* values of the ground relay/recloser is introduced in detail in the following sections. The phase relay/recloser can be designed in a similar way. PV systems are not included in the initial analysis. The settings of the relay/recloser will be changed and analyzed later with different ratings and interconnection types of PV systems included. The optimization problem is formulated and it is solved using MATLAB optimization function *fmincon* as well as AMPL. The optimization problem formed has a linear objective function and both linear and nonlinear inequality constraints.

4.4.1 Relay/recloser settings without PV systems

The objective of the optimization problem is to maximize the sum of pickup current values I_{BRE_pickup} and I_{REC_pickup}, and the time dial values TD_{BRE} and TD_{REC} of the neutral relay and recloser, subject to the proper protection coordination in all ground fault cases. The objective function is given by

$$Maximize \quad \frac{I_{BRE\_\text{pickup}}}{2 \cdot I_{0\max L\_BRE}} + \frac{I_{\text{REC\_pickup}}}{2 \cdot I_{0\max L\_REC}} + TD_{BRE} + TD_{REC} \tag{4.4}$$

where, I_{0maxL_BRE} and I_{0maxL_REC} are the maximum unbalanced current seen by the relay/recloser. Based on the field measurements, I_{0maxL_BRE} and I_{0maxL_REC} are 50 A in the feeder studied.

The nonlinear inequality constraints of the relay/recloser operating time based protection coordination are defined by

$$\vec{t}_{jREC} < \vec{t}_{jfuse} \tag{4.5}$$

$$\vec{t}_{jBRE} < \vec{t}_{jfuse} \tag{4.6}$$

$$\vec{t}_{jREC} < \vec{t}_{jBRE} \tag{4.7}$$

$$2 > \vec{t}_{jREC} > 0 \tag{4.8}$$

$$2 > \vec{t}_{jBRE} > 0 \tag{4.9}$$

$$\vec{t}_{iBRE} < \vec{t}_{ifuse} \tag{4.10}$$

$$2 > \vec{t}_{iBRE} > 0 \tag{4.11}$$

where, variables $\vec{t}_{jREC}$, $\vec{t}_{jBRE}$ and $\vec{t}_{jfuse}$ represent the vector containing the operation time of the recloser, relay and fuses respectively for the ground fault case *j*, in the protection zone of the recloser. This formulation is used for the recloser-lateral fuse coordination (and relay-recloser coordination) studies in the fault case packages. t_{jfuse} is calculated from the fault current seen by the fuse in the fault case *j*, based on the corresponding fuse type library.

The operation time t_{jREC} and t_{jBRE} can be obtained from (4.1) and Table 4.4 as

$$t_{jREC} = TD_{REC} \cdot \left[\frac{0.0006717}{\left(\frac{I_{jfault\_REC}}{I_{REC\_pickup}} \right)^2 - 1} + 0.0672 \right] \tag{4.12}$$

$$t_{jBRE} = TD_{BRE} \cdot \left[\frac{0.4468}{\left(\frac{I_{jfault\_BRE}}{I_{BRE\_pickup}} \right)^2 - 1} + 0.0834 \right] \tag{4.13}$$

where, I_{jfault_REC} and I_{jfault_BRE} are the fault current seen by the recloser and relay in the fault case *j* applied.

In (4.10)-(4.11), variables $\vec{t}_{iBRE}$ and $\vec{t}_{ifuse}$ represent the operation time of the relay and fuses respectively for the ground fault case *i*, in the protection zone of the relay up-stream of the recloser. This formulation is used for the relay-lateral fuse coordination studies in the fault case packages. t_{iBRE} can be also expressed by (4.13) with the corresponding fault current I_{ifault_BRE} seen by relay when the fault case *i* is applied.

In addition, the upper and lower bound linear constraints of the time dial and pickup current values as follows

$$11 \geq TD_{REC} \geq 0.1 \tag{4.14}$$

$$11 \geq TD_{BRE} \geq 0.1 \tag{4.15}$$

$$min(I_{fault\_REC}) \geq I_{REC\_pickup} \geq 2I_{0maxL\_REC} \tag{4.16}$$

$$min(I_{fault\_BRE}) \geq I_{BRE\_pickup} \geq 2I_{0maxL\_BRE} \tag{4.17}$$

$$0.3690 I_{BRE\_pickup} \leq I_{REC\_pickup} \leq 0.7 I_{BRE\_pickup} \tag{4.18}$$

where, $min(I_{fault\_REC})$ and $min(I_{fault\_BRE})$ represent respectively the minimum ground fault current seen by the recloser and the relay in all the fault cases. The lower bound constraints for the pickup current settings of the ground relay/recloser are respectively two times of I_{0maxL_BRE} and I_{0maxL_REC}, both equaling to 100 A. Since the recloser is located downstream of the relay, the current seen by the recloser is less than that seen by the relay. Based on the field measurements of current values at the substation and the recloser in the one year data, range of the current flowing through the recloser is defined in (4.18) as a portion of the current seen by the relay.

The ground relay/recloser settings are derived by solving the above formulated optimization problem in (4.4)-(4.18), based on the ground fault cases stored in the fault case packages. The results of the ground relay/recloser settings are listed in Table 4.5.

The phase relay/recloser settings are also defined also in a similar way with linear constraints changed from (4.16)-(4.17) to (4.19)-(4.20).

$$min(I_{fault\_REC}) \geq I_{REC\_pickup} \geq 1.3 I_{maxL\_REC} \tag{4.19}$$

$$min(I_{fault\_BRE}) \geq I_{BRE\_pickup} \geq 1.3 I_{maxL\_BRE} \tag{4.20}$$

where, I_{maxL_REC} and I_{maxL_BRE} are respectively the maximum phase current seen by the recloser and the relay. As seen from the field measurements, the maximum phase current seen by the relay and recloser are 270 A and 125 A respectively. Therefore, the lower bound constraints for the pickup current settings of the phase relay/recloser are 351 A and 162.5 A respectively.

The reformulated optimization problem given by (4.4)-(4.15) for the phase relay/recloser settings is solved, based on the phase fault cases stored in the fault case packages. The results of the phase relay/recloser settings are listed in Table 4.5.

Table 4.5 Settings of the relay/recloser without PV systems

	Time dial values (s)	Pickup current values (A)
Ground relay	0.1	313.0595
Ground recloser	0.1248	219.1416
Phase relay	0.1	700.1850
Phase recloser	0.1540	490.1295

4.4.2 Relay/recloser settings with PV systems (HV side grounded wye/LV side delta interface transformer connection)

Different PV interface transformer connections have different impacts on the phase and ground relay/recloser sensitivity. Therefore, the design of the relay/recloser is divided into two parts depending on the large PV interface transformer connections. The first design is based on the interface transformer connection of HV side grounded wye/LV side delta. The second design is based on the HV side delta/LV side delta connection.

The large-scale PV system is modeled in the feeder, with the HV side grounded wye/LV side delta interface transformer connection. The rating of the large-scale PV system is increased from 0 to 5000 kW in steps of 1000 kW. For each PV output level, all the fault cases in the fault case packages are simulated, and the settings of the relay/recloser are found by the optimization process illustrated in the previous section. The lower bounds on the pickup current values are not changed, since the PV outputs vary throughout the day. The results of the ground and phase settings are listed in Table 4.6 and Table 4.7. As seen from Table 4.6 and Table 4.7, the fault current seen by the relay/recloser is reduced when the outputs of the PV system increased. Therefore, the reduced values of the pickup current are required for a faster operation of the relay/recloser. When the PV rating is larger than 3000 kW, the sensitivity of the ground relay/recloser is reduced to the extent that the end of the feeder cannot be reached with the lower bound constraints for the pickup current settings. The impacts of PV on the phase relay/recloser are less significant as compared to the ground relay/recloser. This is illustrated in Table 4.6 and Table 4.7.

Table 4.6 Settings of the ground relay/recloser with PV systems (grounded wye/delta)

	PV rating (kW)				
	1000	2000	3000	4000	5000
Ground relay TD (s)	0.1079	0.1610	-	-	-
Ground recloser TD (s)	0.1270	0.1897	-	-	-
Ground relay pickup current (A)	238.4496	158.0739	-	-	-
Ground recloser pickup current (A)	166.9147	110.6517	-	-	-

Table 4.7 Settings of the phase relay/recloser with PV systems (grounded wye/delta)

	PV rating (kW)				
	1000	2000	3000	4000	5000
Phase relay TD (s)	0.1	0.1	0.1	0.1	0.1
Phase recloser TD (s)	0.1502	0.1475	0.1455	0.1439	0.1429
Phase relay pickup current (A)	668.6668	647.9514	631.0567	618.2521	609.8235
Phase recloser pickup current (A)	468.0668	453.5660	441.7397	432.7765	426.8764

A new recloser is proposed to be installed near one DAS system in the downstream feeder when the PV rating is above 3000 kW, and the feeder is divided into two zones. The two zones are protected by the existing upstream recloser and the new downstream recloser respectively during ground faults. DAS 3 is found to be the suitable location for installing

the new recloser, such that the existing recloser settings remain within the constraints. The settings for the existing ground relay/recloser as well as the new recloser are listed in Table 4.8. Since the large-scale PV system is located downstream of the new recloser, the fault current seen by the new recloser during downstream ground faults is increased with the increase of PV ratings. Therefore, the pickup current values for the new recloser are increased with larger PV ratings, as indicated from Table 4.8.

Table 4.8 Settings of the original ground relay/recloser and the new recloser with PV systems above 3000 kW

	PV rating (kW)		
	3000	4000	5000
Ground relay TD (s)	0.1	0.1348	0.1673
Ground recloser TD (s)	0.1239	0.1655	0.2040
Ground relay pickup current (A)	347.2082	287.4623	241.6373
Ground recloser pickup current (A)	243.0457	201.2236	169.1461
New ground recloser TD (s)	0.3023	0.2991	0.2970
New ground recloser pickup current (A)	603.4912	612.4259	618.7742

4.4.3 Relay/recloser settings with PV systems (HV side delta/LV side delta interface transformer connection)

When the PV interconnection transformer is connected as HV side delta/LV side delta, the flow of zero sequence currents is not allowed. Hence, the PV interconnection transformer is not included in the zero-sequence circuit. In this way, the ground relay/recloser sensitivity is not affected by the change of PV ratings. The impact of PV on the phase relay/recloser sensitivity is almost negligible. To study the impact of PV with the

delta/delta connection, the output of the large-scale PV system is increased from 0 to 5000 kW in steps of 1000 kW. The fault cases are regenerated and the solved relay/recloser settings are given in Table 4.9 and Table 4.10. As seen from Table 4.9 and Table 4.10, the settings of the relay/recloser are not changed significantly with the increase of PV system outputs. Therefore, when PV interconnection transformer is connected as delta/delta, settings for the relay/recloser can be set as constant, equaling to the values when PV outputs are 5000 kW shown in Table 4.9 and Table 4.10.

Table 4.9 Settings of the ground relay/recloser with PV systems (delta /delta)

	PV rating (kW)				
	1000	2000	3000	4000	5000
Ground relay TD (s)	0.1	0.1	0.1	0.1	0.1
Ground recloser TD (s)	0.1222	0.1214	0.1208	0.1205	0.1204
Ground relay pickup current (A)	283.4085	273.3307	266.4541	263.0624	262.1205
Ground recloser pickup current (A)	198.3859	191.3315	186.5179	184.1437	183.4844

Table 4.10 Settings of the phase relay/recloser with PV systems (delta /delta)

	PV rating (kW)				
	1000	2000	3000	4000	5000
Phase relay TD (s)	0.1	0.1	0.1	0.1	0.1
Phase recloser TD (s)	0.1502	0.1475	0.1455	0.1439	0.1429
Phase relay pickup current (A)	668.6668	647.9514	631.0567	618.2521	609.8235
Phase recloser pickup current (A)	468.0668	453.5660	441.7397	432.7765	426.8764

4.4.4 Summary of the impacts of PV ratings and interconnection transformer types on relay/recloser settings

The impacts of both the PV ratings and the PV interconnection transformer types on the ground and phase reclosers respectively are highlighted in Figure 4.5. Figure 4.5 is generated from the data listed in Table 4.5 to Table 4.10. Only the impacts on the pickup current values are illustrated in Figure 4.5. The impacts on the TD values are similar and not plotted here. As seen from Figure 4.5, the change of the PV ratings has significant impact on the pickup current settings of the ground reclosers when the transformer is connected as ground wye/delta. The effect is not significant when the transformer is connected as delta/delta. In addition, the phase recloser settings are not substantially influenced by the PV ratings when the transformer is connected as ground wye/delta or delta/delta. As indicated from Figure 4.6, the impacts of both the PV ratings and PV interconnection transformer types on the relay settings are similar to the impacts on the recloser settings.

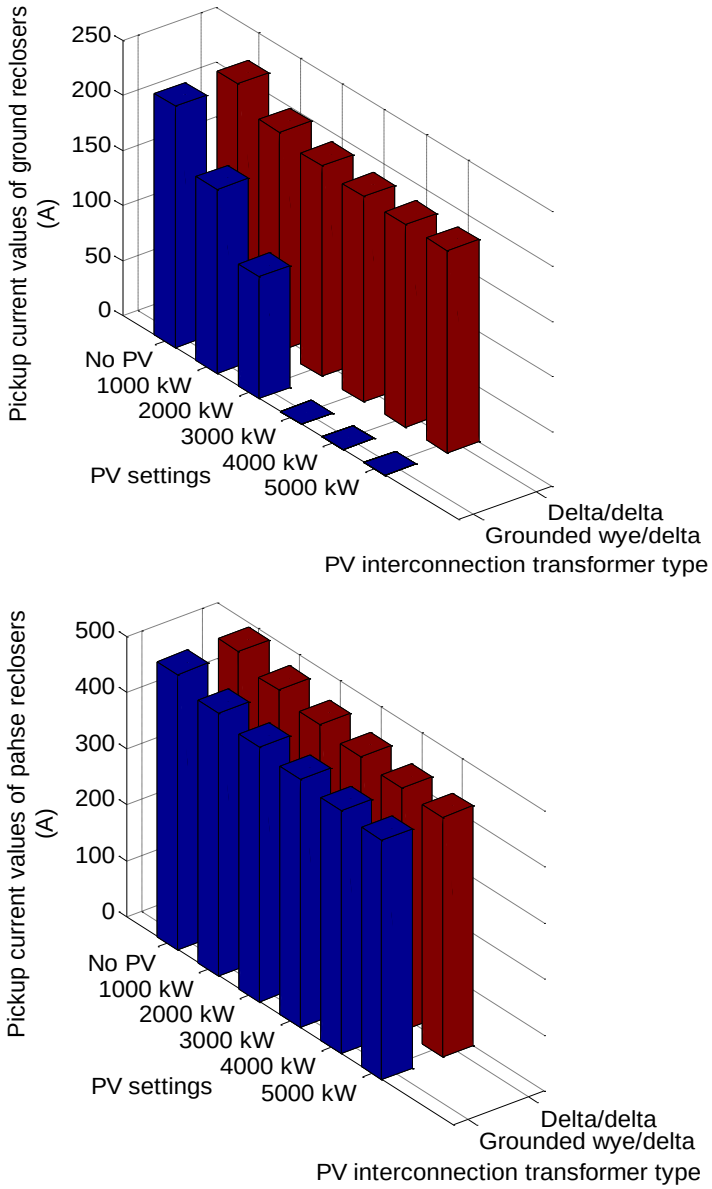

Figure 4.5 Pickup current values of the ground/phase reclosers under different PV ratings and interconnection transformer types

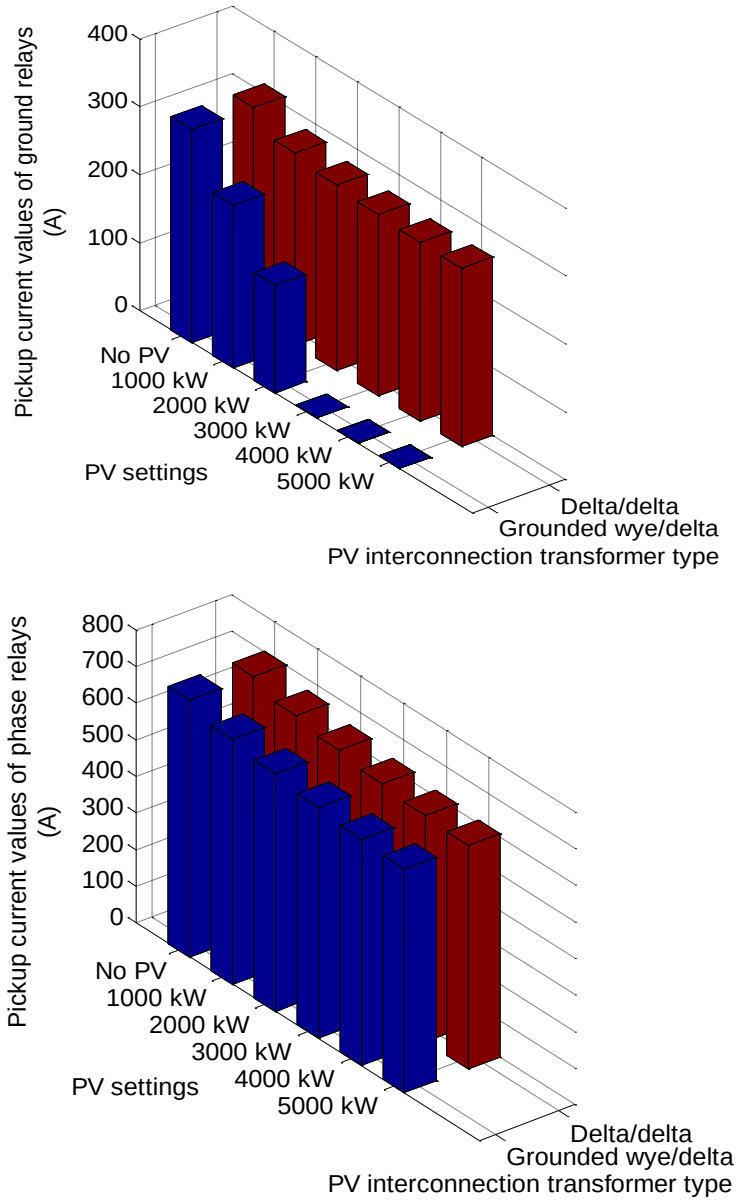

Figure 4.6 Pickup current values of the ground/phase relays under different PV ratings and interconnection transformer types

It can be concluded that, with the ground wye/delta connection of the PV interconnection transformer, significant changes in the relay/recloser settings are needed when the PV penetration in the system is increased. Under high PV penetration, additional reclosers have to be installed downstream of the original reclosers, since the sensitivity of the relay/recloser is reduced significantly. The analysis presented in this chapter can be used to

determine the proper settings of the relay/recloser, when the PV penetration levels in the system increases.

With the delta/delta connection of the PV interconnection transformer, settings of the relay/recloser are not affected significantly due to the increase in PV penetration levels. In this case, the relay/recloser can be set at value calculated with the largest possible PV ratings in the feeder.

CHAPTER 5: VOLTAGE-SAG-BASED FAULT LOCATION IDENTIFICATION METHODOLOGY IN DISTRIBUTION SYSTEM

5.1 Introduction

Increasing the reliability of the distribution system is one of the main objective of the smart grid initiatives. The system reliability is quantified by reliability indices such as system average interruption duration index (SAIDI), customer average interruption duration index (CAIDI) and customer total average interruption duration index (CTAIDI). These indices depend on the interruption duration [86]. If the fault locations are pinpointed in an accurate and fast way, the faults can be isolated more efficiently. Therefore, the duration of the fault interruptions is reduced, resulting in the improved system reliability. Hence, an accurate and efficient fault location identification methodology is essential in distribution systems.

To enable an efficient and accurate method for locating faults, a systematic fault location identification process is introduced in this chapter. Figure 5.1 shows a block diagram of the proposed fault location identification process. The fault location identification methodology is mainly based on the fault event data recorded by DAS along the feeder. The methodology consists of two major parts:

1. The off-line training, which includes feeder zone division and CART training. This part helps identify the corresponding fault zones for the fault locations. Whenever the feeder topology is changed, the feeder model as well as the off-line training can be updated accordingly. The topology changes may include an increase in the number of residential customers, or replacement of the line segments or both

2. The on-line analysis of the fault event data. When a fault occurs, the fast on-line analysis reads in the fault event data, and pinpoints the fault location with the corresponding fault type.

Two actual fault event cases provided by the utility are analyzed by the fault location identification methodology. The correctly identified fault locations verify the effectiveness of the methodology proposed.

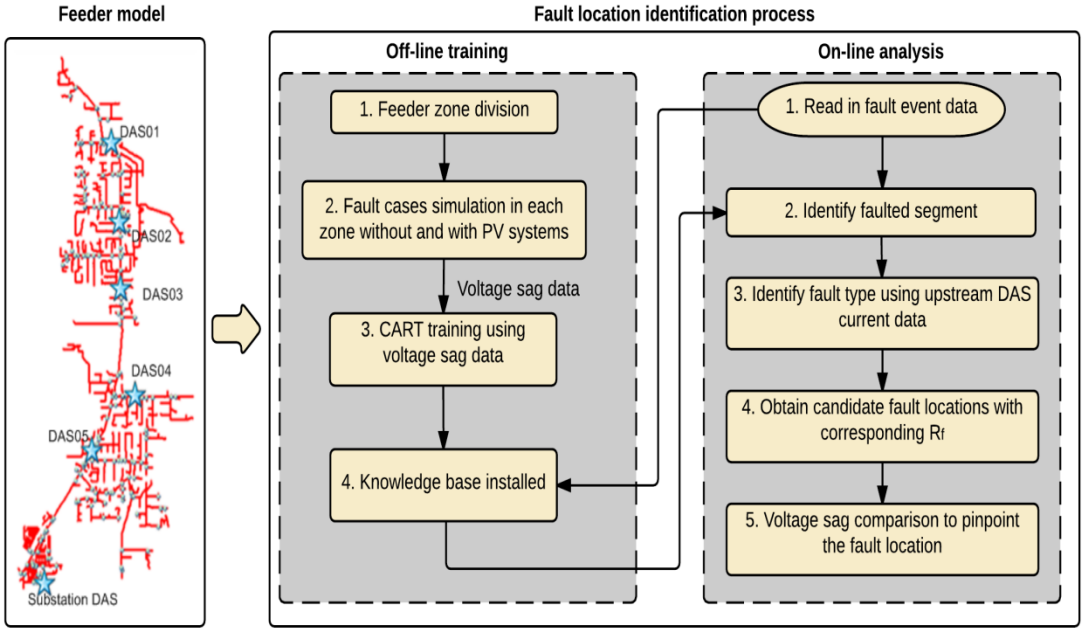

Figure 5.1 Block diagram of the fault location identification

5.2 Off-line training procedure

With the fault event data available from DAS along the feeder, the voltage-sag based method is used to pinpoint the fault location. In the proposed method, the fault location is identified by:

1. Applying a fault on every tentative feeder node

2. Comparing the simulated during-fault current and voltage sag data to the measured ones

Due to the complexity of the distribution feeder, which contains thousands of laterals and sublaterals, a large number of the fault cases need to be simulated if all the nodes on the feeder are assumed as possible fault locations. In order to reduce computation burden and increase efficiency of the proposed method, the off-line training procedure is introduced.

As proposed in [88-89], the decision-tree (DT) method was successfully applied in several works to estimate the fault sections. In comparison to other black-box solution methods like neural networks, the knowledge-based DT method is more transparent. In this work, the feeder is divided into several fault zones based on the event data available from DAS. Faults with different fault impedance values in each zone produce different voltage sags at the DAS locations. The DT can be trained off-line to develop an internal rule between the inputs (the given voltage sag values at several DAS) and the predictive objective (the fault zone). Therefore, the off-line training helps to reduce the computation burden during the on-line analysis.

5.2.1 Decision trees

In a general classification problem, given a set of predictor variables and target categorical variables, a binary tree structure denoted as the classification rule is developed to predict what target class a predictor is in. The mathematical representation of the DT algorithm [89-90] is built on the following definitions (5.1)-(5.3).

$$\overline{X} = \{X_1, \quad X_2, \quad \ldots \quad X_m\} \tag{5.1}$$

$$C = \{1, \quad 2, \quad ... \quad J\} \tag{5.2}$$

$$A_j = \{X_i; d(X_i) = j\} \tag{5.3}$$

where $\overline{X}$ is a m-dimensional vector of the predictor variables X_1, X_2, ... X_m, C is a set of target classes containing class of 1, 2, ..., J. A classification rule A_j is a function $d(X_i)$ defined on $\overline{X}$ such that for each X_i, $d(X_i)$ is equal to one of the target classes.

The construction of a DT proposed by Breiman [89-90] is composed of three steps: growing the tree regardless of the tree size, pruning tree with decreased sequence of subtrees, and tree selection based on the cross-validation method. During the growing of the DT in the first step, the *Gini* index defined in (5.4) is used as an impurity function to select the best split at each internal node.

$$i(t) = \sum_{m \neq n} p(m \mid t)\, p(n \mid t) \tag{5.4}$$

where, $p(m|t)$ and $p(n|t)$ is the probability of a given sample at node t belonging to the class m and n respectively.

Starting from the root, a large tree is grown by continued splitting until all the terminal nodes are pure (the node cases are all in one class) or nearly pure. Then the tree is pruned based on the misclassification cost $R(T)$ defined in (5.5).

$$R(T) = \sum_{t \in \tilde{T}} \{r(t) \cdot p(t)\} \tag{5.5}$$

where, T is a binary tree, $r(t)$ is the re-substituition estimate of the misclassification error of a case in node t, $p(t)$ is the probability that any case falls into node t.

The optimal DT model T_{ko} is selected by cross-validation so that the misclassification error $R(T_{ko})$ for the tree is minimized, as expressed in (5.6).

$$R(T_{ko}) = \min_{k}\{R(T_k)\}, k = 1, 2, ..., K \tag{5.6}$$

where, k is the tree index number, and $R(T_k)$ is the misclassification error for the tree T_k.

The tree growing and pruning algorithm discussed in the preceding paragraphs, has been incorporated into the data mining software CART, which has been developed by Salford Systems, CA [36]. In this work:

1. The simulated voltage sag measurements are recorded from OpenDSS
2. The database generation and analysis is conducted in MATLAB
3. The off-line training and testing of the DT based on the voltage sags are implemented in CART.

The block diagram of the process is shown in Figure 5.2.

5.2.2 DT training in CART

The feeder can be divided into several zones based on the DAS locations. Although there are 6 DAS installed along the feeder, not all of them are triggered during the faults. Depending on the number of DAS available with the event data for a given fault case, the feeder is divided and the DT is trained accordingly. In the two actual fault event cases provided by the utility, the event data from DAS 5, DAS 4 and DAS 2 are available. Based on the data the feeder is divided into four fault zones, as shown in Figure 5.3.

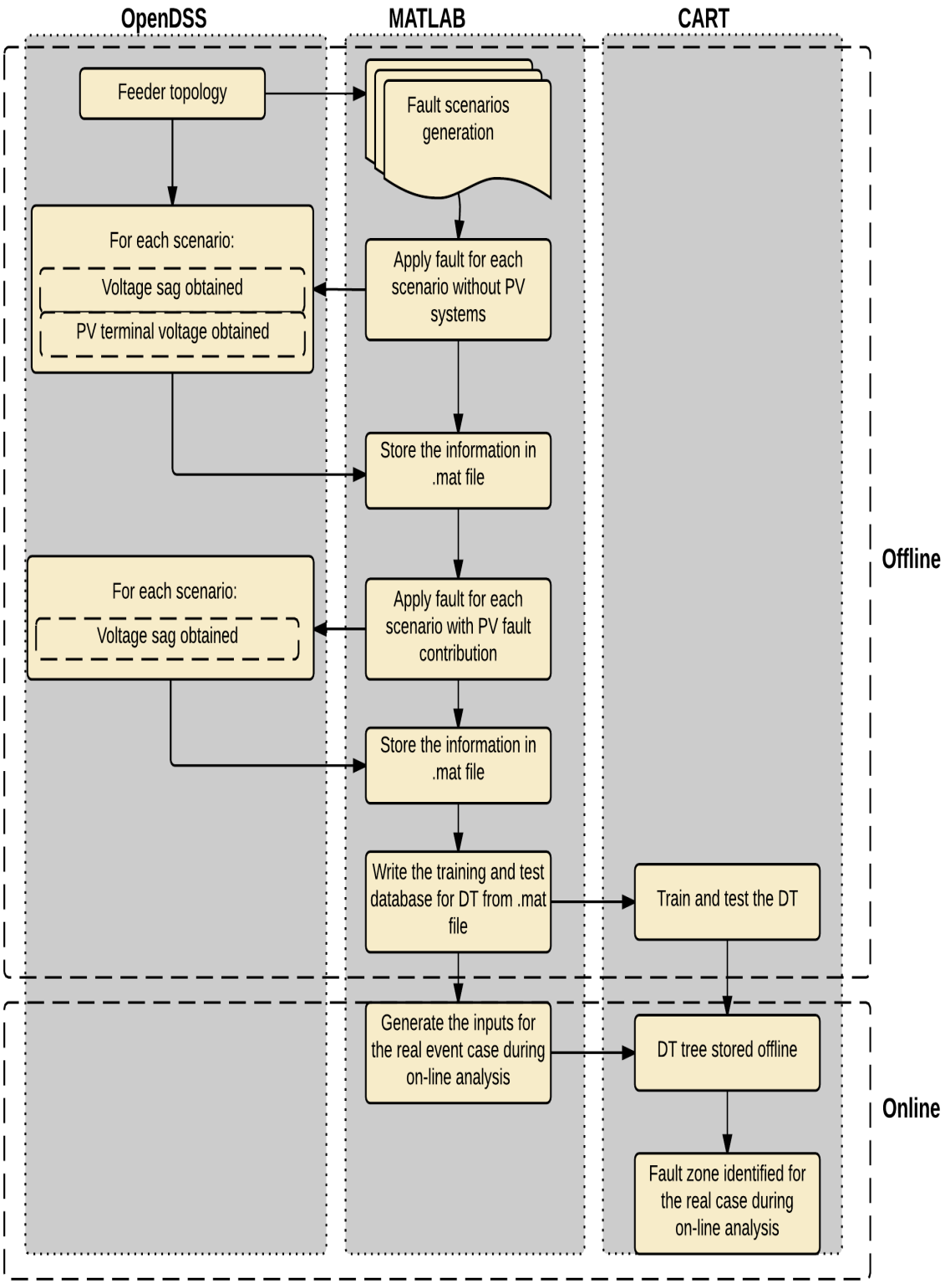

Figure 5.2 Offline-training procedure using OpenDSS, MATLAB and CART

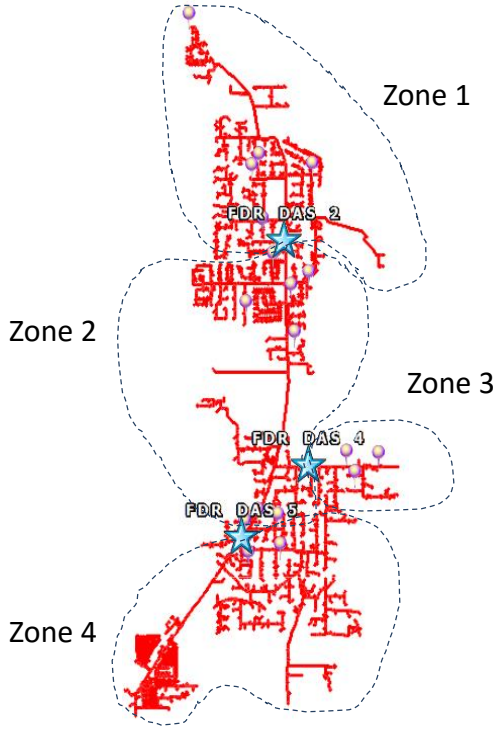

Figure 5.3 Feeder zone division based on DAS available with the event data

Generation of knowledge base without PV systems

The off-line training of the DT-based fault zone identification requires a knowledge base composed of a number of instances, and each instance represents a fault scenario including a vector of predictor variables and a target categorical variable. The predictor variables in this work are the voltage sag magnitudes and the phase angles at the DAS locations. The target categorical variables are the fault zone numbers from 1 to 4. In the feeder studied, there are 2867 possible single-phase-ground fault cases. In consideration of possible measurement errors accounted in the event data recorded by DAS, and the variation of the fault resistance values, each fault is applied on the feeder with fault resistance values ranging from 0 to 30 Ω. The resistance is changed between 0 to 30 Ω in steps of 1 Ω for each case. As a result, a database containing 2867 * 31 = 88877 fault scenarios is generated.

A random error following a normal distribution with zero mean and deviation of 0.5% is added to each fault scenario.

Generation of knowledge base with PV systems

When the large PV systems are installed in the studied feeder, the fault contributions from the PV systems need to be included in the knowledge base. The IEEE 1547 standard defines the default clearing time of the large PV systems under system disturbances with abnormal voltages. The default clearing time of the large PV systems are listed in Table 5.1. During the fault identification process, the voltage sag values are obtained from the first few cycles after the fault occurs. Since the clearing time of PV systems (given by Table 5.1) are higher than a few cycles, the PV systems are not disconnected, and the fault contribution from the PV systems is considered.

Table 5.1 IEEE 1547 interconnection system response to abnormal voltages

Voltage range (% of base voltage)	Clearing time (s)
$V < 50$	0.16
$50 \leq V \leq 88$	2.00
$110 < V < 120$	1.00
$V \geq 120$	0.16

Presently, as a "rule of thumb", the industry uses of 2 times rated current as the amount of the fault current contribution of an inverter-based DG [84]. However, the actual fault contribution from the PV inverter depends on the fault duration and the voltage at the PV terminal. In this work, the fault contribution from the PV systems is denoted as a function of the PV terminal voltages. Figure 5.4 shows the assumed variation of fault current

contribution from the PV system with the change in the PV system terminal voltage. To obtain the fault contribution of all PV systems for the 88877 fault scenarios, each fault case is run in the OpenDSS model without PV systems, and the PV terminal voltages are recorded. The corresponding fault current contribution of the PV systems are calculated based on the recorded terminal voltages and the characteristics described in Figure 5.4. The fault cases are then reapplied by including the calculated PV fault contribution. In this way, another database including 88877 fault scenarios with PV systems is generated. Depending on the time of the fault event and connection status of the PV systems, the database with or without PV systems is chosen for training, testing and fault zone identification.

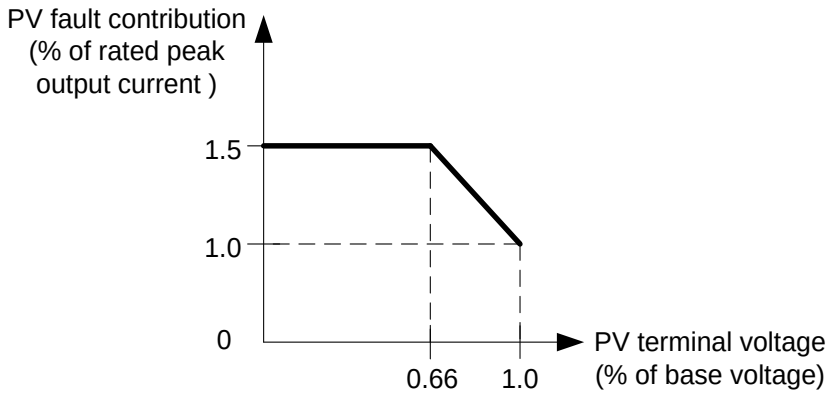

Figure 5.4 Assumed PV fault contribution curve based on the PV terminal voltage values

Training of the DT

The two databases generated, with and without the PV systems respectively, are used for the DT training. The time for the DT training, including the tree growing, pruning and selecting the best-pruned tree, takes less than 1 minute, as indicated from the built-in clock of CART. As an example, the topology of the resulting DT for the database without PV systems is shown in Figure 5.5. The DT tree in Figure 5.5 contains 114 nodes. The block above the tree shows the detail of the three nodes. To examine the performance of the DT,

the untrained fault scenarios are used as the test cases. Considering the variation of the fault resistance and the fault contribution from the PV systems, 9 groups of test cases are created. The total number of the test cases in the 9 groups is 2867 * 9 = 22936. The test results are listed in Table 5.2. As seen from Table 5.2, the average fault zone identification accuracy is above 99.7%.

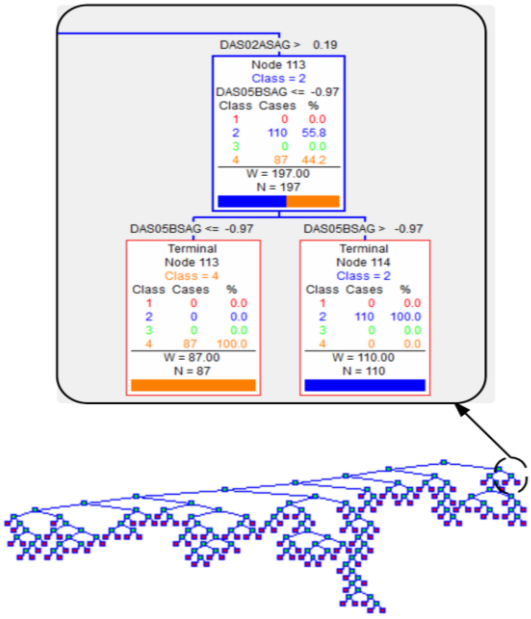

Figure 5.5 DT topology developed for the database

Table 5.2 Accuracy of the DT developed

Test group	Detail of the test group (R_f is the fault resistance)	Accuracy of the fault zone identification
1	R_f = 0 Ω, no measurement error	99.30%
2	R_f = 0 Ω, random error of ~N(0,0.5%) applied	99.30%
3	R_f = 10 Ω, no measurement error	99.86%
4	R_f = 10 Ω, random error of ~N(0,0.5%) applied	99.93%
5	R_f = 20 Ω, no measurement error	99.90%
6	R_f = 20 Ω, random error of ~N(0,0.5%) applied	99.90%
7	R_f = 30 Ω, no measurement error	99.79%
8	R_f = 30 Ω, random error of ~N(0,0.5%) applied	99.86%

The two actual event cases have also been tested in the DT, and the fault zones are identified correctly based on the fault location provided by the utility. Details of the actual case study are discussed later in the chapter.

5.3 On-line analysis procedure

When a fault occurs, the fault events are recorded and transferred to the utility, and the fault location is analyzed on-line. The on-line analysis of the fault location needs to be accurate and fast, so that the utility can clear the faults in time and maintain the system reliability. This section introduces an automated fault-locating tool developed in MATLAB, containing the fast on-line analysis of fault types and fault locations.

5.3.1 Fault type identification

Figure 5.6 shows the overall procedure for the fault type identification. The process starts by reading in the fault event data when a fault occurs and triggers the DAS. A tool is developed in MATLAB to:

1. Store and plot the current and voltage profiles
2. Analyze the event time by searching for peak current values
3. Calculate the during-fault voltage sag values for all available event data sent by each DAS.

Sometimes event data are unavailable from the substation or the other DAS. It is therefore necessary to identify the fault zone before classifying the fault types. This process helps to choose the specific DAS upstream of the fault, which needs to be analyzed. As discussed in Section 5.2.2, based on the voltage sag data obtained from the DAS measurements for the two actual event cases, the off-line trained DT in CART can successfully

identify the fault zones. In both the actual event cases, the event data from DAS 5 are used to identify the fault types. This is because DAS 5 is upstream of both the identified fault zones.

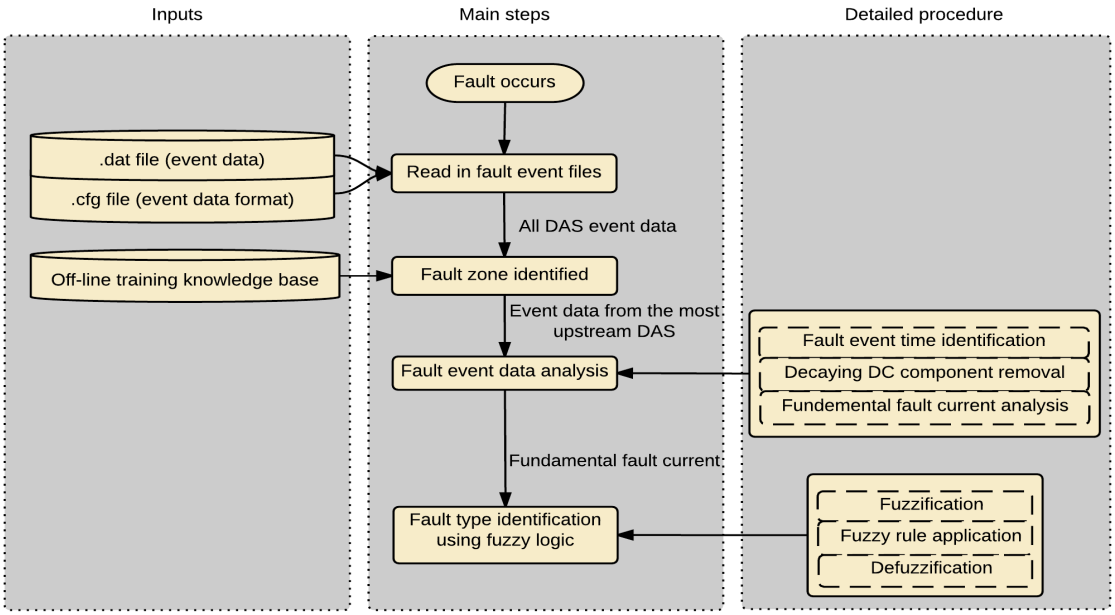

Figure 5.6 Block diagram of fault type identification

Obtain fundamental fault current

The fault current consists of a fundamental component, harmonics and a decaying dc component, as expressed in (5.7).

$$i_f(t) = I_0 e^{-t/\tau} + \sum_{h=1}^{p} I_h \sin(h\omega_1 t + \theta_k) \tag{5.7}$$

where, I_0 and τ are the magnitude and time constant of the decaying dc offset respectively, I_k and θ_k are the magnitude and phase angle of the kth harmonic component respectively, and p is the maximum harmonic order.

Since only the fundamental component is used for the fault discrimination, the other components in (5.7) need to be removed. A dc component estimation algorithm [91] is used to calculate I_0 and τ of the decaying dc offset component, as presented in (5.8)-(5.11).

$$\int_{t-T_c}^{t} i(t)dt = -I_0\tau \cdot e^{-t/\tau}(1-e^{T_c/\tau}) = Z(t) \tag{5.8}$$

$$\int_{t-T_c+\Delta t}^{t+\Delta t} i(t)dt = -I_0\tau \cdot e^{-t/\tau}(1-e^{T_c/\tau}) \cdot e^{-\Delta t/\tau} = Z(t+\Delta t) \tag{5.9}$$

$$\tau = \frac{-T_c}{\ln \dfrac{Z(t+T_c)}{Z(t)}} \tag{5.10}$$

$$I_0 = \frac{Z(T_c)}{-\tau(e^{-T_c/\tau}-1)} \tag{5.11}$$

When (5.7) is integrated during one cycle Tc as shown in (5.8), the harmonics in the second term in (5.7) is zero, and only the first term containing dc offset component remains. The integral of (5.7) after a small time step Δt is expressed in (5.9). I0 and τ can be calculated by combining (5.8)-(5.9). The dc decaying component then can be removed from the during-fault current, by subtracting the calculated dc values at each sampling instant from the during-fault current values.

The unbalance feature in the distribution feeder current may also affect the fault type identification. Hence, the pre-fault steady state current values are subtracted from the during-fault current values to eliminate the impact of unbalance. The resulting fundamental fault current (FFC), as well as the pre-fault current, and the during-fault current are shown in Figure 5.7. A fuzzy logic-based fault-type identification method is then applied on the FFC profile using the Fuzzy Logic Toolbox in the MATLAB environment.

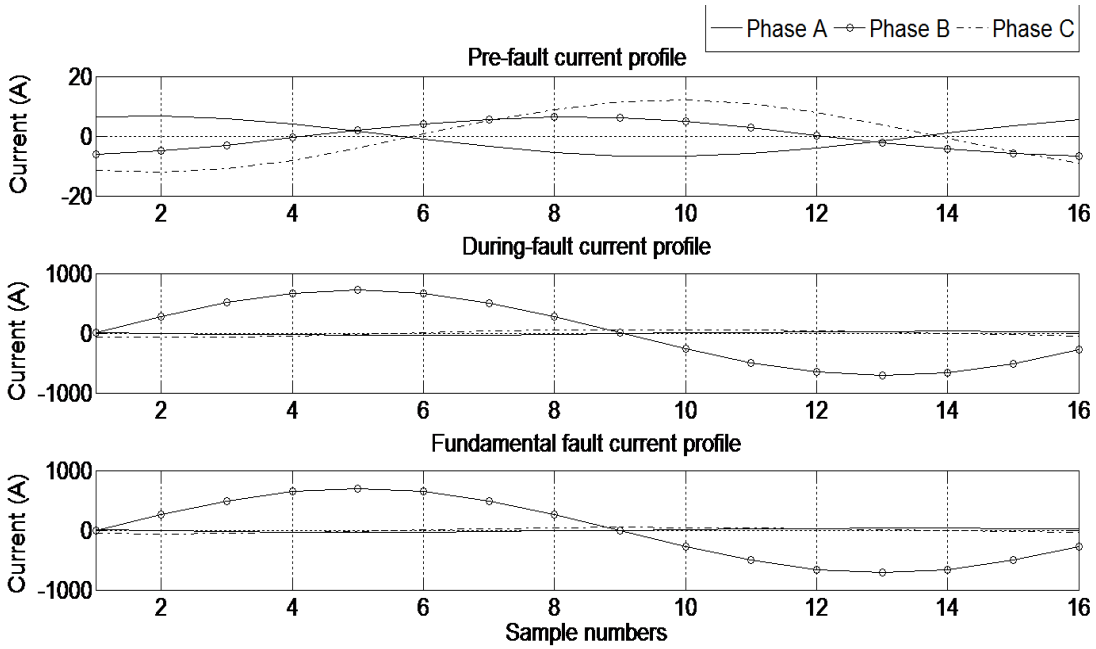

Figure 5.7 The pre-fault, the during-fault and the FFC profile

Fuzzy-logic based fault identification

Due to the non-transposed nature of the distribution system feeders, fault occurring on any of the phases can also affect the healthy phases. An appropriate technique is required to differentiate between the faulted and healthy phases. To differentiate between the faulted and the healthy phases, a fuzzy-logic based identification method is proposed in [92].

For asymmetrical faults under unloaded conditions, relations between the sequence components of the fault currents can be easily derived. The fault current due to a single line-to-ground fault, line-to-line fault and double line-to-ground fault is expressed in (5.12)-(5.14) respectively.

$$I_{a0f} = I_{a1f} = I_{a2f} \tag{5.12}$$

$$I_{a0f} = 0, \;\; I_{a1f} = -I_{a2f} \tag{5.13}$$

$$I_{a0f} + I_{a1f} + I_{a2f} = 0 \tag{5.14}$$

where, I_{a0f}, I_{a1f}, and I_{a2f} represent the zero, positive and negative current respectively.

Table 5.3 can then be used to differentiate different fault types. In Table 5.3, *ang_A*, *ang_B* and *ang_C* represent the angle difference between the positive sequence and the negative sequence of phase A, B and C in FFC respectively. R_{0f} and R_{2f} represent the ratios of $|I_{a0f}|$ to $|I_{a1f}|$ and $|I_{a2f}|$ to $|I_{a1f}|$ respectively. In Table 5.3, values of R_{0f} and R_{2f} under phase faults are denoted by K and K_1 respectively, and are calculated from (5.15)-(5.16).

$$K = \frac{Z_2}{Z_2 + Z_0 + 3Z_f} \tag{5.15}$$

$$K_1 = \frac{Z_0 + 3Z_f}{Z_2 + Z_0 + 3Z_f} \tag{5.16}$$

where, Z_2, Z_0 and Z_f are the negative sequence impedance of the line, zero sequence impedance of the line and fault impedance respectively.

Table 5.3 Fundamental relations for asymmetrical faults

Fault type	*ang_A*	*ang_B*	*ang_C*	R_{0f}	R_{2f}
a-g	0°	120°	120°	1.0	1.0
b-g	120°	0°	120°	1.0	1.0
c-g	120°	120°	0°	1.0	1.0
a-b	60°	60°	180°	0.0	1.0
b-c	180°	60°	60°	0.0	1.0
c-a	60°	180°	60°	0.0	1.0
a-b-g	60°	60°	180°	K	K_1
b-c-g	180°	60°	60°	K	K_1
c-a-g	60°	180°	60°	K	K_1
Symmetrical fault	-	-	-	0.0	0.0

In practice, the values of *ang_A*, *ang_B*, *ang_C*, R_{0f} and R_{2f} are approximately close to (but not exact) the ideal values listed in Table 5.3. The small discrepancy is due to the variation in fault locations, fault resistance, loading conditions and impact of PV system on the feeders. The approximate fuzzy variables are proposed to define the values of these five quantities using the triangular membership function, as listed in Table 5.4. This helps to eliminate the impact of variation of the feeder quantities.

The sequence components of the FFC are obtained by the discrete Fourier transform (DFT). With the obtained sequence components, the five quantities are calculated and fuzz-ified based on Table 5.4. The fault types are then classified by applying the rule base listed in Table 5.3 to the five fuzzified quantities. Consequently, the fault types obtained are also fuzzy variables and are represented by different triplets [92] as shown in Table 5.5.

Table 5.4 Fuzzy variables definition

Fuzzy variable	Triplets		
approximately 0°	0°	0°	40°
approximately 60°	25°	60°	100°
approximately 120°	85°	120°	160°
approximately 180°	140°	180°	180°
low- R_{0f}	0.0	0.0	0.2
high- R_{0f}	0.1	0.65	1
low- R_{2f}	0.0	0.0	0.2
high- R_{2f}	0.1	0.65	1

Table 5.5 Fault types represented by fuzzy variables

Fault type	Triplets		
a-g	8.5	9.0	9.5
b-g	4.5	5.0	5.5
c-g	2.5	3.0	3.5
a-b	11.5	12.0	12.5
b-c	5.5	6.0	6.5
c-a	9.5	10.0	10.5
a-b-g	12.5	13.0	13.5
b-c-g	6.5	7.0	7.5
c-a-g	10.5	11.0	11.5
Symmetrical fault	14.5	15.0	15.5

The defuzzification process is applied to obtain the final fault types based on Table 5.5. The entire fuzzy-logic based fault type identification process has been implemented using the Fuzzy Logic Toolbox in MATLAB.

5.3.2 Fault location identification with estimated fault resistance

The fault type and the feeder zone obtained from the previous sections. All feeder nodes with the corresponding faulted phase in the identified zone are recognized as the fault candidates. The fault candidates will be further analyzed during the fault location identification analysis.

The fault resistance R_f for each fault candidate is estimated by applying faults on each fault candidate node. The fault resistance is varied between 0 Ω to 40 Ω in steps of 1

Ω. The simulated steady state fault currents at the substation $I_{simulated}$ (or the most upstream DAS where the measured event data is available), are compared with the measured values, $I_{measured}$, and the mismatch between the two currents are calculated in (5.17).

$$\varepsilon_{curr} = | I_{simulated} | - | I_{measured} | \tag{5.17}$$

For one fault candidate node, the value of ε_{curr} is calculated for each R_f value. The best R_f value is chosen for the fault candidate node when ε_{curr} is within the convergence tolerance. This process is illustrated in Figure 5.8. The iteration can be continued with a reduced step size of 0.1 Ω to obtain a better approximation of R_f.

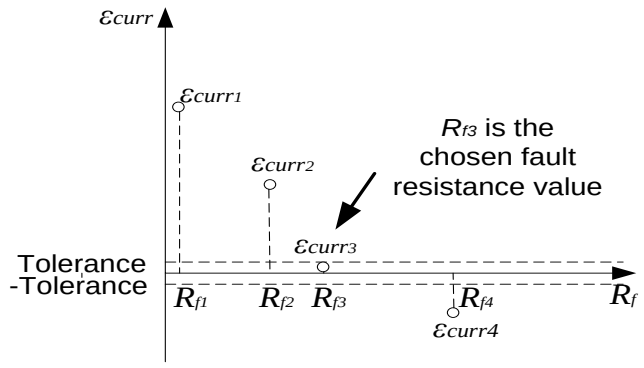

Figure 5.8 R_f estimation procedure

As described in [71], faults at different locations of the feeder may produce voltage sags with the same magnitude at the monitored places. This is due to the effect of the fault resistance. In order to differentiate the faults with varying fault resistance values, the monitored phase angle shifts and the voltage sag magnitudes are analyzed. For each fault candidate case, the voltage sag errors between the simulated case results and the measurements are calculated as:

$$\varepsilon_{FeederDAS} = \sum_{DAS=1}^{n_{DAS}} \left(\frac{\sqrt{\sum_{ph} (V_{sim\_DAS\_ph} - V_{mea\_DAS\_ph})^2}}{V_{base}} + \frac{\sqrt{\sum_{ph} (V_{ang\_sim\_DAS\_ph} - V_{ang\_mea\_DAS\_ph})^2}}{V_{ang\_base}} \right) \tag{5.18}$$

where, n_{DAS} represents the total feeder DAS number available with the event data, *ph* represents the phase A, B and C, $V_{sim\_DAS\_ph}$ and $V_{ang\_sim\_DAS\_ph}$ are the simulated voltage sag magnitude and angle of the phase *ph* at the corresponding DAS respectively, $V_{mea\_DAS\_ph}$ and $V_{ang\_mea\_DAS\_ph}$ are the measured voltage sag magnitude and angle of the phase *ph* at the corresponding DAS respectively, V_{base} of 7200 V and V_{ang_base} of 180° are used as the weights.

The fault candidate node with the smallest voltage sag error is pinpointed as the fault location.

5.4 Study of the real-world event cases

The event records collected from two actual fault cases are used to verify the proposed fault identification methodology. The actual locations of the two faults were found by the utility after patrolling the feeder. The actual locations are compared with the relocations obtained from the fault location identification method.

The first case is a single-phase-C-to-ground fault that occurred at 05:21 AM on July 24, 2013. Event data from DAS 5, DAS 4 and DAS 2 were available, and the feeder is divided into 4 zones accordingly. No event data from the PV DAS were available in this case. The reported fault location is 6.84 miles away from the substation in the feeder zone 2, downstream of one lateral fuse. Figure 5.9 shows the voltages and currents recorded during the faults at DAS 5. The data is plotted in AcSELerator Analytic Assistant.

The trained DT in CART and the implemented fuzzy logic based algorithm successfully identified the feeder zone and the fault type. Figure 5.10 shows the fault candidate nodes in each step of the fault identification process. 271 feeder nodes in the feeder zone 2

with Phase-C are recognized as the fault candidates. These 271 nodes are shown as the red dots in Figure 5.10 (a). After the fault resistance estimation process, the total numbers of the fault candidates are reduced to 153. The 153 nodes are shown in Figure 5.10 (b).

As shown in Figure 5.11, the voltage sag errors of the fault candidates are calculated and sorted. The with the smallest voltage sag error value of 0.2076 is observed at node 1566. Hence, node 1566 is identified as the fault location. The identified location is down-stream of the repaired lateral fuse on the same lateral. The estimation error is 0.32 miles. Figure 5.12 shows the identified fault location, as well as the true fault location marked with a star.

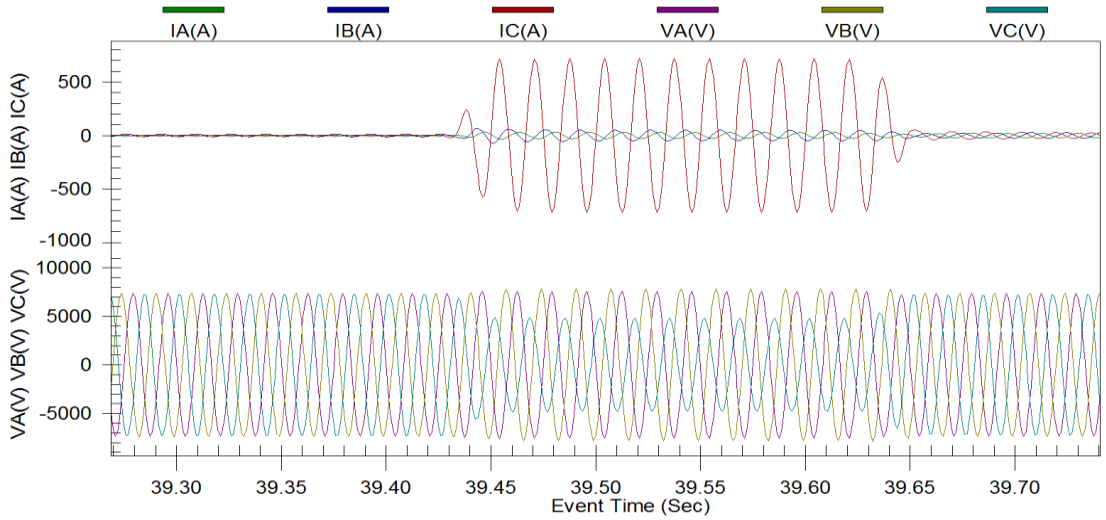

Figure 5.9 Recorded fault voltages and currents in the first fault case

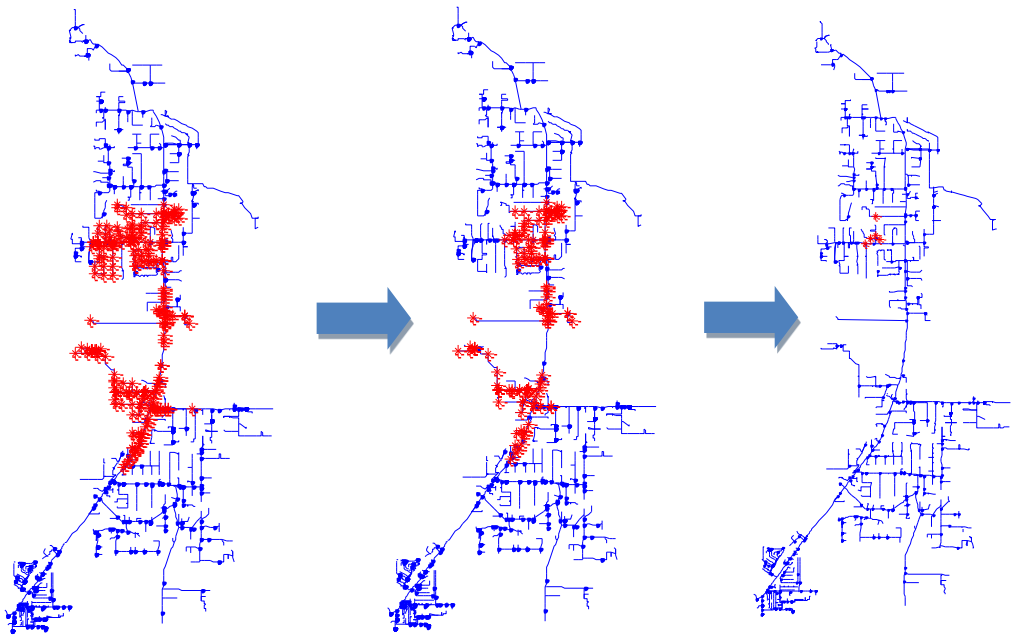

(a) (b) (c)

Figure 5.10 Fault candidate nodes in each step of the fault identification process (step a: identification of the fault zone with the fault type; step b: estimation of the fault resistance; step c: identification of the fault candidates within 5% of the smallest voltage sag error)

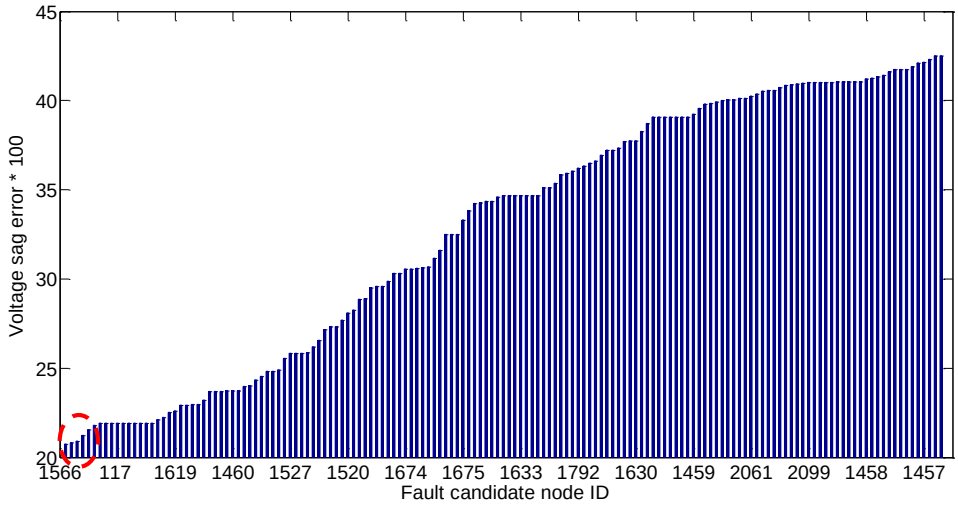

Figure 5.11 Voltage sag values obtained for all 153 fault candidate nodes

Additional fault candidate nodes with relatively small voltage sag errors (the nodes within 5% voltage sag error of the pinpointed node) are also chosen and analyzed. Based on this, 5 fault candidates are chosen and plotted as shown in Figure 5.10 (c). As illustrated in Figure 5.12, these 5 fault candidates fall into 2 sections. Table 5.6 lists the electrical distance of each section to the true fault location, as well as the geometric distance from each section to the substation.

The percentage error in the geometric distance from the estimated fault location to the substation is calculated as

$$Error_{dis}(\%) = \frac{L_{est} - L_{true}}{L_{true}} \times 100\% \tag{5.19}$$

where, L_{est} and L_{true} represent respectively the geometric distance of the estimated fault location and the true fault location to the substation.

As illustrated from Table 5.6, the largest electrical distance error is 0.97 mile as seen from section 2. However, the two sections are all within 3% error of the geometric distance to the substation compared to the true fault location. This indicates that the proposed fault identification method successfully narrows down the potential fault candidate area.

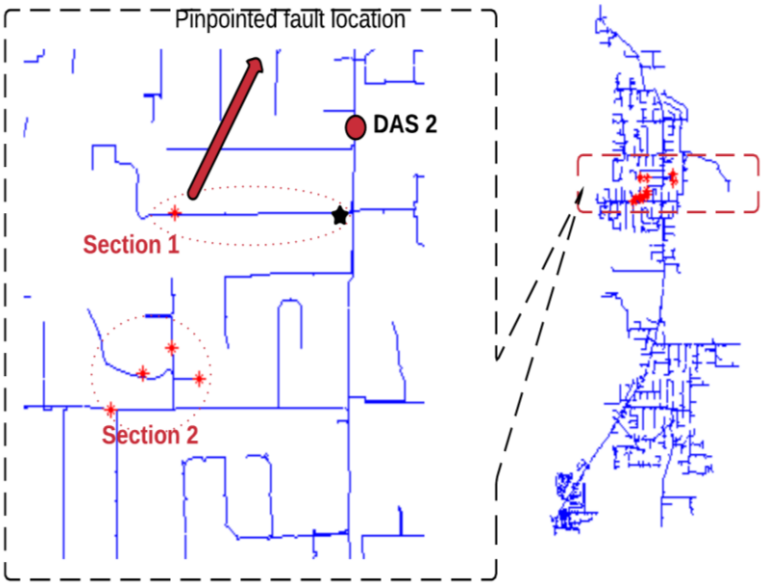

Figure 5.12 Fault candidates with relatively small voltage sag values

Table 5.6 Sections for the fault candidate nodes

	Electrical distance to the true fault location (mile)	Geometric distance to the substation (mile)	$Error_{dis}$
Section 1	0.32	7.03	2.78%
Section 2	0.97	6.73	1.54%

The second fault case is a single-phase-B-to-ground fault that occurred at 13:12 PM on March 21, 2014. Event data from DAS 5, DAS 4 and DAS 2, as well as from 5 small PV DAS were available in this case. Figure 5.13 shows the profiles of the voltages and currents during the faults at DAS 5. The data is plotted in AcSELerator Analytic Assistant. The fault was reported to occur at a distance of 7.67 mile from the substation.

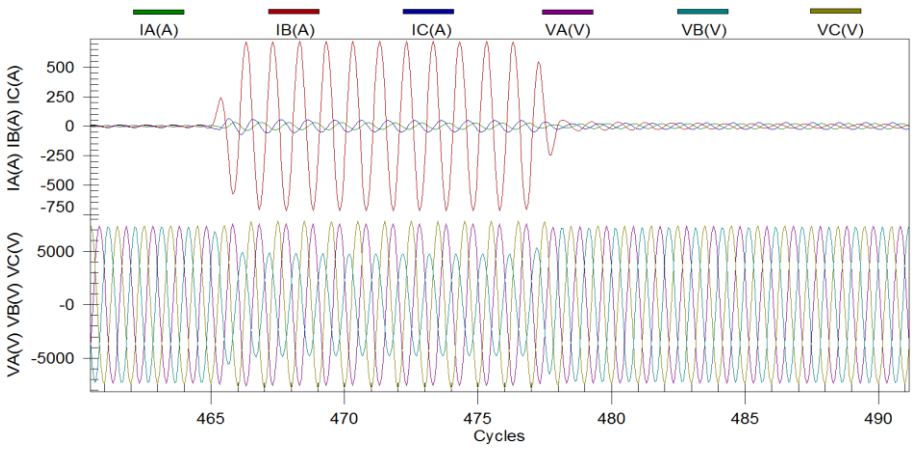

Figure 5.13 Recorded fault voltages and currents in the second fault case

The fault zone is identified by the DT trained in CART, and the fault type is identified by the fuzzy logic based algorithm. Figure 5.14 shows the fault candidate nodes in each step of the fault identification process. As shown in Figure 5.14 (a), 205 fault candidates with phase-B are analyzed. After the fault resistance estimation process, the total numbers of the fault candidates are reduced to 25. The 25 nodes are shown in Figure 5.14 (b).

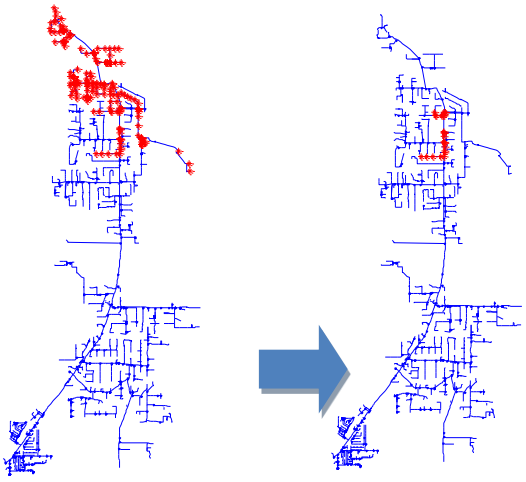

(a) (b)

Figure 5.14 Fault candidate nodes in each step of the fault identification process (step a: identification of the fault zone with the fault type; step b: estimation of the fault resistance)

Figure 5.15 shows the estimated fault location using feeder DAS and PV DAS event data. With only the event data from the feeder DAS, the preliminary estimated fault location (node 510) is 0.002 mile away from the true fault location (the true location is marked as a star shown in Figure 5.15). The voltage sag errors are plotted in Figure 5.16. The pinpointed fault location is very close to the actual one. However, the voltage sag errors calculated for the 25 fault candidate nodes shown in Figure 5.14 (b) are within 5% of the smallest value. Hence, these 25 fault candidate nodes need to be analyzed as well.

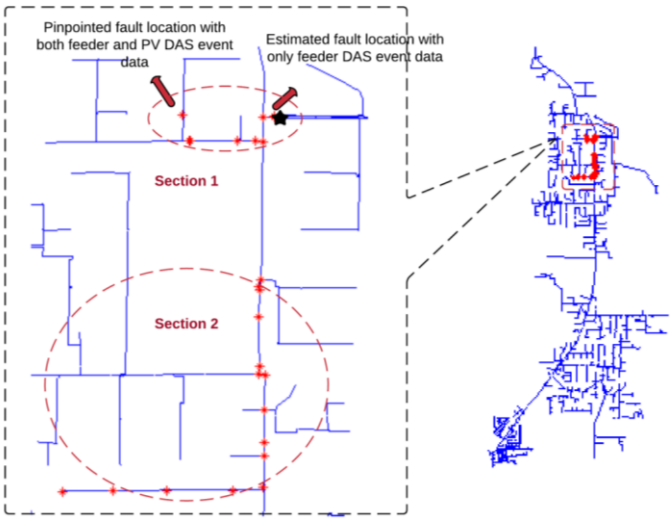

Figure 5.15 Estimated fault location using feeder DAS and PV DAS event data

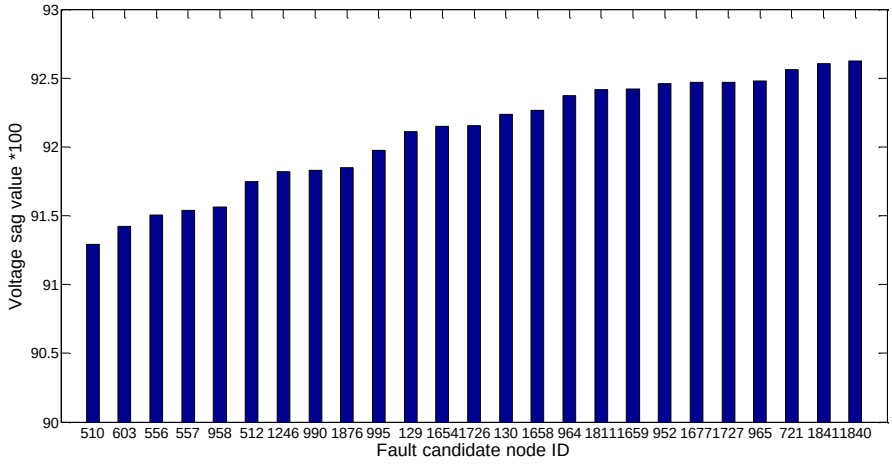

Figure 5.16 Voltage sag values obtained with feeder DAS event data

To obtain more accurate fault identification with narrowed fault area, the simulated voltage sag values at the 5 PV DAS are compared with the measurements, as expressed in (5.20).

$$\varepsilon_{PVDAS} = \sum_{PVDAS=1}^{n} \frac{\sqrt{(V_{sim\_PVDAS} - V_{mea\_PVDAS})^2}}{V_{base}} \tag{5.20}$$

where, n represents the total PV DAS number available with the event data, V_{sim_PVDAS} and V_{mea_PVDAS} are the simulated and measured voltage sag magnitude at the corresponding PV DAS respectively, and V_{base} of 120 V is used as the weight.

A more accurate estimate of the fault location can be obtained if more PV DAS measurements are available, especially from PV DAS located near the actual fault.

With voltage sag errors from both the feeder DAS and the PV DAS considered, the total voltage sag error value is given by

$$\varepsilon_{total} = \varepsilon_{FeederDAS} + \varepsilon_{PVDAS} \tag{5.21}$$

The sorted total voltage sag errors of the fault candidates are shown in Figure 5.17.

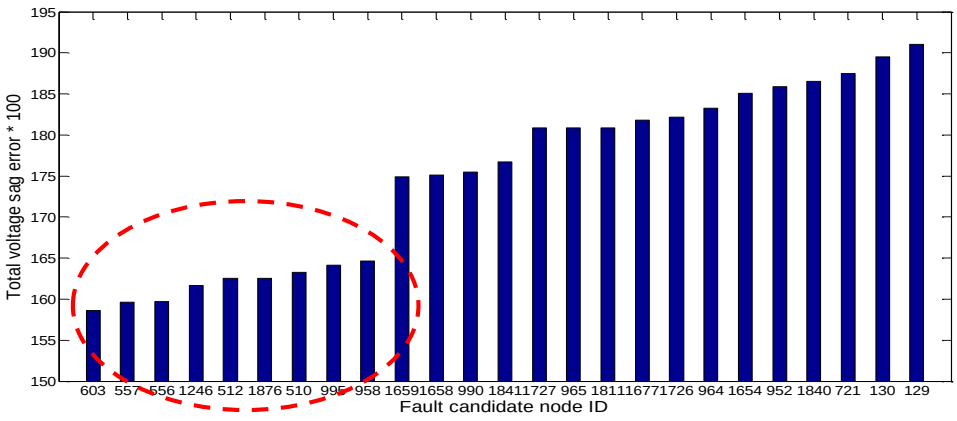

Figure 5.17 Voltage sag values obtained with both feeder and PV DAS event data

The fault location is pinpointed at node 603, which has the smallest total voltage sag error. The pinpointed location is 0.15 mile away from the true fault location, as seen from

Figure 5.15. The fault candidates with the total voltage sag errors within 5% of the smallest value are all inside section 1 shown in Figure 5.15. Section 1 is within 0.82 miles of the true fault location. It should be noted that with PV DAS event data included, the pinpointed fault location is farther away from the true location compared to the estimated location with only feeder DAS event data used. However, the fault location area with small voltage sag error values is narrowed down.

CHAPTER 6: CONCLUSIONS

This work has provided an extensive study of distribution systems with high penetration of PV generation. The main topics covered in this work are as follows:

- Detailed modeling and verification of a distribution feeder
- Steady state analysis of the impact of PV on feeder voltages
- Dynamic modeling and analysis of the PV inverters in unbalanced large distribution systems
- Protection coordination analysis of the PV impacts with different connection types of the interconnection transformer
- Fault location identification with and without PV systems installed in the distribution feeder.

Developing a detailed model of a distribution feeder is the first step towards any analysis that needs to be performed on a distribution system. Accordingly, this work presented an automated procedure to develop a detailed model for an actual test feeder. The test feeder has been modeled in both CYMDIST and OpenDSS. The model was developed based on the complete GIS data on major feeder equipment and conductor segments, and load and PV data at a fine resolution through AMI and DAS. A zone-division method was used, which enabled the development of an accurate feeder model. The accuracy of the model was verified by comparing simulation results with the field measurements. The RMS error between the simulated and measured voltages and currents at DAS along the feeder was found to be less than 1.5%. The main merit of the modeling work lies in the fact that an actual 'real-life' feeder data was used. Hence, the modeling approach tackles many

practical issues that may not arise while using an academic test system. The modeling and verification methods described in this work can therefore be readily used to model other feeders or larger distribution systems.

To perform a steady state analysis of the impact of high penetration of PV on voltage profiles, snapshot and time-series analyses were conducted. These simulations were performed based on the historical load data and PV generation data provided by the utility. The results of the study indicated that the maximum PV penetration level generally decreases when the average distance from the PV systems to the feeder head increases. In addition, recommendations were proposed on the settings of the PV inverters and the LTC transformers. It was found that under high penetration of PV, the PV inverters are able to maintain the feeder voltage profile within the ANSI limits, if they are allowed to absorb reactive power. The PV inverters can keep the feeder voltages within the recommended limits when they operate at a 0.9 leading power factor, with PV generation as high as 50% above the base hosting capacity. It is therefore recommended that the residential inverters have a kVA rating of at least 1.11 times the maximum kW rating. In addition, the study suggested that a significant increase in PV hosting capacity could be obtained by appropriate tap selections of LTC. The LTC tap selection is done based on the variation of loads and irradiance.

In order to perform dynamic analysis in large unbalanced distribution systems, this work proposes a DAE based dynamic modeling and analysis method. The analytical model of the PV inverter is created based on the single-phase *dq* transformation. The PV model is written into a DLL, and interfaced with the network model built in OpenDSS. At each time step of the dynamic simulation, the differential equations of the PV model inside the

DLL are solved, and the network algebraic equations are solved in OpenDSS. The reference frame transformation is executed during the electrical quantity exchange between the DLL containing the PV inverter model and OpenDSS. The proposed modeling method has been verified by performing detailed three-phase simulation in PLECS. In addition, the current controls, anti-islanding schemes, and droop controls of the PV inverter models are tested in large unbalanced distribution systems in both islanded and grid connected mode. The proposed method extends the capability of OpenDSS to perform dynamic studies for unbalanced distribution systems. This approach is expected to help in the design and testing of CIGs in distribution systems.

A thorough protection coordination analysis of the impact of PV systems on distribution systems was presented in this work. This research proposed a methodology to verify and design the protective device settings under different penetration levels of PV systems. The impact of the connection types of the PV interconnection transformers were also explored in-depth during the protection coordination analysis. All possible protection coordination cases in the feeder were studied. The cases studied included coordination of fuse-fuse, recloser-fuse, relay-fuse and relay-recloser, based on the definition of the protection zones. An optimization problem was formulated to find the appropriate settings of the protection devices. The study included thousands of protection coordination cases found under different penetration levels of the PV systems. The research findings indicated that, when the PV interconnection transformers are connected as grounded wye/delta, the relay/recloser settings need to be changed. The change is significant when the PV penetration level increases in the distribution system. Additional reclosers may need to be installed down-

stream of the original reclosers due to the reduced sensitivity of the relay/recloser. However, when the PV interconnection transformers are connected as delta/delta, the settings of the relay/recloser are not affected significantly as the PV penetration levels increase. In this case, the settings for the relay/recloser can be set as the value calculated with the largest possible PV rating in the feeder. The presented methodology provided a reference for designing proper settings for distribution level protection devices in the presence of high penetration of PV. The analysis was done on an actual feeder and it highlighted some practical problems with protection system analysis. Such issues may not be encountered while studying academic test systems. The analysis techniques presented here can be readily extended in studying real, large distribution systems.

This research also proposed a fuzzy logic and DT based fault location identification process. The method proposed here utilizes various open-source and commercial analysis tools like OpenDSS, MATLAB, CART. The impact of PV fault current contribution on the fault identification process was eliminated using fuzzy logic and DT. Two actual fault cases with the event data recorded were used to examine the effectiveness of the fault identification process. The proposed method pinpointed the fault location within 0.32 mile and 0.002 mile from the respective true fault locations, in both the cases. In addition, the proposed method substantially narrows down the area of the potential fault location. With the use of this method, utility operators can effectively track down fault locations in the distribution feeder, thereby enabling faster restoration of faulted lines. Incorporating the proposed fault location identification method is expected to increase the reliability of the distribution system significantly.

REFERENCES

[1] Philip P. Barker, "Determining the impact of distributed generation on power systems: part 1-radial distribution systems," *Power Engineering Society Summer Meeting*, vol. 3, pp. 1645-1656, July 2000.

[2] Lisa Schwartz, "Distributed generation in Oregon: overview, regulatory barriers and recommendations," Oregon Public Utility Commission Report, February 2005.

[3] Tales M. de Britto, "Distributed generation impacts on the coordination of protection systems in distribution networks," *Transmission and Distribution Conference and Exposition: Latin America*, pp. 623-628, November 2004.

[4] B. Hussain, "Impact studies of distributed generation on power quality and protection setup of an existing distribution network," *Power Electronics Electrical Drives Automation and Motion*, pp. 1243-1246, June 2010.

[5] R. A. Walling, "Summary of distributed resources impact on power delivery systems," *IEEE Transactions on Power Delivery*, vol. 23, No. 3, pp. 1636-1644, July 2008.

[6] Eurelectric, "Active distribution system management—a key tool for the smooth integration of distributed generation," *Eurelectric*, Feb. 2013

[7] F. A. Viawan and D. Karlsson, "Voltage and reactive power control in system with synchronous machine-based distributed generation," *IEEE Trans. Power Del.*, vol. 23, no. 2, pp. 1079-1087, Apr. 2008.

[8] M. Venmathi, J. Vargese, L. Ramesh and E. S. Percis, "Impact of grid connected distributed generation on voltage sag," *Sustainable Energy and Intelligent Systems*, Chennai, pp. 91-96, 2011.

[9] L. Kojovic, "Impact DG on voltage regulation," *IEEE Power Engineering Society Summer Meeting*, vol. 1, pp. 97-102, 2001.

[10] L. F. Ochoa and G. P. Harrison, "Minimizing energy losses: optimal accommodation and smart operation of renewable distributed generation," *IEEE Transactions on Power Systems*, vol. 26, no. 1, pp. 198-205, Feb. 2011.

[11] T. Ackermann and V. Knyazkin, "Interaction between distributed generation and the distribution network: operation aspects," *IEEE Transmission and Distribution Conference and Exhibition*, vol. 2, pp. 1357-1362, 2002.

[12] G.C. Cornfield, "Definition and measurement of voltage flicker in lighting," *IEE Colloquium on Electronics in Power Systems Measurement*, pp. 1-4, Aug. 2002.

[13] J. Sun, D. Czarkowski and Z. Zabar, "Voltage flicker mitigation using PWM-based distribution STATCOM," *IEEE Power Engineering Society Summer Meeting*, vol.1, pp. 616-621, 2002.

[14] M. I. Marei, T. K. Abdel-Galil, E. F. El-Saadany and M. M. A. Salama, "Hilbert transform based control algorithm of the DG interface for voltage flicker mitigation," *IEEE Transactions on Power Delivery*, vol. 20, no. 2, pp. 1129-1133, April 2005.

[15] A. Elnady and M. M. A. Salama, "Unified approach for mitigating voltage sag and voltage flicker using the DSTATCOM," *IEEE Transactions on Power Delivery*, vol. 20, no. 2, pp. 992-1000, April 2005.

[16] Zaneta, B. Anton, M. Mucha, "Harmonic distortion produced by synchronous generator in thermal - power plant," *Proceedings of the 6th WSEAS International Conference on Power Systems*, Sept. 2006.

[17] Y. W. Li and J. He, "Distribution system harmonic compensation methods: an overview of DG-interfacing inverters," IEEE Industrial Electronics Magazine, vol. 8, no. 4, pp. 18-31, Dec. 2014.

[18] E. Vasanasong and E. D. Spooner, "The effect of net harmonic currents produced by numbers of the sydney olympic village's PV systems on the power quality of local electrical network," *International Conference on Power System Technology*, vol. 2, pp. 1001-1006, 2002.

[19] V. Khadkikar, R. K. Varma, R. Seethapathy, A. Chandra and H. Zeineldin, "Impact of distributed generation penetration on grid current harmonics considering non-linear loads," *Power Electronics for Distributed Generation Systems*, pp. 608-614, 2012.

[20] IEEE, “IEEE Recommended Practices and Requirements for Harmonic Control in Electrical Power Systems," IEEE Standard 519-1992, pp. 1-112, April 1993.

[21] S. Boljevic and M. F. Conlon, "The contribution to distribution network short-circuit current level from the connection of distributed generation," *43rd International Universities Power Engineering Conference*, pp. 1-6, 2008.

[22] S. Boljevic and M. F. Conlon, "Fault current level issues for urban distribution network with high penetration of distributed generation," *6th International Conference on the European Energy Market*, pp. 1-6, 2009.

[23] A. Sinclair, D. Finney, D. Martin and P. Sharma, "Distance protection in distribution systems: how It assists with integrating distributed resources," *IEEE Transactions on Industry Applications*, vol. 50, no. 3, pp. 2186-2196, May 2014.

[24] F. Coffele, C. Booth, A. Dyśko and G. Burt, "Quantitative analysis of network protection blinding for systems incorporating distributed generation," *IET Generation, Transmission & Distribution*, vol. 6, no. 12, pp. 1218-1224, December 2012.

[25] Seongchul Kwon, "Evaluation of protection coordination with distributed generation in distribution networks," *Developments in Power System Protection, 10th IET International Conference*, pp. 1-5, March 2010.

[26] Dao Van Tu and S. Chaitusaney, "Relay sensitivity approach for maximizing distributed generation," *TENCON 2011-2011 IEEE Region 10 Conference*, pp. 1010-1014, November 2011.

[27] Dao Van Tu and S. Chaitusaney, "Maintaining the reach of protective devices in distribution system with penetration of distributed generation," *Electrical Engineering/Electronics, Computer, Telecommunications and Information Technology*, pp. 696- 699, May 2011.

[28] Andrew T. Moore, "Distributed generation (DG) protection overview," University of Western Ontario Report, May 2008.

[29] K Kauhaniemi, L. Kumpulainen, "Impact of distributed generation on the protection of distribution networks," *Developments in Power System Protection, Eighth IEE International Conference*, vol. 1, pp. 315-318, April 2004.

[30] F T Dai, "Impacts of distributed generation on protection and autoreclosing of distribution networks," Developments in Power System Protection. Managing the Change, *10th IET International Conference*, pp. 1-5, March 2010.

[31] Hamed B. Funmilayo, James A. Silva, Karen L. Butler-Purry, "Overcurrent protection for the IEEE 34-Node radial test feeder," *IEEE Transactions on Power Delivery*, vol. 27, no. 2, pp. 459-468, April 2012.

[32] H. H. Zeineldin, Hebatallah M. Sharaf, Doaa K. Ibrahim, Essam El-Din Abou El-Zahab, "Optimal protection coordination for meshed distribution systems with DG using dual setting directional over-current relays," *IEEE Transactions on Smart Grid*, vol. 6, no. 1, pp. 115-123, Jan. 2015.

[33] R. A. F. Pereira, L. G. W. da Silva, M. Kezunovic, J. R. S. Mantovani, "Improved fault location on distribution feeders based on matching during-fault voltage sags," *IEEE Transactions on Power Delivery*, vol. 24, no. 2, pp. 852-862, April 2009.

[34] CYME by Cooper power systems, available at: http://www.cyme.com/software/cymdist/, 2013.

[35] R. F. Arritt and R. Dugan, “Distribution system analysis and the future smart grid,” *IEEE Transactions on Industry Applications*, vol. 47, pp. 2343-2350, Nov. 2011.

[36] CART by Salford systems, available at: http://www.salford-systems.com/cart.php.

[37] C. L. Masters, "Voltage rise: the big issue when connecting embedded generation to long 11 kV overhead lines," *Power Engineering Journal*, vol. 16, no. 1, pp. 5-12, Feb. 2002.

[38] L. M. Cipcigan, P. C. Taylor, "Investigation of the reverse power flow requirements of high penetrations of small-scale embedded generation," *Renewable Power Generation*, IET, vol. 1, no. 3, pp. 160-166, Sept. 2007.

[39] D. Caples, S. Boljevic and M. F. Conlon, "Impact of distributed generation on voltage profile in 38 kV distribution system," *Proc. 8th Int. Conf. Eur. Energy Market*, pp. 532-536, May 2011.

[40] C. H. Lin, W. L. Hsieh, C. S. Chen, C. T. Hsu and T. T. Ku, "Optimization of photovoltaic penetration in distribution systems considering annual duration curve of solar irradiation," *IEEE Trans. Power Syst.*, vol. 27, no. 2, pp. 1090-1097, May 2012.

[41] P. M. S. Carvalho, P. F. Corriea and L. A. F. Ferriera, "Distributed reactive power generation control for voltage rise mitigation in distribution networks," *IEEE Trans. Power Syst.*, vol. 23, no. 2, pp. 766 -772, May 2008.

[42] X. Liu, A. Aichhorn, L. Liu and H. Li, "Coordinated control of distributed energy storage system with tap changer transformers for voltage rise mitigation under high photovoltaic penetration," *IEEE Trans. Smart Grid*, vol. 3, no. 2, pp. 897-906, 2012.

[43] Y. Liu, J. Bebic, B. Kroposki, J. de Bedout and W. Ren, "Distribution system voltage performance analysis for high-penetration PV," *Proc. IEEE Energy 2030 Conf.*, pp. 1-8, Nov. 2008.

[44] V. Ramachandran, S. K. Solanki, J. Solanki, "Steady state analysis of three phase unbalanced distribution systems with interconnection of photovoltaic cells," *Power Systems Conference and Exposition (PSCE)*, pp. 1-7, March 2011.

[45] J. E. Quiroz and C. P. Cameron, "Technical analysis of prospective photovoltaic systems in Utah," Sandia National Laboratories, SAND2012-1366, Feb. 2012.

[46] A. Hoke, R. Butler, J. Hambrick, B. Kroposki, "Steady-state analysis of maximum photovoltaic penetration levels on typical distribution feeders," *IEEE Transactions on Sustainable Energy*, vol. 4, no. 2, pp. 350-357, April 2013.

[47] Tony Seegers, Ken Bert, "Impact of distributed resources on distribution relay protection," Line Protection Subcommittee of the Power System Relay Committee of the IEEE Power Engineering Society Report, August 2004.

[48] IEEE, "IEEE recommended practice for protection and coordination of industrial and commercial power systems," ANSI/IEEE Standard 242-2001, 2001.

[49] N. Nimpitiwan, G. T. Heydt, J. Blevins, A. B. Cummings, "Potential economic impact of fault currents contributed by distributed generation," *IEEE Power Engineering Society General Meeting*, vol. 1, pp. 678-683, June 2005.

[50] A. A. Girgis and S. M. Brahma, "Effect of distributed generation on protective device coordination in distribution system," *Proc. IEEE Large Eng. Syst. Conf.*, pp. 115-119, July 2001.

[51] S. M. Brahma and A. A. Girgis, "Microprocessor-based reclosing to coordinate fuse and recloser in a system with high penetration of distributed generation," *Proc. IEEE Power Eng. Soc. Winter Meeting*, vol. 1, pp. 453 -458, 2002.

[52] S. M. Brahma and A. A. Girgis, "Development of adaptive protection scheme for distribution systems with high penetration of distributed generation," *IEEE Transactions on Power Delivery*, vol. 19, no. 1, pp. 56-63, Jan. 2004.

[53] S. Chaitusaney and A. Yokoyama, "Reliability analysis of distribution system with distributed generation considering loss of protection coordination," *Proc. Int. Conf. Probabilistic Meth. Appl. Power Syst.*, pp. 1-8, June 2006.

[54] A. F. Naiem, Y. Hegazy, A. Y. Abdelaziz, M. A. Elsharkawy, "A Classification technique for recloser-fuse coordination in distribution systems with distributed generation," *IEEE Transactions on Power Delivery*, vol. 27, no. 1, pp. 176-185, Jan. 2012.

[55] R. K. Aggarwal, Y. Aslan and A. T. Johns, "New concept in fault location for overhead distribution systems using superimposed components," *Proc. Inst. Elect. Eng., Gen., Transm., Distrib.*, vol. 144, no. 3, pp. 309 -316, May 1997.

[56] R. K. Aggarwal, Y. Aslan and A. T. Johns, "An interactive approach to fault location on overhead distribution lines with load taps," *Developments in Power System Protection, Sixth International Conference*, pp. 184 -187, Mar. 1997.

[57] J. J. Mora, G. Carrillo and L. Perez, "Fault location in power distribution systems using ANFIS nets and current patterns," *Proc. IEEE Power Eng. Soc. Transmission and Distribution Conf. Expo. Latin America*, pp. 1-7, Aug. 2006.

[58] J. Mora-Florez, V. Barrera-Nuez and G. Carrillo-Caicedo, "Fault location in power distribution systems using a learning algorithm for multivariable data analysis," *IEEE Transactions on Power Delivery*, vol. 22, no. 3, pp. 1715-1721, July 2007.

[59] Y. Dong, C. Zheng, M. Kezunovic, "Enhancing accuracy while reducing computation complexity for voltage-sag-based distribution fault location," *IEEE Transactions on Power Delivery*, vol. 28, no. 2, pp. 1202-1212, April 2013.

[60] D. Novosel, D. Hart and J. Myllymaki, "System for locating faults and estimating fault resistance in distribution networks with tapped loads," Patent US5839093 A, Nov. 1998.

[61] A. A. Girgis, C. M. Fallon and D. L. Lubkeman, "A fault location technique for rural distribution feeders," *IEEE Trans. Ind. Appl.*, vol. 29, no. 6, pp. 1170-1175, Nov. 1993.

[62] K. Srinivasan and A. St-Jacques, "A new fault location algorithm for radial transmission lines with loads," *IEEE Transactions on Power Delivery*, vol. 18, no. 3, pp. 1679-1682, 2003.

[63] Yanfeng Gong, A. Guzman, "Integrated fault location system for power distribution feeders," *IEEE Transactions on Industry Applications*, vol. 49, no. 3, pp. 1071-1078, May-June 2013.

[64] S. Kulkarni, N. Karnik, S. Das, S. Santoso, "Fault location using impedance-based algorithms on non-homogeneous feeders," *IEEE Power and Energy Society General Meeting*, pp. 1-6, July 2011.

[65] N. Karnik, S. Das, S. Kulkarni, S. Santoso, "Effect of load current on fault location estimates of impedance-based methods," *IEEE Power and Energy Society General Meeting*, pp. 1-6, July 2011.

[66] S. Das, S. Kulkarni, N. Karnik, S. Santoso, "Distribution fault location using short-circuit fault current profile approach," *IEEE Power and Energy Society General Meeting*, pp. 1-7, July 2011.

[67] S. Das, N. Karnik, S. Santoso, "Distribution fault-locating algorithms using current only," *IEEE Transactions on Power Delivery*, vol. 27, no. 3, pp. 1144-1153, July 2012.

[68] Z. Q. Bo, G. Weller and M. A. Redfern, "Accurate fault location technique for distribution system using fault-generated high-frequency transient voltage signals," *Proc. Inst. Elect. Eng., Gen. Transm. Distrib.*, vol. 146, no. 1, 1999.

[69] D. W. P. Thomas, R. J. O. Carvalho and E. T. Pereira, "Fault location in distribution systems on traveling waves," *IEEE Bologna Power Tech Conf.*, vol. 2, June 2003.

[70] H. Nouri, C. Wang and T. Davie, "An accurate fault location technique for distribution lines with tapped loads using wavelet transform," *Proc. IEEE Power Tech, vol. 3*, pp. 1-4, Sept. 2001.

[71] S. Lotfifard, M. Kezunovic, M. J. Mousavi, "Voltage sag data utilization for distribution fault location," *IEEE Transactions on Power Delivery*, vol. 26, no. 2, pp. 1239-1246, April 2011.

[72] Po-Chen Chen, V. Malbasa, Yimai Dong, M. Kezunovic, "Sensitivity analysis of voltage sag based fault location with distributed generation," *IEEE Transactions on Smart Grid*, vol. 6, no. 4, pp. 2098-2106, July 2015.

[73] F. C. L. Trindade, W. Freitas, J. C. M. Vieira, "Fault location in distribution systems based on smart feeder meters," *IEEE Transactions on Power Delivery*, vol. 29, no. 1, pp. 251-260, Feb. 2014.

[74] S. M. Brahma, "Fault location in power distribution system with penetration of distributed generation," *IEEE Transactions on Power Delivery*, vol. 26, no. 3, pp. 1545-1553, July 2011.

[75] P. M. Anderson, "Power system protection," IEEE Press, New York, 1999.

[76] Larry Sherwood, "U.S. solar market insight report - 2012 year in review," GTM Research and Solar Energy Industries Association, 2013, available at: http://www.seia.org/research-resources/us-solar-market-insight-2012-year-review

[77] Dave Narang, Josh Hambrick, "High penetration PV deployment in the Arizona Public Service system," *Photovoltaic Specialists Conference*, June 2011.

[78] Joshua Hambrick, David Narang, "High penetration PV deployment in the Arizona Public Service system, phase 1 update," *Photovoltaic Specialists Conference*, June 2012.

[79] IEEE, "American national standard for electric power systems and equipment -voltage ratings (60 Hz)," ANSI/IEEE Standard C84. 1-2011, 2011.

[80] R. C. Dugan, M. F. McGranaghan, S. Santoso and H. W. Beaty, "Circuit electrical power systems quality," McGraw-Hill Education, New York, 2003.

[81] R.E. Brown, "Electric power distribution reliability," CRC Press, 2009.

[82] P. M. Anderson, "Power system protection," IEEE Press, New York, 1999.

[83] C. A. O' Meally, J. Burke, "A fuse-blow scheme," *Industry Applications Magazine, IEEE*, vol. 16, pp. 37-42, 2010.

[84] IEEE, "IEEE recommended practice for protection and coordination of industrial and commercial power systems," ANSI/IEEE Standard 242-2001, 2001.

[85] J. Keller, B. Kroposki, "Understanding fault characteristics of inverter-based distributed energy resources," National Renewable Energy Laboratory, TP-550-46698, Jan. 2010.

[86] IEEE, "IEEE standard inverse-time characteristic equations for over-current relays," IEEE Standard C37, 112-1996, 1996.

[87] C. A. Warren, "Distribution reliability: what is it?" *Industry Applications Magazine, IEEE*, vol. 2, no. 4, pp. 32-37, Jul. 1996.

[88] S. R. Samantaray, "Decision tree-based fault zone identification and fault classification in flexible AC transmissions-based transmission line," *Generation, Transmission & Distribution, IET*, vol. 3, no. 5, pp. 425-436, May 2009.

[89] L. Breiman, J. H. Friedman, R. A. Olshen, C. J. Stone, "Classification and regression trees," Chapman & Hall Wadsworth, New York, 1984.

[90] D. Landgrebe, "A survey of decision tree classifier methodology," *IEEE Transactions on Systems, Man and Cybernetics*, vol. 21, no. 3, pp. 660-674, May 1991.

[91] Yoon-Sung Cho, Chul-Kyun Lee, Gilsoo Jang, Heung Jae Lee, "An innovative decaying DC component estimation algorithm for digital relaying," *IEEE Transactions on Power Delivery*, vol. 24, no. 1, pp. 73-78, Jan. 2009.

[92] B. Das, "Fuzzy logic-based fault-type identification in unbalanced radial power distribution system," *IEEE Transactions on Power Delivery*, vol. 21, no. 1, pp. 278-285, Jan. 2006.

[93] Sukumar M. Brahma, Adly A. Girgis, "Development of adaptive protection scheme for distribution systems with high penetration of distributed generation," *IEEE Transactions on Power Delivery*, vol. 19, no. 1, pp. 56-63, Jan. 2004.

[94] Sukumar M. Brahma, "Fault location in power distribution system with penetration of distributed generation," *IEEE Transactions on Power Delivery*, vol. 26, no. 3, pp. 1545-1553, July 2011.

[95] Cyndi Newman, David J. Narang, "High penetration of photovoltaic generation study – Flagstaff community power," Arizona Public Service Company, Sept. 2011, available at:
http://www.osti.gov/scitech/servlets/purl/1025589/

[96] PLECS, electrical engineering software, available at:
http://www.plexim.com/

[97] Manitoba HVDC Research Centre, PSCAD Software, 2014, available at:
https://hvdc.ca/pscad

[98] OpenDSS, distribution system simulator, available at:
https://sourceforge.net/projects/electricdss/

[99] GridLab-D, power distribution system simulation and analysis tool, available at:
http://www.gridlabd.org/

[100] S. Mishra, D. Ramasubramanian, and P. Sekhar, "A seamless control methodology for a grid connected and isolated PV-diesel microgrid," *IEEE Trans. Power Syst.*, vol. 28, no. 4, pp. 4393-4404, Nov 2013.

[101] R. de Almeida and J. Pec¸as Lopes, “Participation of doubly fed induction wind generators in system frequency regulation,” *IEEE Trans. Power Syst*., vol. 22, no. 3, pp. 944-950, Aug. 2007.

[102] J. F. Conroy and R. Watson, “Frequency response capability of full converter wind turbine generators in comparison to conventional generation,” *IEEE Trans. Power Syst*., vol. 23, no. 2, pp. 649-656, May 2008.

[103] G. C. Kryonidis et al., "A simulation tool for extended distribution grids with controlled distributed generation," *IEEE Power Tech.*, pp. 1-6, 2015.

[104] M. A. Elizondo, F. K. Tuffner and K. P. Schneider, "Three-Phase unbalanced transient dynamics and powerflow for modeling distribution systems with synchronous machines," *IEEE Transactions on Power Systems*, vol. 31, no. 1, pp. 105-115, Jan. 2016.

[105] T. E. McDermott, "Modeling PV for unbalanced, dynamic and quasistatic distribution system analysis," *IEEE Power and Energy Society General Meeting*, pp. 1-3, 2011.

[106] J. W. Smith, R. Dugan, M. Rylander and T. Key, "Advanced distribution planning tools for high penetration PV deployment," *IEEE Power and Energy Society General Meeting*, pp. 1-7, 2012.

[107] R. C. Dugan and T. E. McDermott, "An open source platform for collaborating on smart grid research," *IEEE Power and Energy Society General Meeting*, pp. 1-7, 2011.

[108] Delphi Embarcadero Delphi 10, available at:
http://www.embarcadero.com/products/delphi

[109] J. M. Cushing, "Differential equations: an applied approach," Prentice Hall, 2004.

[110] IEEE PES Distribution System Analysis Subcommittee, Distribution Test Feeders, 2013, available at:
http://ewh.ieee.org/soc/pes/dsacom/testfeeders/index.html

[111] P. Rodriguez, J. Pou, J. Bergas, J. I. Candela, R. P. Burgos and D. Boroyevich, "Decoupled double synchronous reference frame PLL for power converters control," *IEEE Transactions on Power Electronics*, vol. 22, no. 2, pp. 584-592, March 2007.

[112] P. Rodriguez, A. Lunar, R. Teodorescu, F. Iov and F. Blaabjerg, "Fault ride-through capability implementation in wind turbine converters using a decoupled double synchronous reference frame PLL," *Power Electronics and Applications*, pp. 1-10, 2007.

[113] V. John, Zhihong Ye and A. Kolwalkar, "Investigation of anti-islanding protection of power converter based distributed generators using frequency domain analysis," *IEEE Transactions on Power Electronics*, vol. 19, no. 5, pp. 1177-1183, Sept. 2004.

[114] Z. Ye, R. Walling, L. Garces, R. Zhou, L. Li, T. Wang, "Study and development of anti-islanding control for grid-connected inverters," NREL/SR-560-36243. National Renewable Energy Laboratory, May 2004.

[115] P. Piagi and R. H. Lasseter, "Autonomous control of microgrids," *IEEE Power Engineering Society General Meeting*, pp. 8, 2006.

[116] R. H. Lasseter and P. Paigi, "Microgrid: a conceptual solution," *Power Electronics Specialists Conference*, vol. 6, pp. 4285-4290, June 2004.

[117] N. Pogaku, M. Prodanovic and T. C. Green, "Modeling, analysis and testing of autonomous operation of an inverter-based microgrid," *IEEE Transactions on Power Electronics*, vol. 22, no. 2, pp. 613-625, March 2007.

[118] R. Majumder, B. Chaudhuri, A. Ghosh, R. Majumder, G. Ledwich and F. Zare, "Improvement of stability and load sharing in an autonomous microgrid using supplementary droop control loop," *IEEE Transactions on Power Systems*, vol. 25, no. 2, pp. 796-808, May 2010.

[119] PSLF, positive sequence load flow software, available at: http://www.geenergyconsulting.com/practice-area/software-products/pslf

[120] PSSE, power system simulator for engineering, available at: http://w3.siemens.com/smartgrid/global/en/products-systems-solutions/software-solutions/planning-data-management-software/planning-simulation/pages/pss-e.aspx

[121] PowerWorld, visualization tool for the power system analysis, available at: http://www.powerworld.com/

[122] Simulink, block diagram environment for multi-domain simulation and model-based design, available at: http://www.mathworks.com/products/simulink/?s_iid=ovp_prodindex_1422057685001-69027_pm

[123] Edith Clarke, " Circuit analysis of A-C power systems; symmetrical and related components," Wiley, New York, 1943.

APPENDIX A

NUMBER OF BUS VOLTAGE VALUES BEYOND THE ANSI LIMIT

Table A.1 Number of bus voltage values beyond the upper limit

Tap settings / Hour	1 0.98 p.u.	2 0.99 p.u.	3 1 p.u.	4 1.01 p.u.	5 1.02 p.u.	6 1.03 p.u.	7 1.04 p.u.	8 1.05 p.u.
1	0	0	17	177	1807	3002	4155	5178
2	0	0	16	174	1867	3055	4197	5217
3	0	0	20	197	1879	3092	4213	5211
4	0	0	19	199	1869	3062	4216	5202
5	0	0	19	184	1747	2749	4092	5125
6	0	0	2	83	1293	2309	3938	4763
7	0	0	0	40	438	1474	2359	3724
8	0	0	0	0	46	804	1957	2642
9	0	0	0	0	52	955	2024	3774
10	0	0	0	0	53	1001	2138	4052
11	0	0	0	0	54	1021	2179	4110
12	0	0	0	0	54	1130	2326	4268
13	0	0	0	0	55	1167	2430	4357
14	0	0	0	0	49	1175	2551	4381
15	0	0	0	0	46	1153	2579	4379
16	0	0	0	0	46	1134	2575	4352
17	0	0	0	0	45	996	2243	4132
18	0	0	0	0	49	820	1879	3656
19	0	0	0	0	45	765	1753	3291
20	0	0	0	0	44	920	1588	3051
21	0	0	0	0	44	820	1544	3023
22	0	0	0	0	46	1208	1811	3236
23	0	0	0	0	52	2028	2064	3954
24	0	0	553	747	1759	2788	4090	5009
Total voltage violations in one day	0	0	646	1801	13439	38628	64901	100087

Table A.2 Number of bus voltage values below the lower limit

Tap settings / Hour	1 0.98 p.u.	2 0.99 p.u.	3 1 p.u.	4 1.01 p.u.	5 1.02 p.u.	6 1.03 p.u.	7 1.04 p.u.	8 1.05 p.u.
1	9	8	8	8	5	3	3	2
2	4	4	4	4	3	3	3	2
3	5	4	4	4	3	3	3	2
4	5	4	4	4	3	3	3	3
5	6	4	4	4	3	3	3	3
6	8	3	3	6	2	2	2	2
7	19	10	9	4	6	4	2	2
8	32	15	6	6	3	3	3	2
9	13	5	3	3	3	3	2	1
10	8	3	3	3	2	2	1	0
11	7	4	4	4	4	4	4	3
12	3	2	2	2	2	2	2	1
13	4	2	2	2	2	2	2	1
14	3	2	2	2	2	2	2	1
15	3	2	2	2	2	2	2	1
16	3	2	2	2	2	2	2	0
17	3	2	2	2	2	2	2	1
18	9	2	2	2	2	2	2	2
19	25	12	3	3	2	2	2	2
20	47	15	10	9	2	2	2	2
21	46	17	5	4	2	2	1	1
22	16	11	7	6	2	1	1	1
23	11	5	4	3	3	2	2	2
24	5	3	3	3	3	3	3	2
Total voltage violations in one day	294	141	98	92	65	59	54	39

APPENDIX B

PUBLICATIONS RELATED TO THIS WORK

[1] Narang, David, Raja Ayyannar, Paul Gemin, Murali Baggu, Devarajan Srinivasan, final technical report. results of Phases 2-5. United States: N. p., 2015. Web. doi:10.2172/1171386, available at: http://www.osti.gov/scitech/biblio/1171386

[2] M. Baggu, J. Cale, and D. Narang, "High-penetration PV deployment in the Arizona Public Service system, results from Phases 3-4 and update on (final) Phase 5," *Photovoltaic Specialty Conference (PVSC) 2014*.

[3] P. Gotseff, J. Cale, M. Baggu, D. Narang, and K. Carroll, "Accurate power prediction of spatially distributed PV systems using localized irradiance measurements," *Power and Energy Society (PES) 2014*.

[4] M. Baggu, B. Palmintier, J. Cale, and D. Narang, "Distribution modeling of closed-loop controls for advanced scenario analysis on feeders with high-penetration PV," *Photovoltaic Specialty Conference (PVSC) 2014*.

[5] J. Cale, B. Palmintier, D. Narang, and K. Carroll, "Clustering of distribution feeders on the Arizona Public Service system," *Photovoltaic Specialty Conference (PVSC) 2014*.

[6] M. Baggu, R. Ayyanar, and D. Narang, "Feeder model validation and simulation for high-penetration photovoltaic deployment in the Arizona Public Service system," *Photovoltaic Specialty Conference (PVSC) 2014*.

[7] Y. Tang and R. Ayyanar, "Verification of protective device coordination in distribution systems with photovoltaic generation," *Photovoltaic Specialty Conference (PVSC) 2014*.

[8] A. Nagarajan, R. Ayyanar, "Design and strategy for the deployment of energy storage systems in a distribution feeder with penetration of renewable resources," *IEEE Transactions on Sustainable Energy, 2014,* Article#: 2330294, IEEE Early Access.

[9] T. Joshi, G. Heydt, R. Ayyanar, "High frequency spectral components in distribution voltages and currents due to photovoltaic resources," *North American Power Symposium (NAPS), 2014*, pp. 1-6.

[10] Narang, David, Joshua Hambrick, Devarajan Srinivasan, Raja Ayyannar, Kathleen O'Brien, Jovan Bebic, and Owen Schelenz, 2011. "*Final technical report: results of Phase 1*," doi:10.2172/1036532, available at: http://www.osti.gov/scitech/servlets/purl/1036532